THE ATTENUATION OF RADIANT ENERGY IN HOT SEEDED HYDROGEN

A THESIS

Presented to

The Faculty of the Graduate Division

by

Arkal Subraya Shenoy

In Partial Fulfillment

of the Requirements for the Degree

Doctor of Philosophy

in the School of Nuclear Engineering

Georgia Institute of Technology

May, 1969

In presenting the dissertation as a partial fulfillment of the requirements for an advanced degree from the Georgia Institute of Technology, I agree that the Library of the Institute shall make it available for inspection and circulation in accordance with its regulations governing materials of this type. I agree that permission to copy from, or to publish from, this dissertation may be granted by the professor under whose direction it was written, or, in his absence, by the Dean of the Graduate Division when such copying or publication is solely for scholarly purposes and does not involve potential financial gain. It is understood that any copying from, or publication of, this dissertation which involves potential financial gain will not be allowed without written permission.

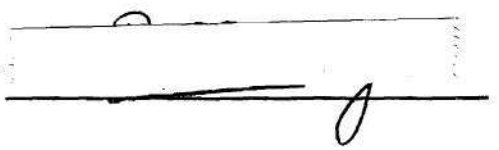

7/25/68

THE ATTENUATION OF RADIANT ENERGY IN HOT SEEDED HYDROGEN

Approved:

Date approved by Chairman: May 22, 196

ACKNOWLEDGMENTS

This research project was supported by NASA grant NGR-11-002-068 and monitored by the Advanced Nuclear Propulsion Concepts Branch of the Lewis Research Center. Many individuals have contributed their special talents towards the completion of this research. The author wishes to thank Mr. R. G. Ragsdale, Mr. F. E. Rom and their associates for their helpful comments and suggestions during the course of this work. The author is especially grateful to Mr. C. C. Masser for his technical advice during his several visits to the campus while this work was in progress.

I am very grateful to Dr. J. D. Clement, my thesis advisor, and Dr. J. R. Williams, my thesis consultant, for their constant interest, encouragement, and professional support throughout the duration of this research effort. Dr. J. R. Stevenson served on my thesis committee and suggested the original design of the spectrometer. His suggestions and assistance have been greatly appreciated. Dr. G. G. Eichholz contributed many helpful suggestions during the drafting of the manuscript. I wish to thank Dr. C. J. Roberts of the School of Nuclear Engineering for his support during the course of this work.

To my good friend, Mr. W. L. Partain, I wish to express my sincere gratitude for hours of unselfish assistance. I owe a special debt of gratitude to my fellow nuclear engineering graduate students, Ken Stephens, Alex Hawes, Phil Plemmons, Ken Kirby, Pete Aucoin, Mike Phillips, Will

Vanderzalm, and Won Guk Hwang, for their contributions and assistance during the course of this work.

The author would like to thank Mr. N. L. Kracella of United Aircraft Corporation for the Mie scattering computer program and for his assistance in implementing this program at Georgia Tech.

I would like to thank Messrs. Harold Huey and Finn Scarboro of the Engineering Experiment Station machine shop for their excellent work in constructing the furnace, spectrometer, and other experimental equipment. Mr. Hadley Wellborn of the High Temperature Materials Division has helped in obtaining various seed materials. Thanks are also due to undergraduate students, Leon Russell, Dick Driscoll, John Owen, Ned McCubbin, Bill Austin, Howard Davis, and David Boddiford, who helped during the course of this work. I also wish to thank Mr. J. L. Hubbard of the Engineering Experiment Station, whose excellent work on the electron micrographs was vital to this thesis. The assistance in electronics design given by Mr. Billy D. Statham is greatly appreciated. Mrs. Lydia Geeslin has done an outstanding job of editing and typing this manuscript.

To my brothers, I express my deep appreciation for their unfaltering confidence and encouragement during my several years of graduate study.

TABLE OF CONTENTS

TABLE OF CONTENTS (Concluded)

LIST OF TABLES

LIST OF TABLES (Concluded)

LIST OF ILLUSTRATIONS

LIST OF ILLUSTRATIONS (Continued)

LIST OF ILLUSTRATIONS (Continued)

LIST OF ILLUSTRATIONS (Concluded)

SUMMARY

Measurements of the optical absorption parameters as a function of temperature and incident radiation wavelength are made of hydrogen seeded with submicron-sized particles. Hydrogen, first unseeded and then seeded, is heated in a furnace employing an electrically heated tungsten strip. Radiation of wavelengths from about 1200 Å to 6000 Å is passed through unseeded and then seeded hydrogen at a given temperature. Measurements of the transmission for the two cases yield the absorption parameters for the particle seed in hydrogen gas.

The absorption coefficients of carbon-hydrogen, tungsten-hydrogen, and silicon-hydrogen aerosols were measured as a function of radiation wavelength at various temperatures up to 3450° F. The submicron-sized carbon particles have a relatively high absorption coefficient of the order of 50,000 cm^2/gm. However, at higher temperatures the carbon particles disappear apparently due to the chemical reactions between hydrogen and carbon. In the case of tungsten particles, the absorption coefficient varies from 10,000 cm^2/gm to 20,000 cm^2/gm depending upon the size of the particles. The absorption coefficient of silicon particles at room temperature is about 65,000 cm^2/gm. In all of these cases the mass absorption coefficient is essentially independent of wavelength over the range of wavelengths and temperatures investigated.

Electron micrographs of carbon, tungsten, and other seed materials of various particle sizes have been taken for various operating conditions.

The electron micrographs present representations of the particles of which the mass absorption coefficient is measured.

The absorption coefficient of clouds of tungsten, carbon, and silicon particles is calculated using the Mie theory for particle sizes from 0.01 micron to 1.0 micron and radiation wavelengths from 1000 Å to 6000 Å. The absorption coefficient has been calculated for carbon at 3590°F, silicon at 80°F, and tungsten at 76°F, 1520°F, and 2420°F.

CHAPTER I

INTRODUCTION

Background

The performance of a rocket engine is measured primarily by two factors, the thrust-to-weight ratio and the specific impulse.[1,2] The thrust-to-weight ratio is the thrust of the propulsion system divided by the total weight of the vehicle and should be as large as possible so that a given mission can be accomplished with a minimum fuel expenditure. The specific impulse of a rocket engine is defined as the thrust divided by the weight flow rate of the propellant. For more energetic missions and to carry larger payloads, a high specific impulse is necessary. The present chemical rocket engines have an adequate thrust-to-weight ratio but their specific impulse is limited to about 400 seconds. Nuclear rocket engines can achieve both high specific impulse and a high thrust-to-weight ratio.

The basic difference between chemical and nuclear powered vehicles is the method of producing the energy which heats the propellant. The chemical system fills its energy needs from the combustion of its fuel or propellant, whereas the working fluid of a nuclear rocket need not provide any such intrinsic energy since this is supplied by nuclear reactions. The energy content of fissionable fuels is nearly 10^7 times that of the best chemical combustible mixtures.[1] The effect of nuclear heating on rocket performance can be seen more readily by writing the equation for

the specific impulse

$$\text{specific impulse} = \frac{\text{thrust}}{\dot{m} g_c} \tag{1}$$

where $\dot{m}$ is the mass flow rate of propellant and g_c is a constant equivalent to the acceleration of gravity at sea level. Since thrust is given by $\dot{m} v_e$

$$\text{specific impulse} = \frac{v_e}{g_c} \tag{2}$$

where v_e is the average velocity of the exhaust through the nozzle. The mean square velocity of the gas molecules is given by

$$E = \tfrac{1}{2} m v^2 = \tfrac{3}{2} kT$$

where m is the molecular weight, T is the absolute temperature of the gas, and k is the Boltzmann constant. Thus

$$v = \sqrt{\frac{3kT}{m}} = \text{const.} \sqrt{\frac{T}{m}} \tag{3}$$

Therefore, since v_e is proportional to v

$$\text{specific impulse} = \text{const.} \sqrt{\frac{T}{m}} \tag{4}$$

From equation (4) the specific impulse increases with both decreasing molecular weight and increasing propellant temperature. The key to

the large performance increase of first generation solid core nuclear rockets over present chemical rockets is the lower molecular weight of the propellant. In solid core reactors, the propellant is heated to about 4000°F, while the propellant temperature in a chemical rocket may be slightly higher. But the performance lost in nuclear rockets because of lower temperature is more than made up for in the low molecular weight of the hydrogen propellant. The solid core nuclear rocket currently has a specific impulse more than twice that of the best chemical rocket.

Given this increase in performance due to the smaller propellant molecular weight, any further increases depend primarily on increasing the temperature of the hydrogen propellant. This is the direction one must take for future generation nuclear rockets.[4,5] In the solid core nuclear rocket engine, the limiting temperature is about 5000°F. Moving up the temperature scale is the so-called dust-bed reactor.[6] Here the aim is to circumvent the temperature limitation of the solid core by eliminating the structural matrix. Instead, the uranium compound would be in the form of tiny dust particles held in a critical mass by the centrifugal force that presses them against the inner side of a rotating drum. Temperatures associated with this concept range up to 6500°F, or a specific impulse of up to 1100 seconds. Next up the temperature scale is the liquid-core reactor.[7] Here the uranium compound would again be held in a critical configuration by the centrifugal force of a rotating drum, but it would be a liquid. The hydrogen would bubble through the liquid uranium layer. The limiting temperature would be in the neighborhood of 8000°F, with a maximum specific impulse of 1600 seconds.

At the top of the reactor temperature scale is the gaseous-core

nuclear rocket engine[8,9,10] which would operate at temperatures higher than the melting point and boiling point of solid and liquid core reactor materials. This is the most advanced rocket reactor concept and would heat propellant to as high as 30,000°F producing specific impulses of up to 3000 seconds.[11] Two concepts of gaseous core nuclear rocket engines that are being investigated are the coaxial flow concept[12,13] and the nuclear light bulb concept.[14,15] In the coaxial flow concept, a slow moving central stream of fissioning fuel heats a fast moving annular stream of hydrogen solely by radiation. In the nuclear light bulb concept, the fissioning fuel is contained in a transparent partition and the propellant is heated by radiation through the partition. A number of such light bulbs may be arranged together to form a critical mass.

In both of these concepts, a very hot core of gaseous fissioning fuel radiates energy to the propellant. Thus, the hydrogen propellant is heated by the thermal radiation from the core. Hydrogen below about 10,000°F is transparent to the thermal radiation from the core.[16] At temperatures greater than approximately 10,000°F, the first excited state of the hydrogen atom becomes sufficiently populated that the bound-free transition from the first excited state becomes important.[15] At low temperatures, the only appreciable absorption is due to the bound-free transition from the hydrogen ground state and this absorption is encountered only for radiation of energy above the ionization potential. The propellant can be made opaque to the radiation from the core by seeding with gas having a low ionization potential or submicron-sized solid particles of a highly absorbing material. In the case of gases, line absorption is more predominant thereby absorbing radiation of particular wavelengths, and the

widths of the lines were found to be small and to absorb a negligible portion of the complete spectrum of radiation. Submicron-sized particles, however, absorb over a broad wavelength range and are, therefore, a much more useful seed material for the propellant. The absorption parameters of propellant seeded with particles are important for gaseous core nuclear reactor heat transfer calculations. The particles insure maximum heat transfer to the propellant and minimum heating of the containment vessel. A number of papers[17,18] are found in the literature regarding the solution of Maxwell's equations for spherical particles. In 1908 Mie[19] published a rigorous solution for the scattering and absorption of electromagnetic radiation by a homogeneous sphere of any diameter and of any composition. Krascella[20] has used Mie's equations to calculate theoretically the absorption and scattering parameters of small spherical particles of various materials. Svatos[21] has published the solution for the scattering of electromagnetic radiation by flattened ellipsoids.

Several groups have experimentally investigated the absorption parameter of seeded gases. Lanzo and Ragsdale[22,23] investigated experimentally the absorption of suspended particles as a function of material, size, and concentration. The experiment involved radiation from an electric arc to air that contained submicron-sized particles. Seeded air was introduced into an annular heat exchanger. The arc was initiated at time zero, and the unseeded air temperature in the annulus reached 540°F. When the carbon particles were added to the air stream, they absorbed radient energy causing the outlet temperature to increase to 740°F, thus showing that seeded particles will absorb radiant energy from the electric arc. McAlister[24,25] reported theoretical and experimental studies of ra-

diant heat transfer from a heated tungsten cylindrical enclosure to a cloud within it. A transparent gas, helium, was passed through the tube and the tube dimensions and helium flow rate were selected to give a low thermal efficiency for forced convection heating. The addition of tungsten particles to render the gas opaque caused a significant increase in heat absorption.

Marteney[26] studied techniques of producing dispersions of submicron-sized solid particles in a carrier gas and investigated the optical parameters of these particles for several wavelengths. Tests were conducted with carbon and tungsten particles having nominal radii of 0.0045 and 0.01 micron, respectively, dispersed in helium and nitrogen. These studies showed that the application of aerodynamic shear forces to a carbon aerosol resulted in an increase by a factor of five in the absorption parameter. This increase is believed to be caused by a reduction in the size of particle agglomerates since theoretically a decrease in the average agglomerate size should result in an increase in the value of the extinction parameter.[20]

The first experimental work involving seeded gases at elevated temperatures was reported by Burkig.[27] In this experiment, a cloud of particles in a gas was injected into a transparent quartz tube and exposed to a flash of a xenon flash tube. The temperature rise of the gas was inferred from the pressure rise measured with a fast response pressure transducer. The bulk of the work was with fine particles (about one micron) of carbon, iron, and tantalum carbide. In general, initial pressures of two and five atmospheres were investigated for both helium and hydrogen. During the flash, as indicated by the pressure transducer, the temperature

of the carbon aerosol rose to about 3600°F or more for about one millisecond. After the flash, solid residues were examined for chemical products and evidence of vaporization; no evidence of chemical changes was found.

One problem with experiments involving heat transfer from hot tungsten tubes or arcs to a gas containing small particles is that the maximum temperature of the tungsten tube (about 5400°F)[24] or the arc (about 14,000°F)[28] is much lower than the expected temperature of the gaseous core (about 40,000°F).[12] This means that the emission of the radiation from the gaseous core will be almost entirely in the ultraviolet or near ultraviolet, whereas for the arc and tungsten tube, the emission is primarily in the visible or infrared.

Williams[29] measured the absorption parameter of carbon particles in nitrogen gas as a function of incident radiation wavelength in the range from 1100 Å to 6000 Å at temperatures up to 1525°F. The resulting data showed that, at room temperature, the mass absorption coefficient of the carbon seed in nitrogen is essentially independent of wavelength from 1100 Å to 6000 Å. Observations at higher temperatures up to 1525°F indicated no change in either the magnitude or the dependence on radiation wavelength. It is indicated from this work that the experimental technique used with some modifications is meaningful and realistic in measuring the absorption parameter for various seed materials.

To date, no work has been reported on the optical properties of equilibrium carbon-hydrogen or tungsten-hydrogen aerosols at elevated temperatures. Also, the work reported thus far primarily involves the attenuation of energy from broad spectrum radiation sources. No measurements

have been made previously of the optical properties of hydrogen seeded with submicron-sized particles as a function of wavelength over a broad range of wavelengths, and very little has been reported regarding the optical properties of aerosols in the ultraviolet range. In the gaseous core rocket, most of the energy reaching the particles would probably lie in this wavelength range.

To evaluate the absorptive properties of seeded propellant for various core temperatures, propellant temperatures, seed concentrations, and pressures, one may measure the optical absorption of the particle seed as a function of pressure, temperature, and radiation wavelength.

When radiant energy falls upon a cloud of particles suspended in a transparent medium, two processes, absorption and scattering, may occur. It has been shown that, for most seed materials of interest, aerosols of submicron-sized particles absorb much more energy than they scatter, and this scattering is highly forward.[30] Thus, the seeded propellant may generally be treated as a purely absorbing medium. Also, for dispersions of submicron-sized particles in a gas, the particles and gas can generally be considered to be in thermal equilibrium.[31]

The absorption of a beam of radiation in a purely absorbing medium is governed by the simple expression

$$I(\lambda,X) = I(\lambda,o)\, e^{-K_T(\lambda,T,P)X} \tag{5}$$

where $K_T(\lambda,T,P)$ is the total linear attenuation coefficient at wavelength λ, temperature T, and pressure P, and X is the distance into the medium.

In a gas containing particles, the absorption takes place by ab-

sorption in the gas and absorption due to the particles. For radiation wavelengths of interest, the submicron-sized particles absorb much more energy than they scatter,[20] and this scattering is shown to be highly forward.[30] In such cases

$$K_T(\lambda,T,P) = K_g(\lambda,T,P) + K_p(\lambda,T,P) \tag{6}$$

where

$K_g(\lambda,T,P)$ is the absorption coefficient due to absorption in the gas alone at wavelength λ, temperature T, and pressure P

$K_p(\lambda,T,P)$ is the absorption coefficient for the particles in the gas and products of particle-gas reactions at wavelength λ, temperature T, and pressure P

The attenuation of radiant energy in a seeded gas is proportional to the seed density. The seed density, ρ, is defined as the weight of seed material in a unit volume of aerosol. Since $K_p(\lambda,T,P)$ is proportional to ρ, it is convenient to define the absorption parameter, $\mu(\lambda,T,P)$ to be

$$\mu(\lambda,T,P) = \frac{K_p(\lambda,T,P)}{\rho(T,P)} \tag{7}$$

The absorption parameter, μ, is independent of particle concentration as long as the average distance between particles is much greater than the average effective particle radius and the particles are randomly oriented. If the absorption parameter, $\mu(\lambda,T,P)$ is measured for a particle seed in a gas for which $K_g(\lambda,T,P)$ is known,[16] then $K_T(\lambda,T,P)$ can be evaluated for any particle concentration of interest in that gas

$$K_T(\lambda,T,P) = K_g(\lambda,T,P) + \rho(T,P)\cdot\mu(\lambda,T,P) \qquad (8)$$

where λ is the radiation wavelength, T is the aerosol temperature, and ρ is the particle seed density in grams of seed material per cubic centimeter of aerosol. K_T and K_g have units of cm^{-1}, whereas μ has units of cm^2/gm.

Krascella[16] has calculated values of K_g for hydrogen over a wide range of temperatures from 3000 to 200,000°F and pressures from one to 1000 atmospheres. Hydrogen below 10,000°F is completely transparent to the radiation above 2000 Å.

Purpose of the Research

The purpose of the research was to:

1. Measure the mass absorption coefficient of hydrogen seeded with submicron-sized carbon particles at one atmosphere pressure. The measurement is done for incident radiation of wavelength from about 1200 Å to about 6000 Å at temperatures up to about 3500°F.

2. Investigate the effect of high temperature on carbon-hydrogen aerosols compared with nitrogen-carbon aerosols and hence to evaluate the effect of chemical reactions.

3. Measure the mass absorption coefficient of hydrogen seeded with submicron-sized tungsten particles at one atmosphere pressure for radiation wavelengths from 1200 Å to 6000 Å and at temperatures up to 3500°F.

4. Calculate theoretically the absorption coefficients of carbon, tungsten, and silicon at temperatures for which their properties are available for particle sizes from 0.01 micron to 1.0 micron and radiation wavelengths 1000 Å to 6000 Å.

Application of the Research

One of the important applications of the results of this research is in evaluating the transport of radiant heat energy in the gaseous core nuclear reactor. Calculations[31] evaluating the temperature distribution and heat loads will utilize the results of this research. The results of this work shed light on the selection of a seed material for absorbing the radiant energy.

In addition to the above applications, these data may be useful in a number of problems of engineering interest. These include such applications as re-entry shielding,[32] nozzle cooling in propulsion systems,[33] chemical reactors and certain types of furnaces.

CHAPTER II

INSTRUMENTATION AND EQUIPMENT

The experimental setup is illustrated in Figures 1-3. Hydrogen, first unseeded and then seeded, is heated in the furnace to temperatures up to about 5000° R by an electrically heated tungsten strip. A beam of radiant energy from a capillary discharge tube passes first through unseeded and then seeded hydrogen at a given temperature. Radiant energy passing through the furnace falls on the grating and is refracted to photomultiplier 1 in Figure 1. Measurements of the transmission for the two cases yield the absorption parameters of the hot seeded hydrogen. A small portion of the beam is diverted by a pair of mirrors (not shown in Figure 1) to photomultiplier 2 to monitor changes in the aerosol concentration. The two photomultipliers shown in Figure 1 monitor the transmission through the hot aerosol. There is another aerosol monitor at the entrance of the furnace (Figure 4) to monitor the cold aerosol. A two watt concentrated zirconium arc lamp is employed as a light source. This light passes through the cold aerosol and is monitored by photomultiplier 3. Outputs from these three photomultiplier tubes are measured by picoammeters and recorded by a Honeywell visicorder.

The drive mechanism as shown in Figure 1 consists of a 75 rpm synchronous reversible motor which drives a shaft to turn the defraction grating to scan the spectrum to 6000 Å. Limit switches on the drive mechanism limit the traverse of the drive shaft and automatically reverse

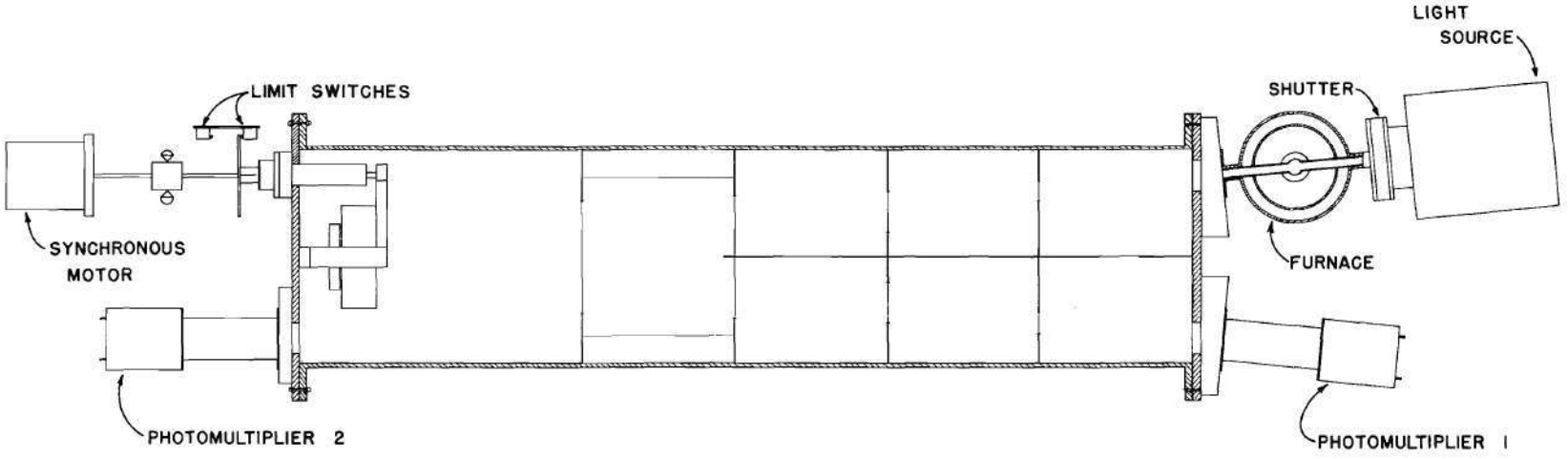

Figure 1. Monochromator Assembly

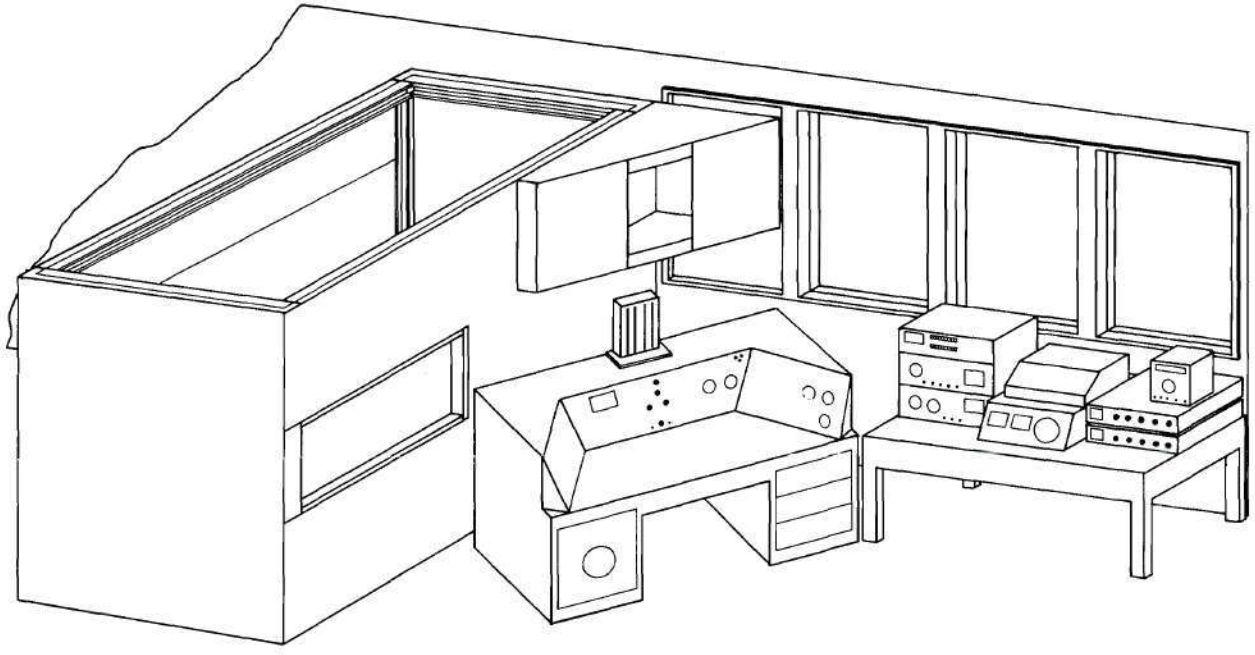

Figure 2. Control Console

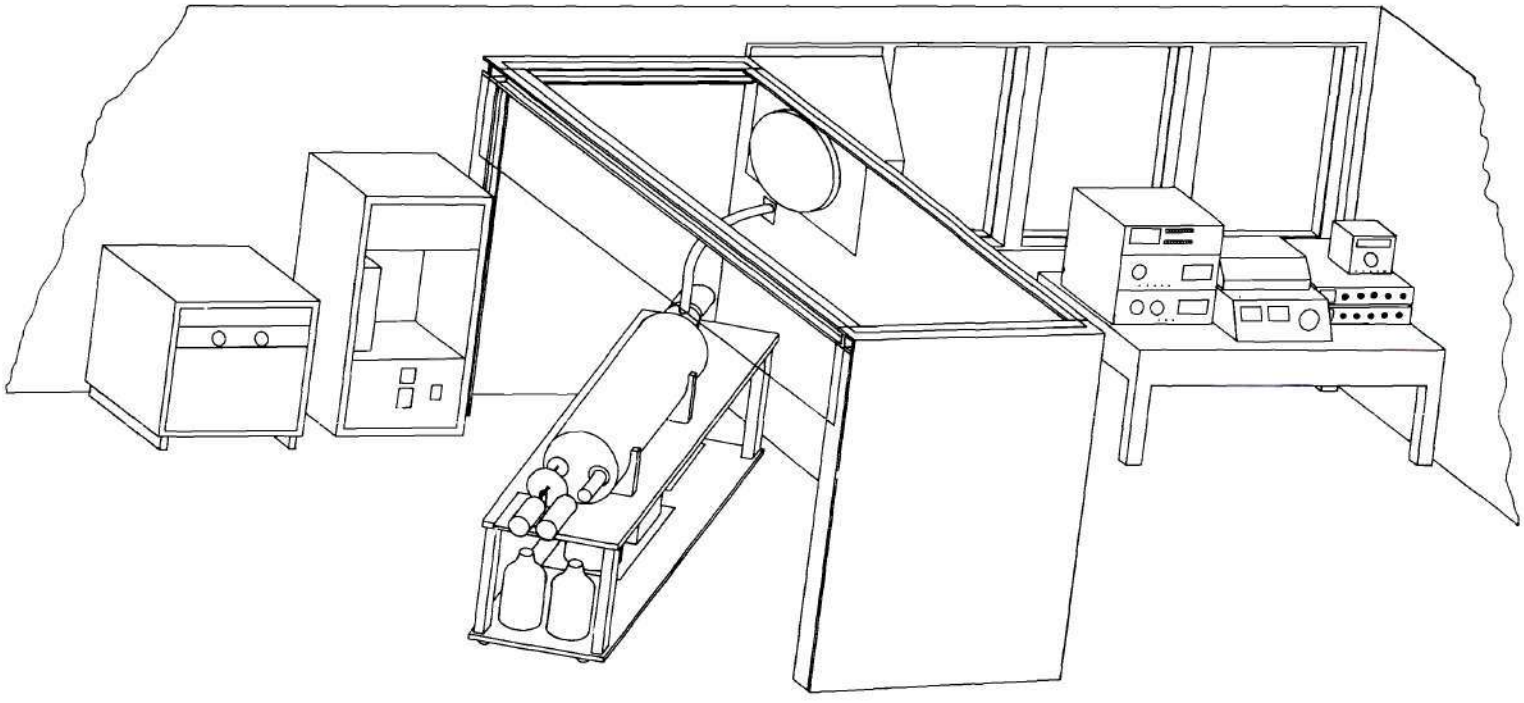

Figure 3. Equipment Layout

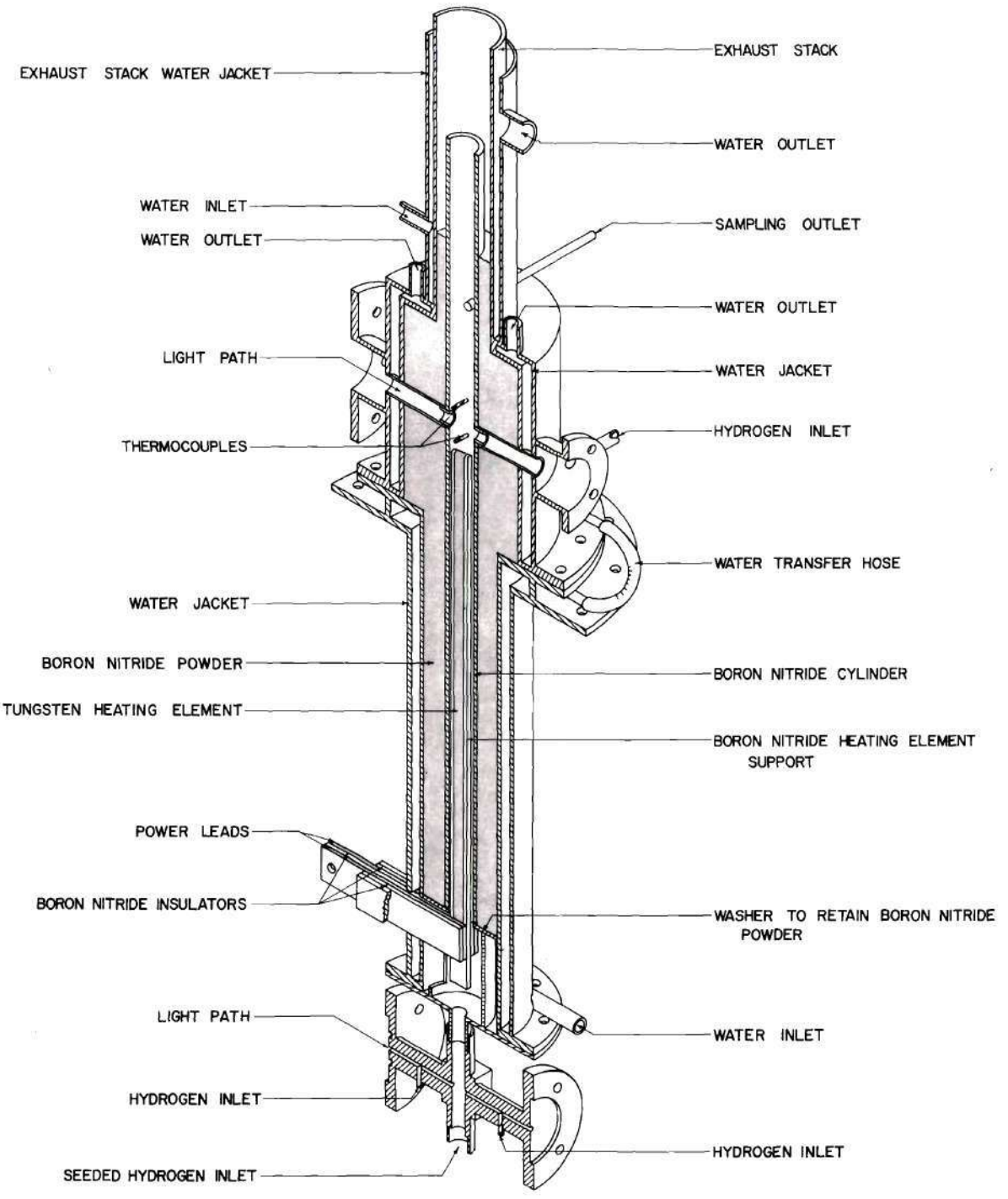

Figure 4. Furnace Assembly

the rotation of the grating after the spectrum has been scanned in the forward direction in order to scan the spectrum in the reverse direction. At the end of the reverse scan, the limit switch shuts off the motor. Initially, a push button switch starts the drive of the visicorder and the synchronous motor.

The mixture of submicron-sized particles and hydrogen is produced by an aerosol generator. The aerosol generator essentially consists of a chamber in which submicron-sized particles are mixed with hydrogen by blades driven by a motor. This mixture at a pressure of about 400 psi is passed through a nozzle before entering the furnace to further deagglomerate the particles.

The experimental setup is located in a laboratory of 12 feet by 24 feet. Since hydrogen is an explosive gas, the room is partitioned by a double thickness aluminum wall to separate the personnel from the equipment. On one side of the wall the control console, data recording table, and gas control system are located, and on the other side of the wall the experimental equipment is located. This enables the operator to conduct the experiment remotely from the control console safely. Figure 2 shows the aluminum wall and the control console. All the switches, valves, and motors are fixed on the console and power supplies, recorders, and picoammeters are placed on the data recording table on the left. The cylinders of gas which are not shown in the figure are chained to the wall behind the operator. The wall contains a double thickness Plexiglas window to allow observation of the equipment while data are being taken.

Figure 3 shows the experimental equipment located behind the wall in a hood. The spectrometer, furnace, etc. are mounted on a wheeled table

so that the whole setup can be moved outside for any major repairs. All of the larger power supplies are located near the main equipment. In order to avoid a buildup of hydrogen, the hood utilizes a large capacity exhaust fan as shown in the figure.

High Temperature Furnace

The high temperature furnace is designed to heat the aerosol mixture to temperatures of the order of 5000°R. Figure 4 illustrates the furnace. There are two positions where the transmission of light is measured, at the bottom where the aerosol enters, and at the top after the aerosol has been heated.

The heating element is a two and one-half foot long by five-eighths inch wide strip of 25 mil thick tungsten. The ends of the heating element are connected by copper power leads to a 20 kilowatt dc power supply. Supporting the tungsten heating element is a one-eighth inch thick hot pressed boron nitride strip. The whole heating element is contained in a five-eighths inch ID boron nitride tube in which the aerosol is heated. By varying the flow rate of aerosol and the heater voltage, the desired temperature is attained.

The one inch OD boron nitride tube is placed in a water jacket. The annular space between the boron nitride tube and water jacket is filled with boron nitride powder to serve as insulation. The copper water jacket is made in two parts so that the furnace can be disassembled and reassembled easily. The furnace is designed so that the filament can be easily replaced if it burns out.

The top observation tube is located about one-half inch above the

upper end of the heater element. In the center where the temperatures are high, the observation tube is made of 0.375 inch ID, 0.02 inch thick tungsten. The ends of these tungsten tubes telescope inside a stainless steel tube of 0.5 inch OD. The two stainless steel tubes end at flanges which connect to the light source and to the spectrometer.

After passing between the observation tubes, the aerosol exhausts to an aerosol disposal system. There are two sampling systems used to measure the concentration of seed material in the hydrogen. One sample is taken at the entrance of the furnace and the other sample is taken near the exhaust. These two samples are used to study the effect of temperature on seed vaporization.

Temperature measurements are made with tungsten three percent rhenium versus tungsten 26 percent rhenium thermocouples. These thermocouples are capable of operation in hydrogen at 5000°F. The temperatures are measured immediately below the light beam and immediately above the light beam with two thermocouples.

Light Source

The light source which is used in the ultraviolet and visible regions of the spectrum is a McPherson Model 630 Hinterregger-type gas discharge[34] lamp. Figure 5 shows the sectional view of the light source and its connection to the furnace. The light source has a three-sixteenths inch diameter glass capillary discharge tube which is cooled by water and has an aluminum cathode which is air cooled by a fan in the lamp housing. The light source is capable of handling 1000 watts of energy continuously and up to 8000 watts intermittently. In operation, this light source can

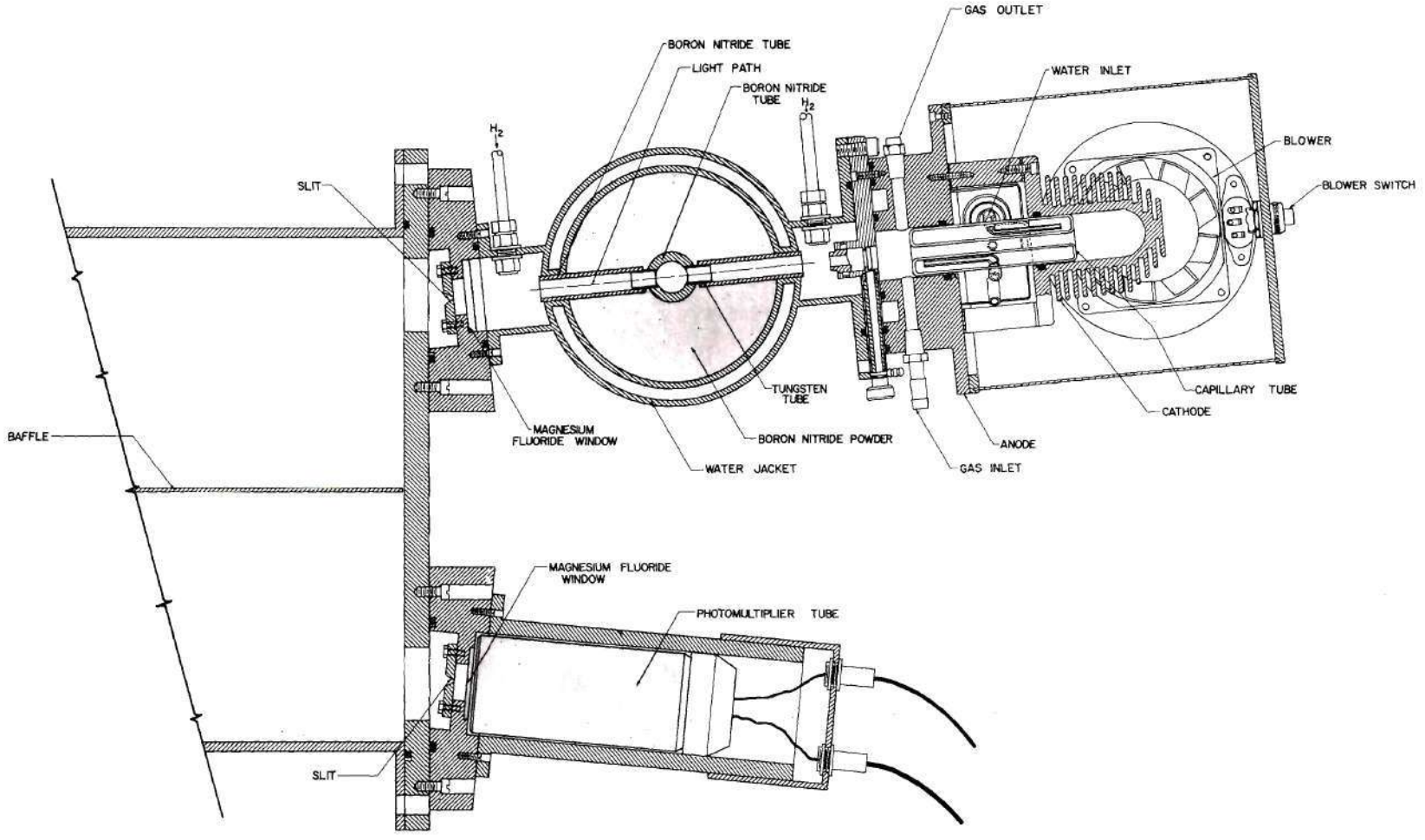

Figure 5. Spectrometer Assembly - Furnace End

produce line spectra or continua, depending on the gas and pressure. In this particular operation, hydrogen is used to give a spectrum in the ultraviolet and visible.

The gas regulating system consists of a hydrogen tank, regulator, throttling valve, and an absolute pressure indicator calibrated from zero to 100 mm mercury. A mechanical vacuum pump is used to maintain a vacuum in the main chamber. The necessary power is provided by a Consolidated Vacuum Corporation model LC-031 dc power supply. The light source is bolted to the slit flange of the furnace as shown in Figure 5. The other flange of the furnace is connected to the monochromator.

Monochromator

The monochromator shown in Figure 3 is a modification of one in the Georgia Tech School of Physics which was designed by Dr. J. R. Stevenson. The main chamber is constructed from a stainless steel tube 10.75 inches in outside diameter with a wall thickness of 0.165 inch. One-quarter inch thick flanges are welded to the tube ends, giving an overall length of 42 inches. One-half inch thick stainless steel plates for mounting the grating holder at one end of the tube and the entrance and exit slits at the other are sealed by O-rings to the flanges by means of 16 three-eighths inch bolts. Four baffles are equally spaced inside the chamber to minimize the unwanted light arriving at the exit slits.

The aluminum grating holder shown in Figure 6 is bolted directly to the end plates. The grating is a Bausch and Lomb replica grating with a one meter radius of curvature and a groove spacing of 600 lines per millimeter. The rotation of the grating is accomplished by advancing a

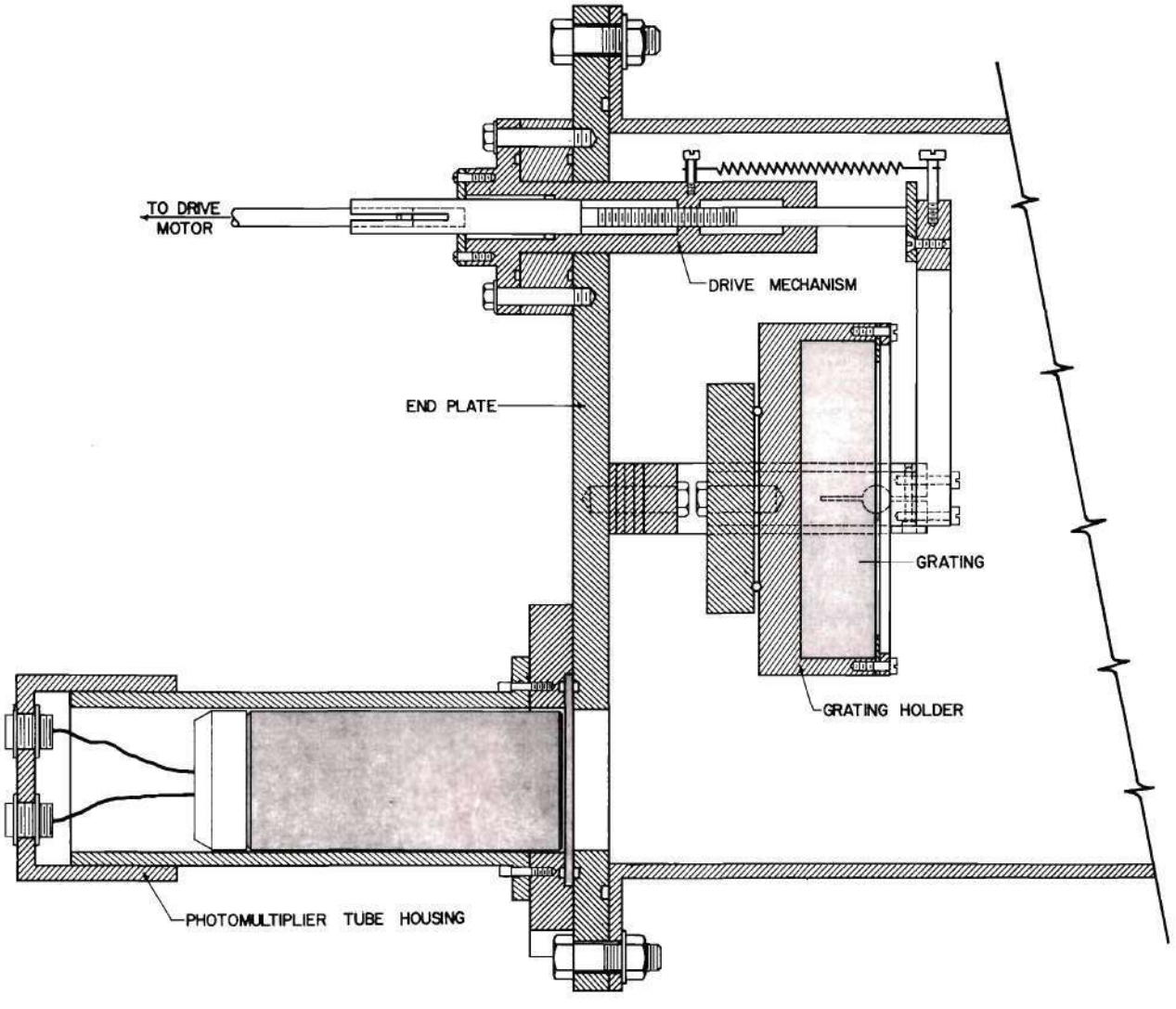

Figure 6. Spectrometer Assembly - Grating End

finely-threaded drive rod through the end plate. The rod is spring-loaded against an arm on the grating mount. The drive rod is turned by a variable speed, reversible dc motor by means of a pin and slot drive. There are two limit switches which operate a number of relays to reverse and stop the dc motor. On pressing a contact switch at the operating console, the drive motor starts scanning the spectrum, and when it reaches the end of the spectrum, the limit switch reverses the direction of the motor thereby bringing the grating to the original position. As the drive shaft comes to the initial position, the other limit switch reverses and stops it so that it is ready for another spectrum scan.

A mechanical vacuum pump is connected to the monochromator which maintains a pressure of less than one micron of mercury in the chamber. The chamber pressure is measured by means of a thermocouple vacuum gauge and indicated by a meter at the operating console.

The furnace is connected to the spectrometer at an angle of six degrees to the axis as shown in Figure 5. The ray of light passing through the furnace falls on the grating and is refracted to the photomultiplier. A small portion of the beam is diverted by a pair of mirrors to pass through a bandpass filter to another photomultiplier tube to monitor the changes in the aerosol concentration.

The Aerosol Generator

It has been shown that an aerosol generator consisting of a chamber with mixing blades driven by an external motor will yield a good aerosol.[25] The penetration necessary for the motor shaft connection has proved to be a major source of leakage however, and for hydrogen this would be undesir-

able from a safety standpoint. Therefore, the task of designing an aerosol generator for use with hydrogen and submicron-sized particles was undertaken.

The experiment requires the dispersion of bulk powder into submicron-sized particles in hydrogen gas. Aerosol flow rates are small, so dispersion is obtained through highly turbulent mixing under pressure and subsequent expansion of the aerosol through a small orifice.

The aerosol generator design is shown in Figure 7. The gas is introduced above the motor and flows past a loose Teflon seal on the rotating shaft into the mixing chamber. The mixing chamber is initially filled approximately one-third full with seed material, and the mixing blades which rotate at 1200 rpm mix the seed particles with the gas. The aerosol exits the mixing chamber through the outlet tube near the center of the chamber. The larger particles and agglomerates are thus discriminated against through the centrifugal action of the mixing blades. The highest degree of dispersion is obtained by allowing the aerosol to expand through a small orifice.

The aerosol generator is operated at a pressure of 500 to 1000 psi. The nozzles used have orifices of 0.00635 inch and 0.0135 inch in diameter, the smaller nozzle orifice being used at higher pressures. The method of controlling the aerosol concentration is illustrated by Figure 8. By changing the flow rate through the direct line or bypass line by means of valve A and valve B, respectively, the concentration can be controlled. It has been found that the best control is by manipulation of valve B at a particular setting of valve A. Increasing the bypass flow dilutes the aerosol. The mixing blades have almost absolute control on aerosol con-

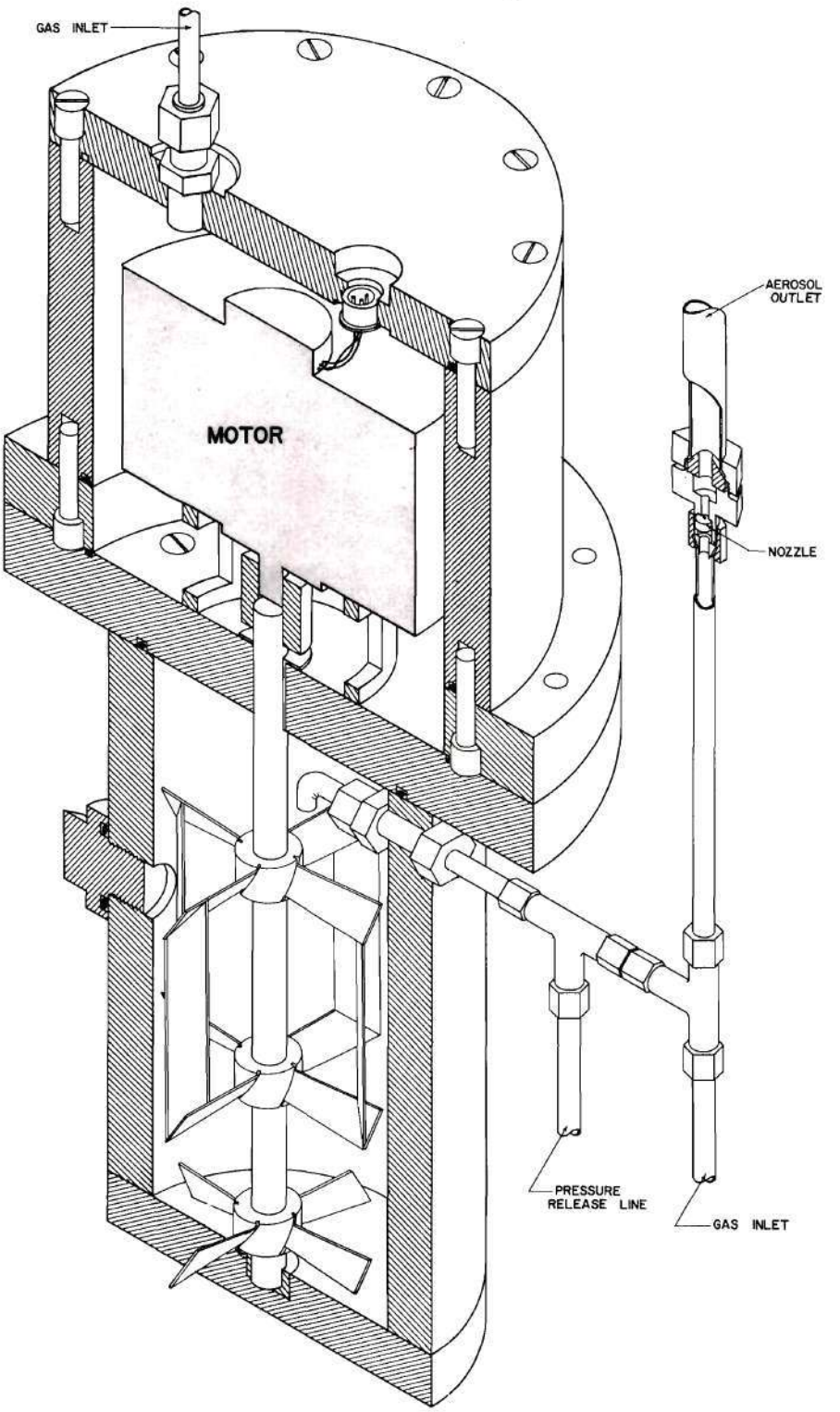

Figure 7. Aerosol Generator

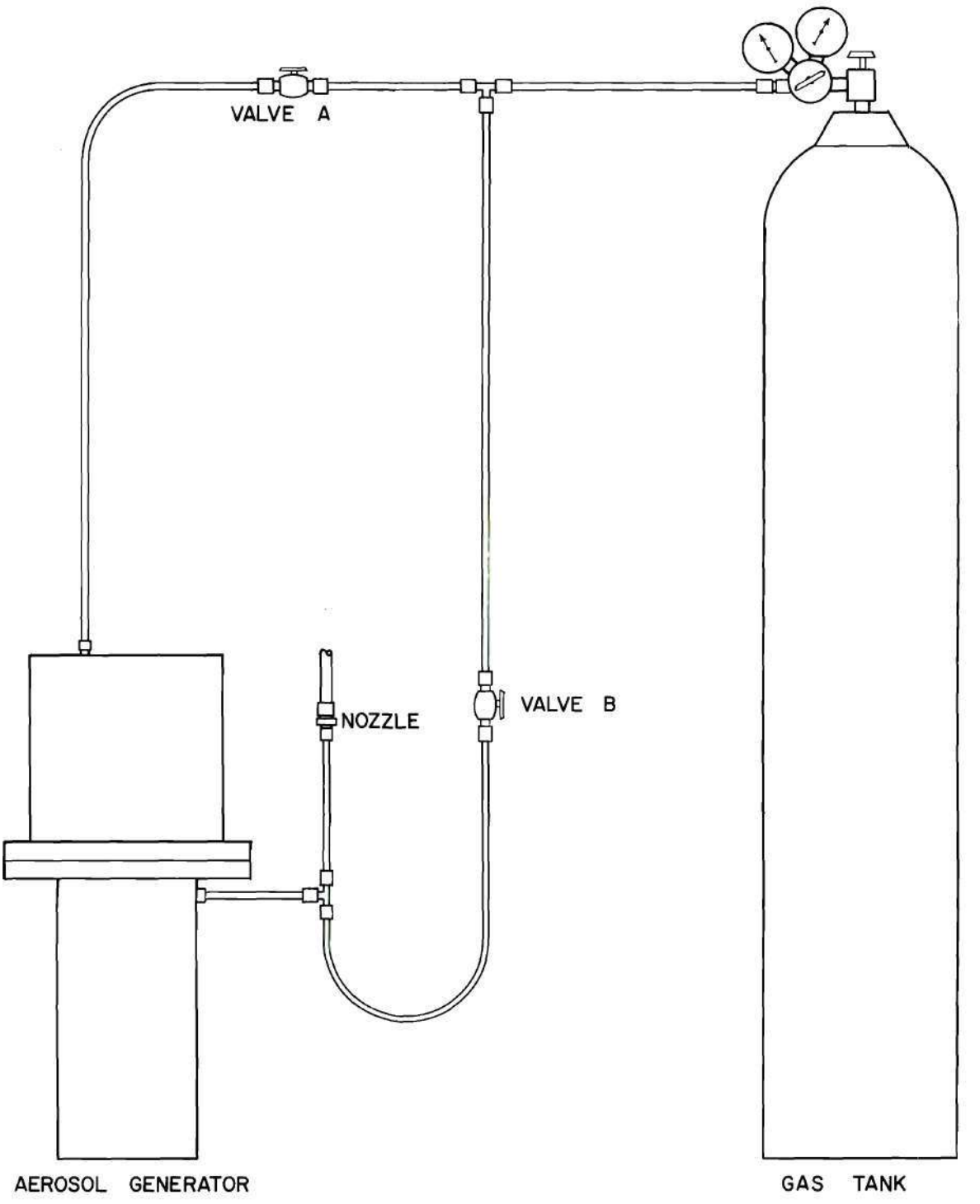

Figure 8. Aerosol Generator Operation

centration. When the blades are not rotating, the gas is not seeded with particles.

The uniformity of the aerosol has been visually observed for periods of time in excess of 30 minutes.

Aerosol Sampling

The aerosol concentration, in grams of seed material per cubic centimeter of aerosol, is measured by passing a known volume of aerosol through a filter and measuring the weight of seed material deposited on the filter. The concentration is then the weight of deposited seed material divided by the volume of gas passing through. The sampling apparatus is illustrated by Figure 9.

The system operates as follows. With hand valve B open, solenoid valve A closed, and solenoid valve B open, bottle B and the line to the furnace are purged with nitrogen to prevent the buildup of an explosive mixture of hydrogen and air when the sample is drawn. After the purging operation is completed, the sampling is done as follows. The vacuum pump is turned on and a single double-pole switch is operated closing solenoid valve B and opening solenoid valve A. Hand valve A is then opened slightly to pull the sample. The pressure differential causes water to flow from bottle B to bottle A, lowering the pressure in the filter holder line. The difference in pressure between the filter holder line and the furnace outlet causes a portion of the aerosol to be drawn through a glass fiber filter in the filter holder. A sample is pulled for about one minute. The rate at which the sample is drawn can be regulated by the hand valve. This may be necessary to prevent disturbing the flow through the furnace.

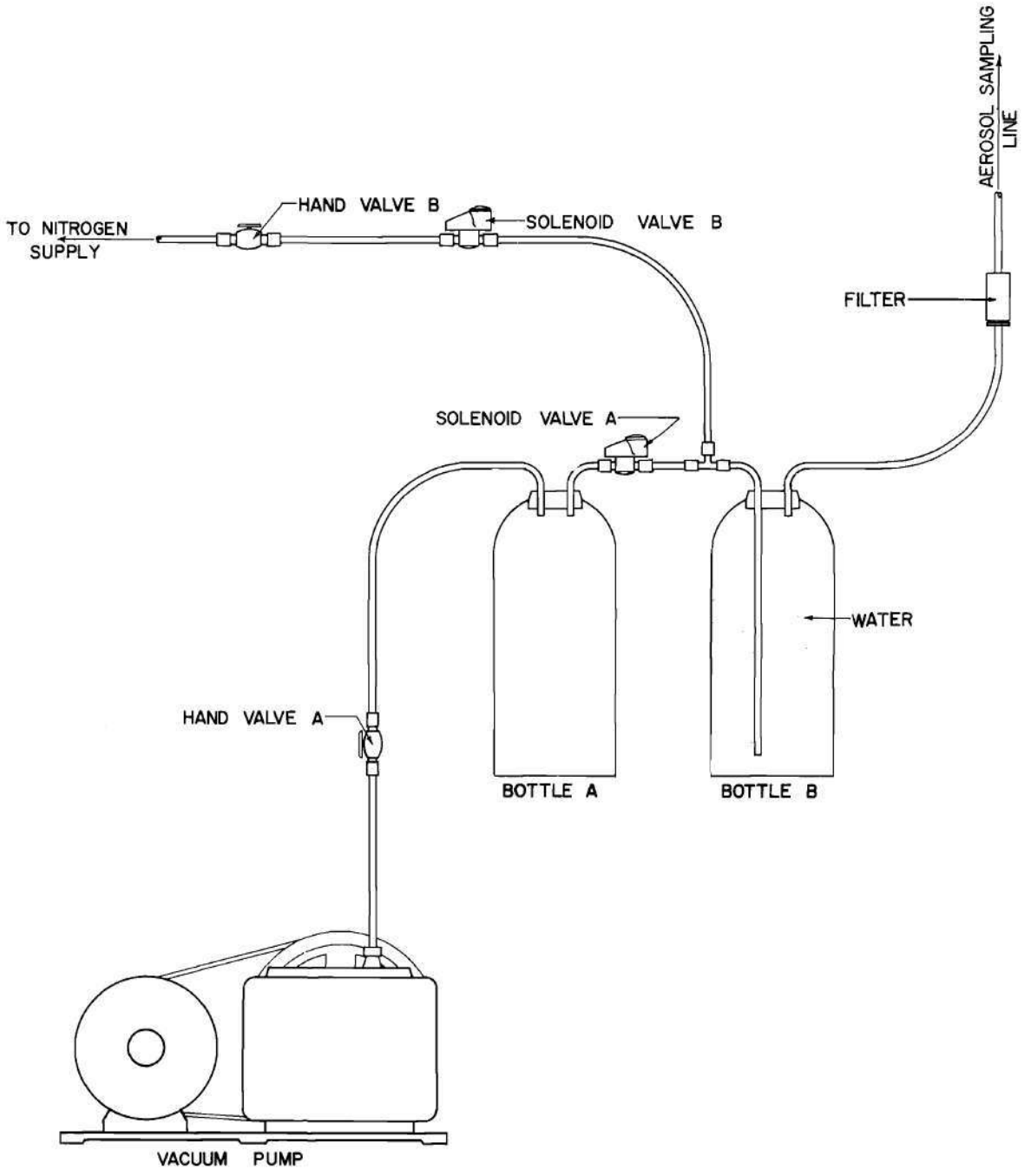

Figure 9. Sampling Apparatus for Aerosol Density Measurements

At the end of the sampling period, the sampling apparatus is shut down instantaneously by operating the double-pole switch to close valve B. Hand valves A and B are mounted on the console and solenoid valves A and B are operated remotely from the console.

The volume of water displaced from bottle B to bottle A is equal to the volume of aerosol drawn plus the volume of the filter holder and the line from the filter holder to the furnace outlet. The filter, which was weighed before sampling, is weighed again. The difference in weight divided by the corrected volume of aerosol drawn through the filter gives the concentration of the aerosol in grams of seed material per cubic centimeter of gas. During preliminary tests, the filter holder was examined for the deposition of carbon on the walls. This appeared to be negligible. An attempt was made to minimize carbon deposition on the tube walls by minimizing the distance between furnace outlet and filter holder consistent with heat removal requirements and by placing the filter holder in a vertical position, so that the sides are vertical and the filter horizontal.

Since the filter holder is rather close to the furnace outlet, the filter holder chosen was of stainless steel and the filters were of glass fiber, both capable of withstanding temperatures to 900°F. There are two sampling systems. Two samples are taken, one just before the aerosol enters the furnace and the other after it is heated.

Particle Size Distribution

It is desirable to have some idea of the size of the particles produced by the aerosol generator, or more precisely, to observe the degree of deagglomeration accomplished by the nozzle in the aerosol stream. Stan-

dard methods of collecting samples disturb the flow field in such a way that many of the smallest particles may be lost. That is, the smallest particles remain in the gas while the larger particles are collected. Since the smallest particles are lost and unobserved, an uncertainty is introduced as to just what contribution they might make to the particle size distribution, and therefore the distribution itself is uncertain.

In view of this, a method has been used which gives a general idea of the particle size distribution, even though there is some bias in favor of the heavier (i.e., larger) particles. In addition, such a measurement allows a reasonably accurate evaluation of the largest particles present. This in itself is an important piece of qualitative information – an upper limit on the size of particles in the aerosol.

One problem involved in the above sampling method for submicron-sized particles dispersed in a gaseous medium is obtaining an accurate sample of the various particle sizes in the aerosol. The simplest method of sampling is simply by introducing an electron microscope grid in a moving aerosol and allowing particles to collect upon the grid. It was felt, however, that aerodynamic effects would favor the deposition of the larger particles while the smaller particles remained in the aerosol. Similar problems existed for a gravity-based "settling out" method which would also be inaccurate due to particle reagglomeration.

A method which overcomes these problems is electrostatic sampling. In general, this means applying a high voltage across the gas. The electric field would then accelerate charged particles across the voltage drop. If the aerosol particles are charged, they will be drawn by the potential difference to one of the plates, depending on the charge.

In the actual experiment, a 75 kV Van de Graaff generator was used to provide the required voltage drop. A Plexiglas container was built with inlet and outlet ports for the gas, a needle for distribution of the negative charge obtained from the Van de Graaff generator, and a grounded metal plate upon which the metal electron microscope grids were placed. The overall arrangement is illustrated in Figure 10.

As a test of the electrostatic method, the grids were taped to a vertical side of the container so that gravity-induced precipitation would not affect the results. The grids were also located parallel to the flow, so that aerodynamic precipitation could be considered minimal.

Although some charging of the particles was assumed to result from their introduction into the aerosol, the main charging is probably due to the flow of electrons from the needle point across the gas to the grounded plate. Thus the Van de Graaff generator not only establishes the electric field but also provides the electrons which charge the particles which are then precipitated.

Detector System

The detector system consists primarily of three photomultiplier tubes. The first photomultiplier tube produces a signal proportional to the intensity of the diffracted light of a particular wavelength which has passed through the hot aerosol. The second photomultiplier produces a signal proportional to the intensity of a fixed narrow wavelength range in the ultraviolet transmitted through the aerosol to monitor the aerosol concentration. The third photomultiplier gives a signal proportional to the intensity transmitted through the aerosol just before entering the furnace.

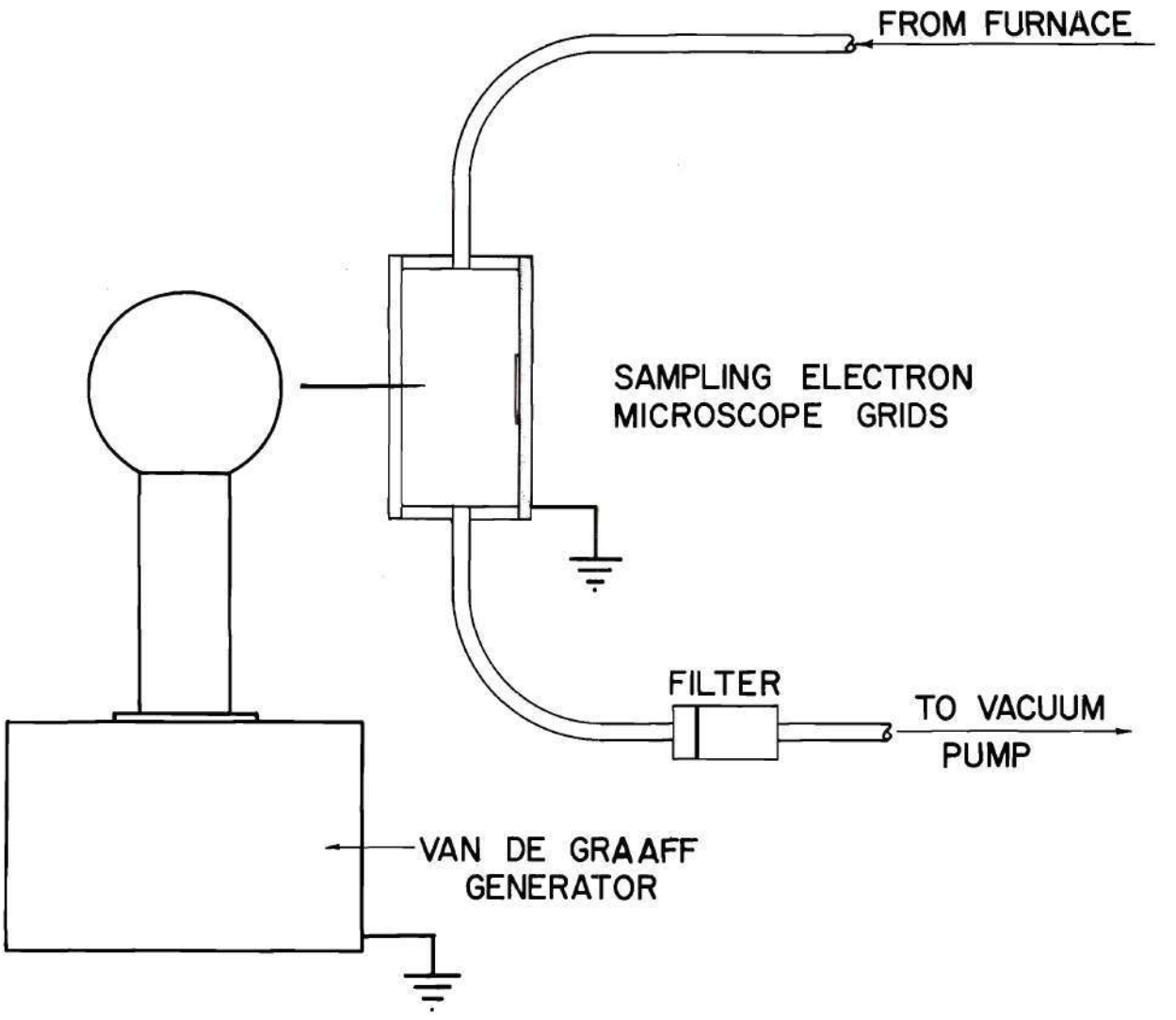

Figure 10. Electrostatic Sampling Equipment

The photomultiplier tube outputs are monitored by Keithley picoammeters. The first photomultiplier output which is wavelength dependent varies by several orders of magnitude during the scanning of the spectrum. Therefore, the output of this photomultiplier is monitored by a Keithley model 419 automatic ranging picoammeter which automatically measures currents from 10^{-13} ampere full scale to 10^{-2} ampere rapidly and accurately. The model 419 can provide an accurate reading within 320 milliseconds for a measurement requiring one range change. With six range changes, less than one second is required for a complete measurement.

The output of all three picoammeters is recorded by a Honeywell model 906 C Direct Recording Visicorder oscillograph. The visicorder is similar to conventional oscillographs in that signals from the picoammeters enter at the galvanometer inputs and are recorded by moving beams of light from mirror galvanometers focused on light sensitive paper.

Control System

A control system capable of operating the experimental equipment from a remote location is required for safety considerations. The operating station is located in front of an aluminum wall constructed to shield personnel from the equipment containing hot hydrogen. The design philosophy is to provide remote operation for all equipment functions that need to be varied during data collection or while either hydrogen gas is flowing or the heater element is energized.

The control system is interlocked with a safety "SCRAM" system that controls electrical power to the equipment. In the event of a power failure or a "SCRAM" signal, all electrical power to the equipment is inter-

rupted and locked off until manually reset. Interrupting the electrical power deactivates a system of normally closed solenoid valves on all hydrogen gas lines and also the high pressure gas lines. The water coolant to the furnace and the exhaust fan remain on.

The electrical system functions to control and distribute electrical power, provide remote control of the spectrometer drive mechanism, monitor those measurements such as flow rates and temperatures during data collection, and transmit data to remote recording devices. The control panel shown in Figure 1 serves as a control and distribution point for all electrical power. The safety system furnishes three phase 220 VAC and single phase 115 VAC through the primary "SCRAM" power contactors to bus terminals in the control panel. The 220 VAC is moderated by a large variac which controls the rectifier for the heater power. This 220 VAC variac is located at the control desk. All direct current power supplies and amplifiers are fed through switches at the control desk.

Gas System

The gas system is shown in Figure 11. All gas required for the experiment is passed through solenoid valves which can be controlled remotely from the control console. Hydrogen for the light source is controlled by a needle valve. Hydrogen for the side ports flows through Matheson flowmeters and is controlled by needle valves on the flowmeters. Two manifolds supply the nitrogen for purging and hydrogen gas for the main flow. The manifolds permit the connection of several cylinders to one line, permitting a larger, continuous supply of gas during the experiment. By using manifolds, the empty cylinders can be replaced without interrupting the

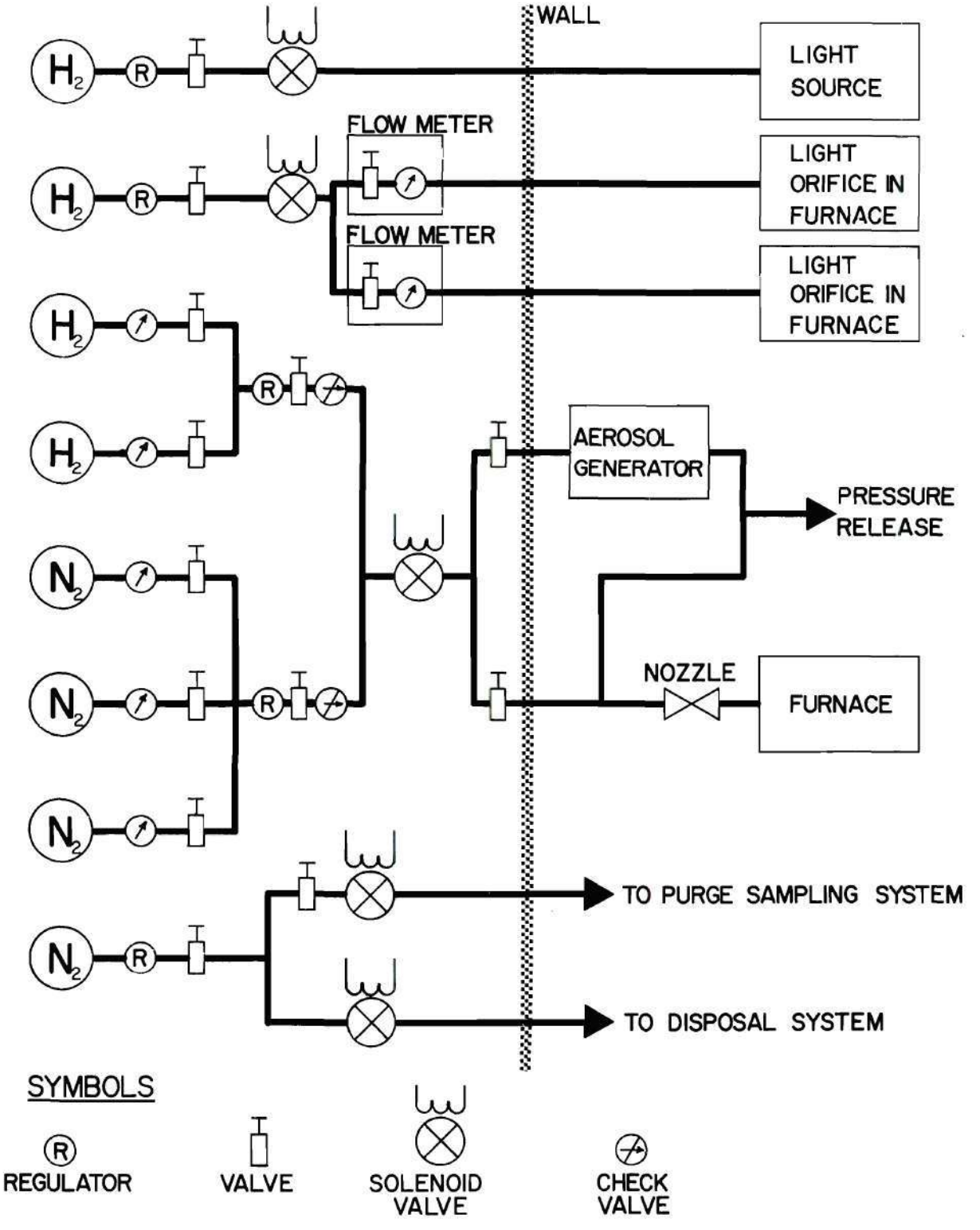

Figure 11. Gas System

experiment. A cylinder of nitrogen supplies nitrogen to purge the sampling system and to pressurize the disposal system.

Disposal System

The exhaust from the furnace is connected to a disposal system outside the building by a one and one-half inch diameter stainless steel flexible hose and copper tube. The hot seeded hydrogen, after passing through the furnace, is bubbled through the disposal tank as shown in Figure 11. The effluent disposal system consists of a 55 gallon drum which is partially filled with water. When the hydrogen with submicron-sized particles is bubbled through the water, the particles remain in the water and hydrogen bubbles rise to the surface. A blower directs air onto the surface to dilute the hydrogen by a factor of several hundred and expels it to the atmosphere. The water trap also prevents air from diffusing back into the furnace and creates a back pressure. The creation of this slight positive pressure prevents air from getting into the system should a leak occur.

CHAPTER III

SAFETY ASPECTS

This experiment involves not only the normal safety problems encountered in experimental work but also has a major one imposed by the use of large quantities of compressed nitrogen and hydrogen. Both the explosive nature of the hydrogen and the hazard associated with compressed gas in general had to be taken into account in planning for safe working conditions. As with any explosive gas, two approaches to safety must be considered. The first deals with preventing a dangerous situation from occurring and the second with preventing injury to personnel if one does occur. Both of these are reflected in the safety aspects of this experiment.

Standard operational procedures exist for using both compressed gases and hydrogen, but, in the case of the latter, they are often designed for large operations in which specially constructed facilities are used. Such facilities are not available at Georgia Tech, so the existing laboratory space had to be modified to provide safe working and storage areas. As with any arrangement of this type, the physical layout of the labs imposed restrictions on what could be done. However, within these limitations, a working environment was created in which the experimental operations could be carried out with a great degree of safety.

The safety aspects initiated for this project have been divided into three areas: hydrogen safety, compressed gases safety, and miscel-

laneous safety.

Hydrogen Safety

Although there are other considerations, as mentioned before, the major safety problem encountered by this project stems from the use of hydrogen gas. In planning a program to deal with this, the following approaches to safety were considered.

1. Inherent Safety. This is the most basic and probably the most important approach to the problem. It simply means that, in the design and building of the experimental equipment, care is taken to build in safety. Specific areas to be taken into consideration are leak prevention, adequate ventillation, and elimination of ignition sources. If any one of these areas were to completely satisfy all safety standards, there would be no problem. However, in most situations, practical and financial considerations generally make this an impossibility and a compromise involving all three is used. Such a compromise is feasible because each area complements the other two. That is, a weakness in one can be compensated for by the others. For this work, the elimination of all ignition sources is impossible. This is partly due to the practical difficulties involved. In fact, since hot hydrogen is being used, a high degree of safety in this area is virtually impossible without the use of some sort of inert atmosphere system.

2. Secondary Safety. This concerns design considerations involved in preventing a given failure of an inherent safety feature from becoming a danger to personnel and equipment. Examples are protective walls and hydrogen detection equipment.

3. System Control. This simply means that the control of the experiment is designed both to prevent operator error and at the same time to give the operator sufficient control to react quickly to any dangerous situation that might occur.

The implementation of these safety approaches is now considered in five major operational areas.

Atmospheric Controls

The most obvious problem when using hydrogen is that of leakage creating an explosive condition. For this reason, the project laboratory utilizes a large capacity exhaust fan which, combined with proper ventillation, prevents the buildup of any explosive mixture. The problem is made simpler by the fact that only about one half cubic foot per minute of gas is being used. As an added precaution, the furnace, which could be expected to cause the most trouble, lies in a semi-enclosed hood area at the top of which is located the exhaust fan. This maximizes ventillation in that area. As a check, when the system is operating, the hydrogen content of the air is periodically monitored with a portable instrument. Needless to say, all precautions were taken during design and fabrication stages to minimize the chance of leakage.

Effluent Disposal

The hot hydrogen, after passing through the furnace, is bubbled through a water trap, diluted with air by a factor of several hundred, and then expelled to the atmosphere. Figure 12 shows the effluent disposal system. The water trap serves a dual purpose in that it prevents air from diffusing back into the furnace as well as creating a back pressure which helps prevent air from getting into the system should a leak occur.

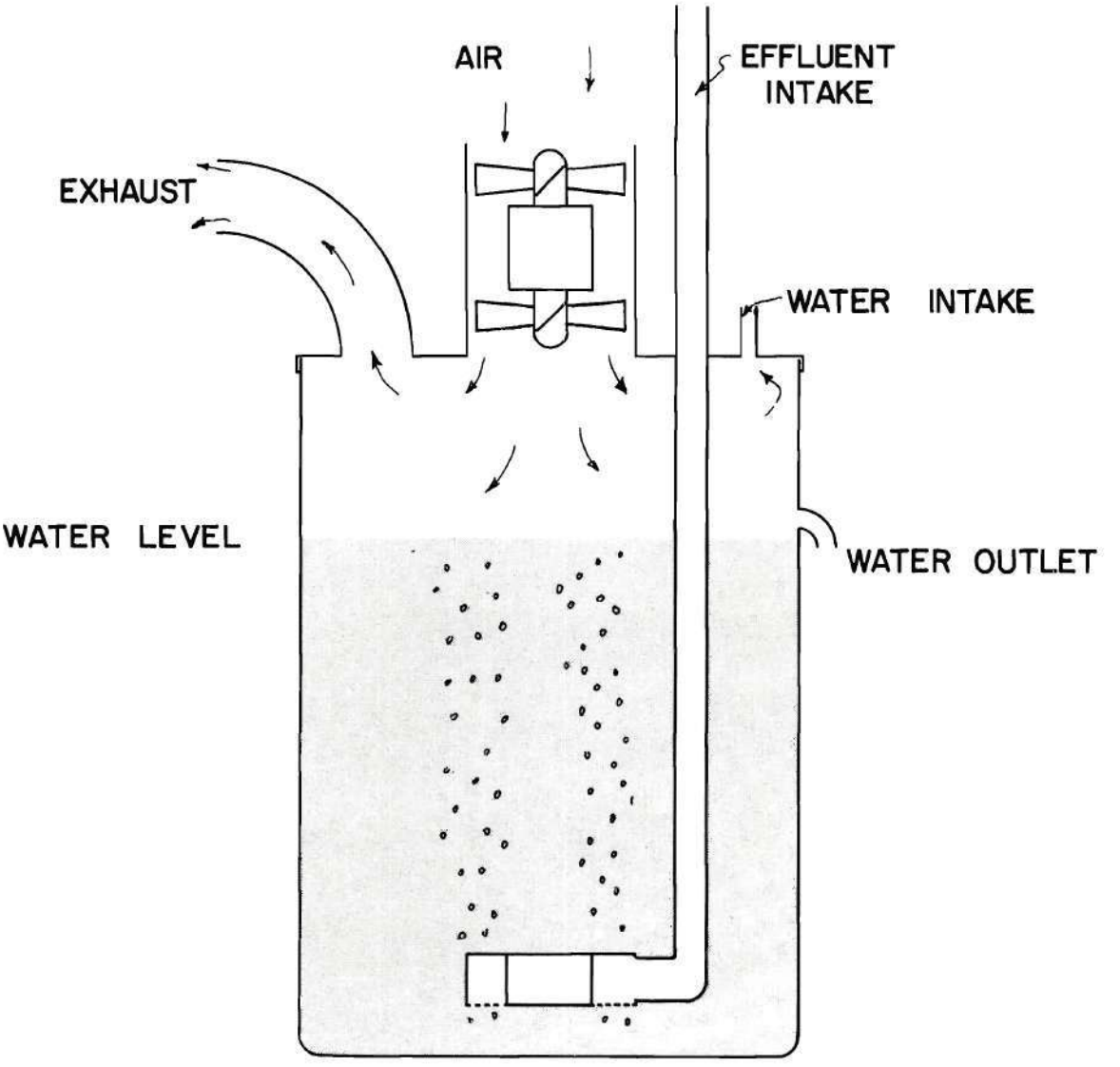

Figure 12. Disposal System

Furnace Safety

The major problem that could arise with the furnace, besides leakage which has already been considered, is that some malfunction might cause overheating to the point of structural failure. To prevent this, the valves controlling the cooling water and nitrogen are wired such that the furnace cannot operate unless they are open. In addition, the furnace temperature is monitored to detect any overheating.

SCRAM System

The SCRAM system designed for this experiment has a twofold purpose: to provide a means of putting the equipment into a safe shutdown mode on short notice and to help prevent possibly dangerous operator errors. The first of these means that, when the SCRAM is initiated, the ventillation and effluent disposal systems remain on while all other equipment is turned off. The purpose of this is to remove possible ignition sources for any hydrogen that might be present while providing means of removing it from the area. This is done utilizing four power relays through which all current that is to be controlled is passed, as shown in Figure 13. The current to the furnace is handled indirectly by a separate relay which is utilized to control still another relay which forms part of the safety interlock on the main power supply. When a SCRAM is initiated, all relays go into their normally off position. It is also noted that a power failure or interruption of any kind also activates the system. The system is designed such that once a SCRAM has occurred, it must be manually reset before further operations can be carried out. This feature serves to prevent the equipment from accidentally being turned on after a SCRAM. All solenoid valves are wired such that the off position represents their

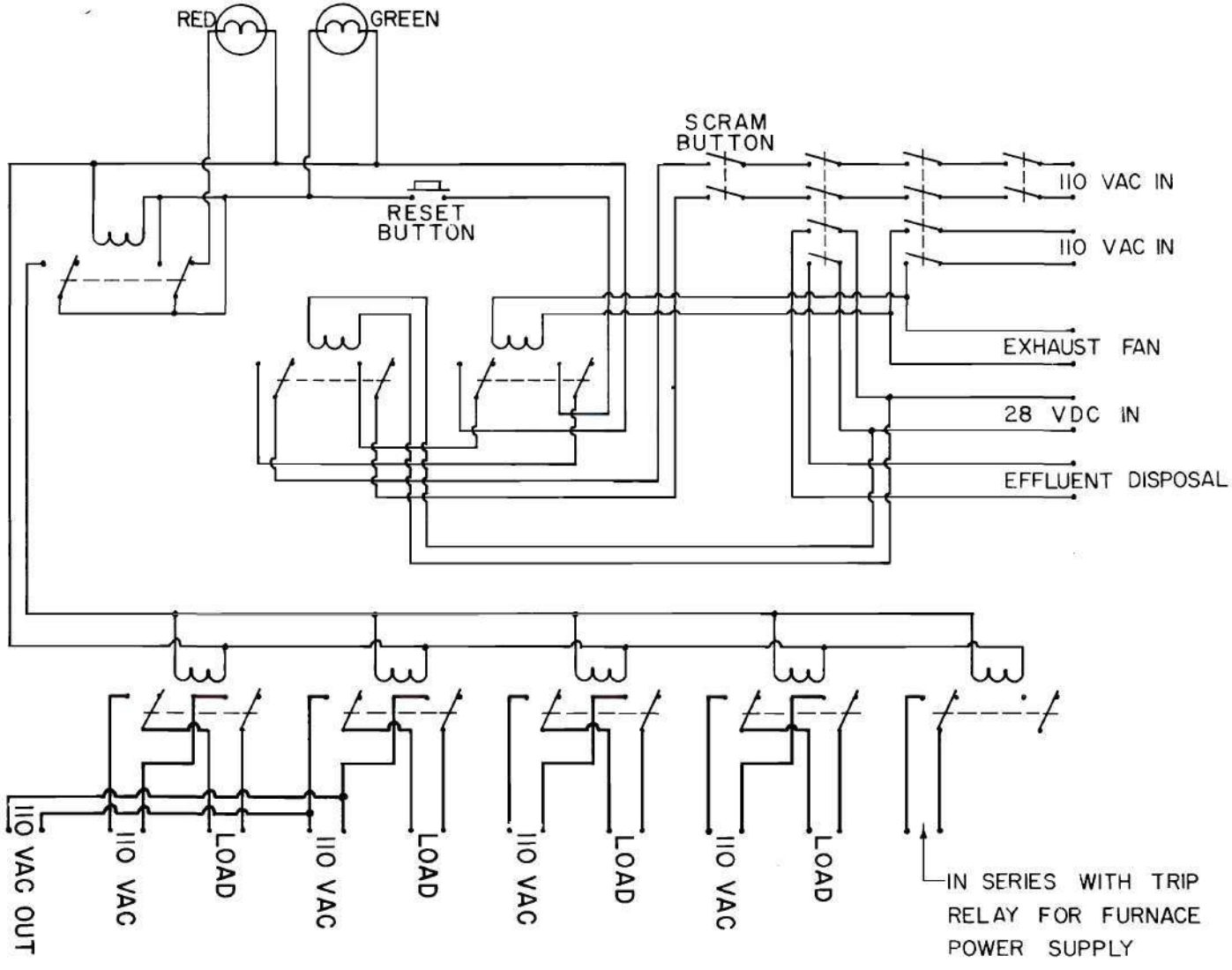

Figure 13. SCRAM System

SCRAM mode.

The second purpose of the system is to prevent operator errors and/or equipment failures from creating unsafe conditions during and after startup. This area of concern includes power failures, power supply failures, and operators forgetting to turn on the effluent and ventillation systems or accidently turning them off during a run. This is accomplished by using a simple logic circuit that prevents the experimental equipment from being activated until several necessary actions have been taken. The following is a list of events that must constitute the startup procedure.

1) SCRAM main switch must be turned on.
2) Exhaust fan must be turned on.
3) Exhaust fan must receive proper voltage.
4) Effluent disposal system must be turned on.
5) Effluent disposal fan must receive proper voltage.
6) SCRAM button must be turned to ON position.

After the above have been accomplished in any order, the final step is:

7) The reset button is pushed.

All relays controlling power to the equipment will now be closed. If, at any time during operation, one of the above actions is negated, a SCRAM will automatically occur.

Secondary Safety

Taking into account the unlikely possibility that all preventive measures fail, an aluminum wall has been constructed between the furnace and its associated equipment and the operator area, as shown in Figures 1 and 2. This wall forms part of the semi-enclosed hood previously mentioned.

Structurally the wall consists of an aluminum girder frame on which two layers of aluminum plate are bolted. The plate thickness varies with the heaviest (one fourth inch) being used in the areas near the furnace. A double thickness Plexiglas window was placed in the wall to allow observation of the equipment while operating. The wall was not designed to contain a major explosion, but rather to protect against a localized explosion that could conceivably occur if oxygen were to somehow get into the system and become mixed with hydrogen.

Compressed Gas Safety

As mentioned before, there exist standard operational procedures for the safe use of compressed gases. Most of these simply require using care when handling gas under pressure, but some need special consideration. For instance, if tubing carrying high pressure were to break loose, it could act like a whip causing injury to nearby personnel. This is most dangerous for tubing that leads directly from a bottle of gas without first going through a valve or regulator. For this reason, all lines going from bottles to the manifolds are chained down. The bottles themselves are chained to the wall.

Storage of the gas also presented a problem especially for the hydrogen. As no suitable outside storage areas existed, the bottles of gas had to be kept inside. This was done keeping them wired together to prevent any from falling over. They were placed in a room under a plastic hood that is vented to the outside by two independent exhaust fans. This was done to prevent the buildup of any hydrogen that might leak out. The two exhaust fans remain on whenever hydrogen tanks are stored in this area.

Miscellaneous

Another safety system was added after an unexpected accident showed that it was desirable. The magnesium fluoride window between the furnace and the spectrometer broke and allowed the pumping system of the spectrometer to create a vacuum in the furnace. This caused water to be sucked from the effluent disposal system into the furnace and monochromator. This occurred during initial operations so only a very great mess resulted. If it had occurred during full operation, hydrogen would have been pumped into the atmosphere. The thermal shock to the furnace caused by the water could also be of sufficient magnitude to cause possible failure. To prevent this from reoccurring, a vacuum switch has been connected to the effluent disposal pipe so that any suction in the pipe will activate a switch. When this happens, the vacuum pump is automatically turned off and nitrogen at 20 psi is forced into the pipe. This serves to equalize the pressure and prevent hydrogen from being pumped into the experimental area and to protect the furnace. The switch is wired such that, once it has been actuated, it must be manually reset. Figure 14 shows a schematic diagram of the vacuum sensing and pressurization system.

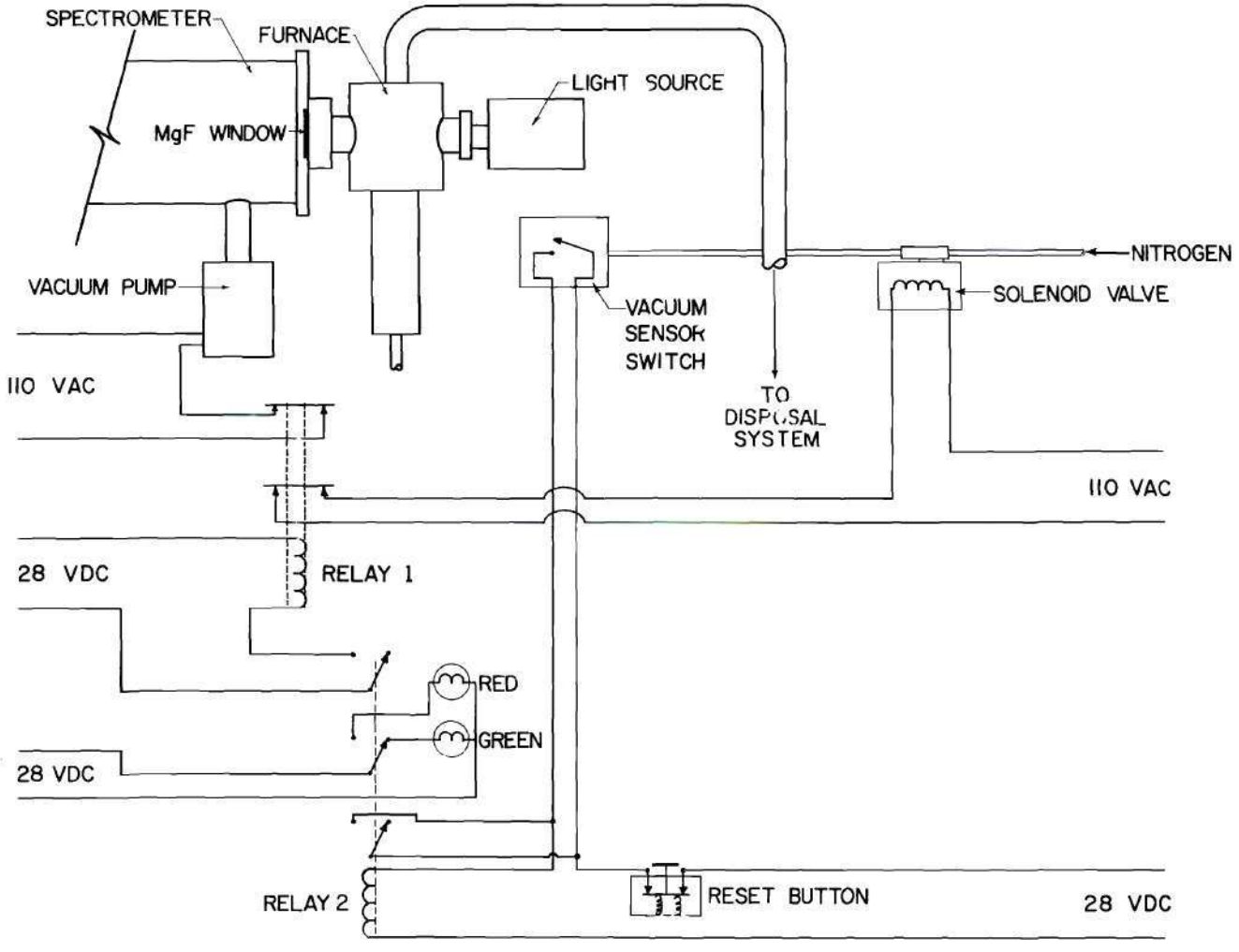

Figure 14. Vacuum Sensing and Pressurization System

CHAPTER IV

EXPERIMENTAL PROCEDURE

The procedure for taking data is outlined in detail in Appendix A. The experiment may be divided into three parts: light transmission measurements, aerosol density measurements, and temperature measurements. In addition to these measurements, a number of flow meters, electrical meters, and gauges are monitored.

Light Transmission Measurements

To take data, one must first purge the entire system with nitrogen and then hydrogen heated to the desired temperature. Then the ultraviolet light is adjusted to the required intensity. A switch at the console turns on the visicorder and the drive mechanism which rotates the grating at constant speed. At the end of the spectrum scan, the drive motor is reversed by a limit switch. During the reverse scan, the shutter between the furnace and the light source is closed so that the intensity of the background radiation from the hot interior of the furnace is measured as a function of wavelength. When the grating returns to the original position, another limit switch reverses the drive mechanism and stops the motor. The experiment is repeated with particles in the gas and again without particles, to make sure that the intensities return to the same value. The last scan assures that the light path has not become partially clogged during the run with particles.

The resulting traces from photomultiplier 1 are a plot of intensity versus wavelength with and without particles in the gas and the wavelength dependent background from the furnace. Photomultiplier 2 produces a plot of intensity monitoring changes in the aerosol concentration. The third photomultiplier monitors the aerosol concentration at the entrance of the furnace (before heating) so that at higher temperatures the disappearance of particles can be verified.

Since the photomultiplier output is proportional to the intensity of the light falling on it, the linear attenuation coefficient at a given wavelength is calculated from the ratio of light intensities from photomultiplier 1 with and without particles in the gas after the background due to the glow of the furnace is subtracted.

Aerosol Density Measurements

The density of the aerosol is measured by withdrawing a known volume of aerosol through a filter. There are two sampling systems, one just before the aerosol enters the furnace and the other just before it exhausts from the furnace. One inch diameter fiberglass filters are weighed initially and placed in the filter holder. Just before sampling, the sampling bottles are purged with nitrogen. The sample is pulled at the same time that the spectrum is scanned with particles in the hydrogen. The plot of intensity from photomultiplier 2 is then used to correct for any changes in the aerosol concentration. The mass attenuation coefficient is calculated by dividing the linear attenuation coefficient obtained from photomultiplier 1 by the aerosol density.

The aerosol is simultaneously sampled before and after it is heated

to establish the percent of the particles that has disappeared due to chemical reactions. Simultaneous samples were taken at various temperatures for hydrogen-carbon and hydrogen-tungsten aerosols to investigate the disappearance of particles at elevated temperatures.

Temperature Measurements

The temperature of the hot aerosol is measured using two tungsten tungsten-rhenium thermocouples, one just below and the other just above the light path. The average of these two temperatures is taken to be the temperature at which the attenuation coefficient is measured. The output of the thermocouples is displayed by a digital voltmeter. The temperature during the course of the experiment is kept constant by changing the heater voltage on the heating element when such changes are needed.

There are a number of gauges, flow meters, and electrical meters which are monitored frequently to ensure correct operating conditions.

CHAPTER V

DATA REDUCTION AND ANALYSIS

The signals from the three photomultiplier tubes recorded by the Honeywell visicorder are analyzed to calculate the linear attenuation coefficient of the aerosol at a given temperature for various radiation wavelengths. The mass attenuation coefficient is calculated by dividing the linear attenuation coefficient by the aerosol density. Figure 15 shows a plot of the signals from the three photomultipliers in three sections. The first section represents the run with pure hydrogen without any particles, the second section represents the run with particles in the gas, and the third section represents a second run without particles. This last run is to make sure that no seed material has been deposited in the light path. In each section, the spectrum is scanned twice; first, in the forward direction and then in the reverse direction. During the forward scan, the shutter between the light source and the furnace is open so that photomultipliers 1 and 2 measure both the light and the thermal background radiation from the furnace. During the reverse scan, the shutter between the light source and the furnace is closed so that photomultipliers 1 and 2 measure only the thermal background from the furnace. The thermal background is more significant at higher temperatures, especially when particles are in the gas.

During the run with particles in the gas, samples are taken during the forward scan. Each scan takes exactly the same length of time, about

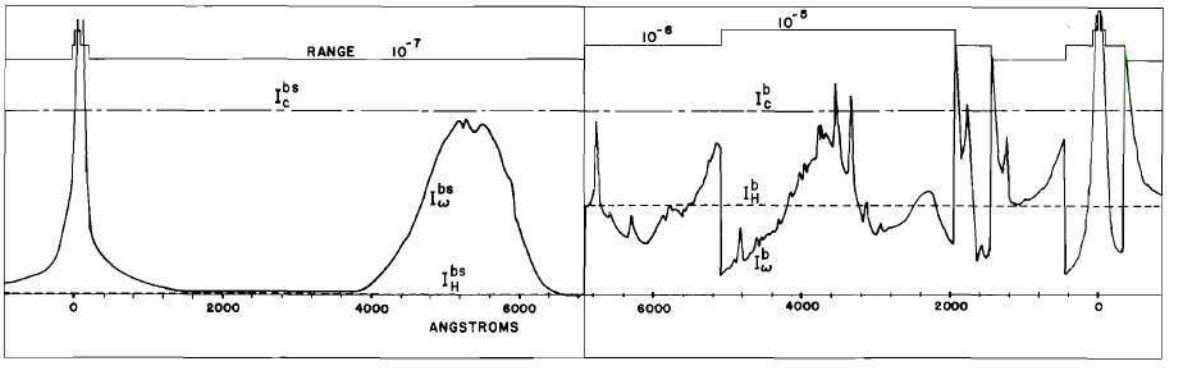

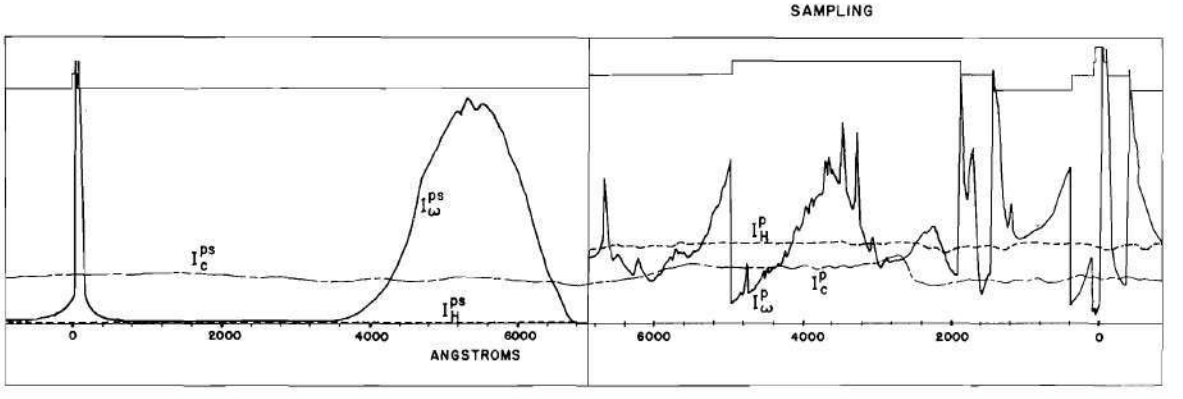

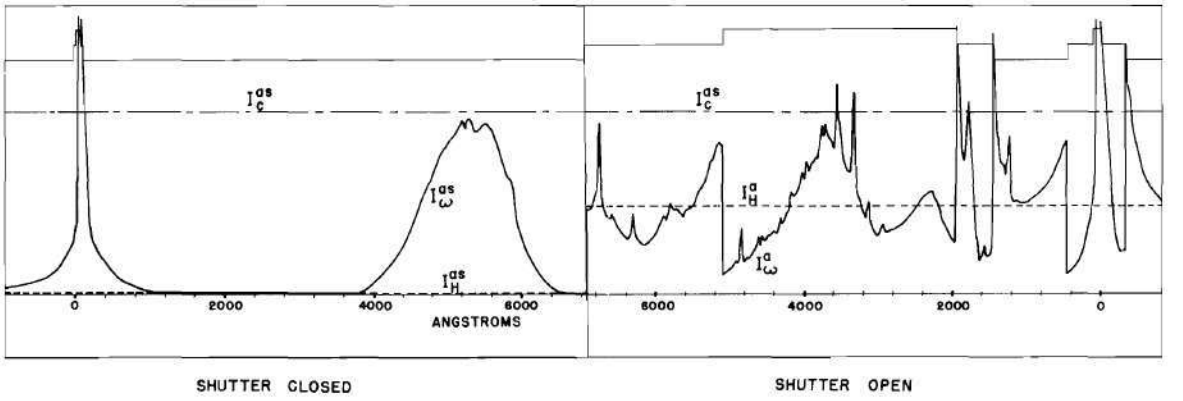

Figure 15. Oscillograph Output

25 seconds. Since the synchronous motor which turns the grating runs at a constant speed, a linear plot of wavelength versus intensity is obtained from the photomultiplier 1 signal recorded by the oscillograph. The wavelength scale is evaluated from two known wavelengths. Since the grating is used at nearly normal incidence, the "white point," a sharp increase in intensity when the grating is at normal incidence, corresponds to zero wavelength. The second position is at a known line in the hydrogen spectrum. The following lines in the hydrogen spectrum can be used to evaluate the wavelength.

Series	Line	Wavelength
"White point"		0
Lyman	Alpha	1216 Å
Balmer	Delta	4102 Å
Balmer	Gamma	4341 Å
Balmer	Beta	4861 Å
Balmer	Alpha	6563 Å

In order to calculate the mass attenuation coefficient at various wavelengths, the intensities from the three photomultiplier tubes with and without particles in the gas are read from the plots.

For the initial run without particles (before), let

I_{ω}^{b} = intensity of photomultiplier 1 with shutter open

I_{H}^{b} = intensity of photomultiplier 2 with shutter open

I_{c}^{b} = intensity of photomultiplier 3 with shutter open

I_{ω}^{bs} = intensity of photomultiplier 1 with shutter closed

I_{H}^{bs} = intensity of photomultiplier 2 with shutter closed

I_c^{bs} = intensity of photomultiplier 3 with shutter closed

For the run with particles in the gas

I_ω^p = intensity of photomultiplier 1 with shutter open

I_H^p = intensity of photomultiplier 2 with shutter open

I_c^p = intensity of photomultiplier 3 with shutter open

I_ω^{ps} = intensity of photomultiplier 1 with shutter closed

I_H^{ps} = intensity of photomultiplier 2 with shutter closed

I_c^{ps} = intensity of photomultiplier 3 with shutter closed

For the second run without particles in the gas (after), let

I_ω^a = intensity of photomultiplier 1 with shutter open

I_H^a = intensity of photomultiplier 2 with shutter open

I_c^a = intensity of photomultiplier 3 with shutter open

I_ω^{as} = intensity of photomultiplier 1 with shutter closed

I_H^{as} = intensity of photomultiplier 2 with shutter closed

I_c^{as} = intensity of photomultiplier 3 with shutter closed

The wavelength is used as the independent variable instead of time for convenience. Thus, $I_H^b(\lambda)$ is the intensity of the second photomultiplier signal when photomultiplier 1 is observing light of wavelength λ, and so forth. Let

$\rho_H(\lambda)$ = aerosol density of hot aerosol at wavelength λ

$\rho_c(\lambda)$ = aerosol density of cold aerosol at wavelength λ and

$\rho_c^s(\lambda)$ = aerosol density of cold aerosol at wavelength λ during the reverse scan when the shutter is closed

The mass attenuation coefficient, $\mu(\lambda)$, is calculated from

$$\mu(\lambda) = \frac{K(\lambda)}{\rho_H(\lambda)} \tag{9}$$

The calculation of the mass attenuation coefficient is in two parts: the calculation of the linear attenuation coefficient, $K(\lambda)$ and the calculation of the hot aerosol density, $\rho_H(\lambda)$.

Calculation of Linear Attenuation Coefficient

The linear attenuation coefficient is given by

$$K(\lambda) = \frac{1}{X} \ln \left[\frac{I_\omega(\lambda)}{I_{\omega B}^p(\lambda)}\right] \tag{10}$$

where

X = aerosol path width

$I_\omega(\lambda)$ = average intensity without particles corrected for thermal background

$$= \tfrac{1}{2} \left[(I_\omega^b(\lambda) - I_\omega^{bs}(\lambda)) + (I_\omega^a(\lambda) - I_\omega^{as}(\lambda)) \right] \tag{11}$$

$I_{\omega B}^p(\lambda)$ = average intensity with particles corrected for thermal background

$$= I_\omega^p - \text{(background due to glow in furnace + background due to emission by particles)} \tag{12}$$

Half of the glow from the furnace is assumed to come from the front of the particle cloud and half from the back of the particle cloud which is attenuated by $\frac{I^{p}_{HB}(\lambda)}{I_H}$

where

$$I_H = \tfrac{1}{2}[(I^{b}_{H} - I^{bs}_{H}) + (I^{a}_{H} - I^{as}_{H})] \tag{13}$$

$$I^{p}_{HB}(\lambda) = I^{p}_{H}(\lambda) - I^{ps}_{H}(\lambda) \otimes \frac{\rho_c(\lambda)}{\rho^{s}_{c}(\lambda)} \tag{14}$$

Therefore

$$\text{Background due to glow of furnace} \tag{15}$$
$$= \tfrac{1}{4}[I^{bs}_{\omega}(\lambda) + I^{as}_{\omega}(\lambda)] + \tfrac{1}{4}[I^{bs}_{\omega}(\lambda) + I^{as}_{\omega}(\lambda)] \times \frac{I^{p}_{HB}(\lambda)}{I_H}$$

$$= \tfrac{1}{4}\left(I^{bs}_{\omega}(\lambda) + I^{as}_{\omega}(\lambda)\right)\left(1 + \frac{I^{p}_{HB}(\lambda)}{I_H}\right)$$

The background due to the particles is proportional to the particle density.

$$\text{Background due to emission by particles} \tag{16}$$
$$= (\text{total background} - \text{background due to glow}) \times \frac{\rho_c(\lambda)}{\rho^{s}_{c}(\lambda)}$$

$$= \left[I^{ps}_{\omega}(\lambda) - \tfrac{1}{4}(I^{bs}_{\omega}(\lambda) + I^{as}_{\omega}(\lambda))\left(1 + \frac{I^{p}_{HB}(\lambda)}{I_H}\right)\right] \otimes \frac{\rho_c(\lambda)}{\rho^{s}_{c}(\lambda)}$$

Substituting equations (15) and (16) into equation (12)

$$I^{p}_{\omega b}(\lambda) = I^{p}_{\omega}(\lambda) - I^{ps}_{\omega}(\lambda) \times \frac{\rho_c(\lambda)}{\rho^{s}_{c}(\lambda)} \tag{17}$$

$$+ \tfrac{1}{4}(I^{bs}_{\omega}(\lambda) + I^{as}_{\omega})\left(1 + \frac{I^{p}_{HB}(\lambda)}{I_H}\right)\left(\frac{\rho_c(\lambda)}{\rho^{s}_{c}(\lambda)} - 1\right)$$

Evaluating equations (11) and (17), the linear attenuation coefficient is calculated by equation (10).

Calculation of Aerosol Densities

The aerosol density measured using the sampling system is the average aerosol density during forward scan with particles and from this $\rho_H(\lambda)$, $\rho_c(\lambda)$, and $\rho^{s}_{c}(\lambda)$ can be calculated using the intensity plots. The average aerosol density is given by

$$\rho_c = \frac{1}{T}\int_{o}^{T} \rho_c(t)\, dt \tag{18}$$

where T = sampling time

When $\rho_c(t)$ does not change much over the time intervals Δt_i and $T = \sum_{i=1}^{N} \Delta t_i$, then

$$\rho_c = \frac{1}{T}\sum_{i=1}^{N} \rho_c(t_i)\, \Delta t_i \tag{19}$$

Since the wavelength is proportional to time during scanning

$$\rho_c = \frac{1}{L}\sum_{i=1}^{N} \rho_c(\lambda_i)\, \Delta\lambda_i \tag{20}$$

where $L = \sum_{i=1}^{N} \Delta\lambda_i$

Now

$$\frac{I_c}{I_c^p(\lambda_i)} = e^{\mu_c x\, \rho_c(\lambda_i)} \tag{21}$$

where μ_c is not a function of λ since I_c results from the light of one wavelength.

$$I_c = \tfrac{1}{2}(I_c^b + I_c^a) \tag{22}$$

Therefore

$$\rho_c(\lambda_i) = \frac{1}{\mu_c x} \ln \frac{I_c}{I_c^p(\lambda_i)} \tag{23}$$

Substituting equation (23) into (20)

$$\rho_c = \frac{1}{\mu_c x\, L} \sum_{i=1}^{N} \left(\ln \frac{I_c}{I_c^p(\lambda_i)}\right) \Delta\lambda_i \tag{24}$$

For any wavelength λ

$$\frac{I_c}{I_c^p(\lambda)} = e^{\mu_c x\, \rho_c(\lambda)}$$

Therefore

$$\rho_c(\lambda) = \frac{1}{\mu_c x} \ln \frac{I_c}{I_c^p(\lambda)} \tag{26}$$

Substituting $\frac{1}{\mu_c x}$, from equation (24)

$$\rho_c(\lambda) = \frac{\rho_c L}{\sum_{i=1}^{N} \left(\ln \frac{I_c}{I_c^p(\lambda_i)} \right) \Delta\lambda_i} \cdot \ln \frac{I_c}{I_c^p(\lambda)} \tag{27}$$

Defining a constant R_c

$$R_c = \frac{\rho_c L}{\sum_{i=1}^{N} \left(\ln \frac{I_c}{I_c^p(\lambda_i)} \right) \Delta\lambda_i} \tag{28}$$

The cold aerosol density at any wavelength λ is expressed as

$$\rho_c(\lambda) = R_c \ln \frac{I_c}{I_c^p(\lambda)} \tag{29}$$

similarly

$$\rho_c^s(\lambda) = R_c \ln \frac{I_c}{I_c^{ps}(\lambda)} \tag{30}$$

A similar analysis can be made for the hot aerosol density which gives

$$\rho_H(\lambda) = R_H \ln \frac{I_H}{I_{HB}^p(\lambda)} \tag{31}$$

where

$$R_H = \frac{\rho_H L}{\sum_{i=1}^{N} \left(\ln \frac{I_H}{I_{HB}^p(\lambda_i)} \right) \Delta\lambda_i} \tag{32}$$

$I^{p}_{HB}(\lambda)$ is given by equation (14).

Using equation (10), $K(\lambda)$ is calculated and using equation (31), $\rho_H(\lambda)$ is calculated. Substituting in equation (9), the mass attenuation coefficient may now be evaluated for various wavelengths.

A computer program is presented in Appendix B which calculates the mass attenuation coefficient at various wavelengths and the computer output of a sample calculation is also given in Appendix B.

Error Analysis

Error is defined as the difference between a calculated or measured value and the true value. Usually the true value is not known and, therefore, an error is estimated. The fact that an error occurs is due to the fact that we can only determine the results with a given uncertainty. The most prominent type of uncertainty results from fluctuations in data from which the mass attenuation coefficient is calculated. The uncertainty in each data point is estimated depending upon the equipment and the method of recording it. Starting with the uncertainty in the data, the propagation of these uncertainties to the final result is calculated.

The percentage uncertainty in the three photomultiplier signals is carefully estimated. The percentage uncertainty in the measurement of the aerosol density is also evaluated. From these values, the percentage error in the mass attenuation coefficient is calculated.

If G is a function of independent variables x, y, and z and if the error in x, y, and z is known, then the error ΔG in G is calculated as follows.

If $$G = f(x,y,z)$$

then

$$(\Delta G)^2 = \left(\frac{\partial f}{\partial x}\,\Delta x\right)^2 + \left(\frac{\partial f}{\partial y}\,\Delta y\right)^2 + \left(\frac{\partial f}{\partial z}\,\Delta z\right)^2$$

and

$$\left(\frac{\Delta G}{G}\right)^2 = \frac{\left(\frac{\partial f}{\partial x}\,\Delta x\right)^2 + \left(\frac{\partial f}{\partial y}\,\Delta y\right)^2 + \left(\frac{\partial f}{\partial z}\,\Delta z\right)^2}{[f(x,y,z)]^2}$$

Now error in the mass absorption coefficient is calculated as follows.

From equation (9)

$$\mu(\lambda) = \frac{K(\lambda)}{\rho_H(\lambda)}$$

so

$$\left(\frac{\Delta\mu(\lambda)}{\mu(\lambda)}\right)^2 = \left(\frac{\Delta K(\lambda)}{K(\lambda)}\right)^2 + \left(\frac{\Delta\rho_H(\lambda)}{\rho_H(\lambda)}\right)^2 \qquad (33)$$

From equation (10)

$$K(\lambda) = \frac{1}{x}\ln\frac{I_\omega(\lambda)}{I^p_{\omega b}(\lambda)}$$

so

$$\left(\frac{\Delta K(\lambda)}{K(\lambda)}\right)^2 = \frac{1}{\ln\left(\frac{I_\omega(\lambda)}{I^p_{\omega b}(\lambda)}\right)^2} \times \left\{\left(\frac{\Delta I_\omega(\lambda)}{I_\omega(\lambda)}\right)^2 + \left(\frac{\Delta I^p_{\omega b}(\lambda)}{I^p_{\omega b}(\lambda)}\right)^2\right\} + \left(\frac{\Delta x}{x}\right)^2 \qquad (34)$$

From equation (21)

$$I_\omega(\lambda) = \tfrac{1}{2}(I^b_\omega(\lambda) - I^{bs}_\omega(\lambda) + I^a_\omega(\lambda) - I^{as}_\omega(\lambda))$$

so

$$\left(\frac{\Delta I_\omega(\lambda)}{I_\omega(\lambda)}\right)^2 = \frac{(\Delta I_\omega^b(\lambda))^2 + (\Delta I_\omega^{bs}(\lambda))^2 + (\Delta I_\omega^a(\lambda))^2 + (\Delta I_\omega^{as}(\lambda))^2}{(I_\omega^b(\lambda) - I_\omega^{bs}(\lambda) + I_\omega^a(\lambda) - I_\omega^{as}(\lambda))^2} \tag{35}$$

From equation (12)

$$I_{\omega b}^p(\lambda) = I_\omega^p(\lambda) - I_\omega^{ps}(\lambda)\,\frac{\rho_c(\lambda)}{\rho_c^s(\lambda)} + \tfrac{1}{4}(I_\omega^{bs}(\lambda) + I_\omega^{as}(\lambda))$$

$$\cdot \left(1 + \frac{I_{HB}^p(\lambda)}{I_\omega(\lambda)}\right)\left(\frac{\rho_c(\lambda)}{\rho_c^s(\lambda)} - 1\right)$$

Let $A = I_\omega^p(\lambda)$

$$B = I_\omega^{ps}(\lambda)\,\frac{\rho_c(\lambda)}{\rho_c^s(\lambda)}$$

and

$$C = \tfrac{1}{4}(I_\omega^{bs}(\lambda) + I_\omega^{as}(\lambda))\left(1 + \frac{I_{HB}^p(\lambda)}{I_\omega(\lambda)}\right)\left(\frac{\rho_c(\lambda)}{\rho_c^s(\lambda)} - 1\right)$$

Then

$$\left(\frac{\Delta I_{\omega b}^p(\lambda)}{I_{\omega b}^p(\lambda)}\right)^2 = \frac{\Delta A^2 + \Delta B^2 + \Delta C^2}{(A - B + C)^2} \tag{36}$$

Now

$$A = I_\omega^p(\lambda)$$

so

$$(\Delta A)^2 = (\Delta I_\omega^p(\lambda))^2 \tag{37}$$

$$B = I_{\omega}^{ps}(\lambda) \frac{\rho_c(\lambda)}{\rho_c^s(\lambda)}$$

so

$$(\Delta B)^2 = \left(\frac{\rho_c(\lambda)}{\rho_c^s(\lambda)} \otimes \Delta I_{\omega}^{ps}(\lambda)\right)^2 + \left(\frac{I_{\omega}^{ps}(\lambda)}{\rho_c^s(\lambda)} \Delta\rho_c(\lambda)\right)^2 \qquad (38)$$

$$+ \left(\frac{I_{\omega}^{ps}(\lambda)\ \rho_c(\lambda)}{\rho_c^s(\lambda)^2} \Delta\rho_c^s(\lambda)\right)^2$$

From equation (28)

$$\rho_c(\lambda) = R_c \ln \frac{I_c}{I_c^p(\lambda)}$$

so

$$(\Delta\rho_c(\lambda))^2 = \left(\ln \frac{I_c}{I_c^p(\lambda)} \Delta R_c\right)^2 + \left(R_c \frac{\Delta I_c}{I_c}\right)^2 + \left(R_c \frac{\Delta I_c^p(\lambda)}{I_c^p(\lambda)}\right)^2 \qquad (39)$$

From equation (27)

$$R_c = \frac{\rho_c L}{\sum_{i=1}^{n} \left(\ln \frac{I_c}{I_c^p(\lambda_i)}\right) \Delta\lambda_i}$$

so

$$(\Delta R_c)^2 = \left(\frac{R_c}{\rho_c} \times \Delta\rho_c\right)^2 + \left(\frac{R_c^2}{\rho_c L} \sum_{i=1}^{n} \left(\frac{\Delta\lambda_i}{I_c}\right) \Delta I_c\right)^2 + \qquad (40)$$

$$+ \left(\frac{R_c^2}{\rho_c L} \sum_{i=1}^{n} \left(\frac{\Delta\lambda_i}{I_c^p(\lambda_i)}\right) \Delta I_c^p(\lambda_i)\right)^2$$

Now

$$I_c = \tfrac{1}{2}(I_c^b + I_c^a)$$

so

$$\left(\frac{\Delta I_c}{I_c}\right)^2 = \frac{(\Delta I_c^b)^2 + (\Delta I_c^a)^2}{(I_c^b + I_c^a)^2} \tag{41}$$

From equation (30)

$$\rho_c^s(\lambda) = R_c \ln \frac{I_c}{I_c^{ps}(\lambda)}$$

so

$$(\Delta\rho_c^s(\lambda))^2 = \left(\ln \frac{I_c}{I_c^{ps}(\lambda)} \Delta R_c\right)^2 + \left(R_c \frac{\Delta I_c}{I_c}\right)^2 + \left(R_c \frac{\Delta I_c^{ps}(\lambda)}{I_c^{ps}(\lambda)}\right)^2 \tag{42}$$

$$C = \tfrac{1}{4}(I_\omega^{bs}(\lambda) + I_\omega^{as}(\lambda))\left(1 + \frac{I_{HB}^p(\lambda)}{I_\omega(\lambda)}\right)\left(\frac{\rho_c(\lambda)}{\rho_c^s(\lambda)} - 1\right)$$

so

$$(\Delta C)^2 = \left[\tfrac{1}{4}\left(1 + \frac{I_{HB}^p(\lambda)}{I_\omega(\lambda)}\right)\left(\frac{\rho_c(\lambda)}{\rho_c^s(\lambda)} - 1\right) \Delta I_\omega^{bs}(\lambda)\right]^2 \tag{43}$$

$$+ \left[\tfrac{1}{4}\left(1 + \frac{I_{HB}^p(\lambda)}{I_\omega(\lambda)}\right)\left(\frac{\rho_c(\lambda)}{\rho_c^s(\lambda)} - 1\right) \Delta I_\omega^{as}(\lambda)\right]^2$$

$$+ \left[\tfrac{1}{4}(I_{\omega}^{bs}(\lambda) + I_{\omega}^{as}(\lambda))\left(\frac{\rho_c(\lambda)}{\rho_c^s(\lambda)} - 1\right) \frac{\Delta I_{HB}^{p}(\lambda)}{I_{\omega}}\right]^2$$

$$+ \left[\tfrac{1}{4}(I_{\omega}^{bs}(\lambda) + I_{\omega}^{as}(\lambda))\left(\frac{\rho_c(\lambda)}{\rho_c^s(\lambda)} - 1\right) \frac{I_{HB}^{p}(\lambda)}{I_{\omega}(\lambda)^2} \Delta I_{\omega}\right]^2$$

$$+ \left[\tfrac{1}{4}(I_{\omega}^{bs}(\lambda) + I_{\omega}^{as}(\lambda))\left(1 + \frac{I_{HB}^{p}(\lambda)}{I_{\omega}}\right) \frac{\Delta\rho_c}{\rho_c^s(\lambda)}\right]^2$$

$$+ \left[\tfrac{1}{4}(I_{\omega}^{bs}(\lambda) + I_{\omega}^{as}(\lambda))\left(1 + \frac{I_{HB}^{p}(\lambda)}{I_{\omega}}\right) \frac{\rho_c(\lambda)}{\rho_c^s(\lambda)} \Delta\rho_c^s(\lambda)\right]^2$$

From equation (14)

$$I_{HB}^{p}(\lambda) = I_{H}^{p}(\lambda) - I_{H}^{ps}(\lambda) \frac{\rho_c(\lambda)}{\rho_c^s(\lambda)}$$

so

$$(\Delta I_{HB}^{p}(\lambda))^2 = (\Delta I_{H}^{p}(\lambda))^2 + \left(\frac{\rho_c(\lambda)}{\rho_c^s(\lambda)} \Delta I_{H}^{ps}(\lambda)\right)^2 + \left(\frac{I_{H}^{ps}(\lambda)}{\rho_c^s(\lambda)} \Delta\rho_c(\lambda)\right)^2 \qquad (44)$$

$$+ \left(I_{H}^{ps}(\lambda) \frac{\rho_c(\lambda)}{\rho_c^s(\lambda)^2} \Delta\rho_c^s(\lambda)\right)^2$$

From equation (11)

$$I_{\omega}(\lambda) = \tfrac{1}{2}(I_{\omega}^{b}(\lambda) - I_{\omega}^{bs}(\lambda) + I_{\omega}^{a}(\lambda) - I_{\omega}^{as}(\lambda))$$

so

$$(\Delta I_{\omega}(\lambda))^2 = \tfrac{1}{4}[(\Delta I_{\omega}^{b}(\lambda))^2 + (\Delta I_{\omega}^{bs}(\lambda))^2 + (\Delta I_{\omega}^{a}(\lambda))^2 + (\Delta I_{\omega}^{as}(\lambda))^2] \qquad (45)$$

From equation (31)

$$\rho_H(\lambda) = R_H \ln \frac{I_H}{I_{HB}^{p}(\lambda)}$$

so

$$\left(\frac{\Delta\rho_H(\lambda)}{\rho_H(\lambda)}\right)^2 = \left(\frac{\Delta R_H}{R_H}\right)^2 + \frac{1}{\left(\ln \frac{I_H}{I_{HB}^{p}(\lambda)}\right)^2}\left[\left(\frac{\Delta I_H}{I_H}\right)^2 + \left(\frac{\Delta I_{HB}^{p}(\lambda)}{I_{HB}^{p}(\lambda)}\right)^2\right] \qquad (46)$$

where

$$R_H = \frac{\rho_H L}{\sum_{i=1}^{n} \ln \frac{I_H}{I_{HB}^{p}(\lambda_i)} \Delta\lambda_i}$$

and

$$(\Delta R_H)^2 = \left(\frac{R_H}{\rho_H} \times \Delta\rho_H\right)^2 + \left(\frac{R_H^2}{\rho_H L} \sum_{i=1}^{n} \left(\frac{\Delta\lambda_i}{I_H}\right) \Delta I_H\right)^2 \qquad (47)$$

$$+ \left(\frac{R_H^2}{\rho_H L} \sum_{i=1}^{n} \left(\frac{\Delta\lambda_i}{I_{HB}^{p}(\lambda_i)}\right) \Delta I_{HB}^{p}(\lambda_i)\right)^2$$

From equation (13)

$$I_H = \tfrac{1}{2}(I_H^b - I_H^{bs} + I_H^a - I_H^{as})$$

so

$$\left(\frac{\Delta I_H}{I_H}\right)^2 = \frac{(\Delta I_H^b)^2 + (\Delta I_H^{bs})^2 + (\Delta I_H^a)^2 + (\Delta I_H^{as})^2}{(I_H^b - I_H^{bs} + I_H^a - I_H^{as})^2} \qquad (48)$$

From the initial values of $\frac{\Delta I}{I}$ for all of the signals and the values for the aerosol densities, $\frac{\Delta\rho}{\rho}$, each of the error quantities is evaluated using the above set of equations.

A computer program was written to calculate the mass attenuation coefficient and its associated error. The program is given in Appendix B with a sample output. The percentage error is calculated for each value of the mass attenuation coefficient. It has been estimated that the signals from each of the photomultipliers can be measured within an accuracy of two percent and the aerosol densities can be measured within an accuracy of 10 percent. The path length is the distance between the two tungsten sight tube ends.

The main sources of error in measuring the temperature of a gas by means of a thermocouple inserted in it are the exchange of radiation between the thermocouple and the surrounding walls, the conduction of heat along the thermocouple leads, and the lag between the thermocouple and the gas temperature when the gas temperature fluctuates. By shielding the thermocouples, the error due to radiation between the thermocouple and the surrounding walls is minimized. The thermocouple leads are much longer than the 10 mil wire diameter, so conduction is very small through the

thermocouple wire. Since the thermocouple bead is 15 mils in diameter, the response time of the thermocouple is much smaller than the time it takes to change the temperature significantly. Therefore, the temperature lag between the thermocouple and the gas is negligible. The fast response digital voltmeter can read the temperature to an accuracy of about two degrees Fahrenheit. Therefore, a maximum of two percent error in the temperature measurement is estimated.

CHAPTER VI

THEORETICAL CALCULATIONS

The absorption of electromagnetic radiation by spherical particles can be calculated theoretically using Maxwell's equations.[35] In 1908, Mie[19] published a rigorous solution for the scattering and absorption of electromagnetic radiation by a homogeneous sphere of any composition in a homogeneous, transparent, non-magnetic medium. This is the solution of Maxwell's equations for diffraction of a plane monochromatic wave by such a sphere.

Consider the diffraction of a plane, linearly polarized, monochromatic wave by a sphere of radius a, immersed in a homogeneous, isotropic medium. We assume the medium to be a non-conductor and both medium and sphere non-magnetic.

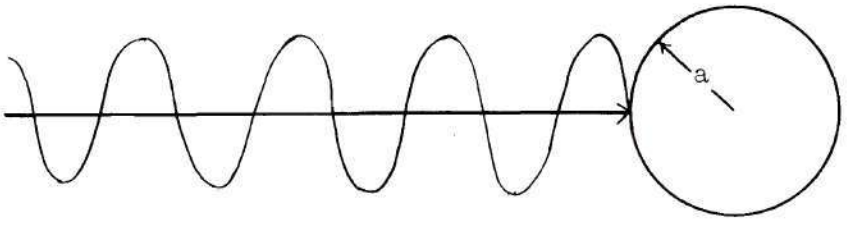

The time-dependent Maxwell's equations with no sources are given by

$$\nabla \times \vec{H}(t) = \frac{4\pi\sigma}{c} \vec{E}(t) + \frac{\epsilon}{c} \frac{\partial \vec{E}(t)}{\partial t} \tag{49}$$

and

$$\nabla \times \vec{E}(t) = - \frac{\mu}{c} \frac{\partial \vec{H}(t)}{\partial t} \tag{50}$$

where $\vec{H}(t)$ = magnetic component of the electromagnetic wave

$\vec{E}(t)$ = electric component of the electromagnetic wave

σ = electrical conductivity

ϵ = inductive capacity

μ = magnetic permeability

c = velocity of light

These equations are applicable both inside and outside the sphere. The solution of these equations should satisfy the boundary conditions that the radial and tangential components of magnetic and electric fields be continuous at the surface of the sphere at r = a. In practice, one is usually concerned with scattering of unpolarized light. In such cases, the solutions are modified by averaging over all directions of polarization.

Maxwell's equations together with the boundary conditions then separate into a set of ordinary differential equations which are solved to give the Mie equations. Since excellent treatment of the Mie solution is available in the literature,[36,37] a complete derivation is not given here. The basic Mie equations for the extinction and scattering cross sections are given by

$$\sigma_e = \frac{2\pi a^2}{q^2} \sum_{n=1}^{\infty} (2n + 1) \, R_e \, (a_n + b_n) \tag{51}$$

$$\sigma_s = \frac{2\pi a^2}{q^2} \sum_{n=1}^{\infty} (2n + 1) \, (|a_n|^2 + |b_n|^2) \tag{52}$$

The symbol "R_e" denotes the real part of a complex number and

a = particle radius

q = size parameter = $\frac{2\pi a}{\lambda}$

λ = wavelength of radiation

a_n and b_n are the Mie coefficients given by

$$a_n = - \frac{J_n(Nq)\,[qJ_n(q)]' - J_n(q)\,[Nq\,J_n(Nq)]'}{J_n(Nq)\,[q\,H_n^{(2)}(q)]' - H_n^{(2)}(q)\,[Nq\,J_n(Nq)]'} \tag{53}$$

$$b_n = - \frac{J_n(q)\,[Nq\,J_n(Nq)]' - N^2\,J_n(Nq)\,[q\,J_n(q)]'}{H_n^{(2)}\,[Nq\,J_n(Nq)]' - N^2\,J_n(Nq)\,[q\,H_n^{(2)}(q)]'} \tag{54}$$

where primes denote differentiation and

$J_r(\ )$ = spherical Bessel function

$H_r^{(2)}(\ )$ = spherical Hankel function of the second kind

$N = \frac{\text{refractive index of particle}}{\text{refractive index of medium}}$

The absorption cross section is

$$\sigma_a = \sigma_e - \sigma_s \tag{55}$$

The above set of equations represent a summary of Mie's formal solution. It is difficult to calculate the absorption cross section using these equations. The complications arise due to the relative refractive index N being a complex quantity and extensive tables of spherical Bessel functions with complex arguments are not available. An excellent transformation procedure, facilitating computation, is given by Aden[38] which makes possible the calculation of absorption and scattering coefficients.

Krascella[20] has used this transformation of the Mie equations to develop a computer program which calculates σ_a, σ_e, and σ_s in cm^2/particle as a function of material, wavelength of radiation, and particle radius.

This program was obtained from United Aircraft Corporation[20] and the necessary changes made to run it on the UNIVAC 1108 at Georgia Tech. Reference 20 describes this program. The mass density of the particle material is also provided as part of the program to allow the determination of the mass absorption coefficient

$$\mu_a = \frac{\sigma_a}{\rho V} \tag{56}$$

where ρ is the mass density of the particle material and

V is the volume of the spherical particle of radius a

The main inputs to this program are the radius of the particle, wavelength of radiation, temperature, density of particle material, and the real and imaginary part of the refractive index of the particle material at that temperature and radiation wavelength. The refractive index of the gaseous medium is assumed to be unity and, for our experimental conditions, this assumption is valid.

The calculation of the absorption coefficient is limited by the availability of refractive index data[39,40] of different particle materials at different temperatures and radiation wavelengths. For the cases where refractive index data are available, the absorption coefficient is calculated by Krascella[20] for various materials at a number of particle radii and radiation wavelengths.

To compare the experimental data with theory, the absorption coeffi-

cient for seed materials used in the experiment is calculated for particle sizes from 0.01 micron to 1.0 micron and radiation wavelengths from 1000 Å to 6000 Å. At lower wavelengths where refractive index data are not available, the extrapolated values have been used. The absorption coefficient has been calculated for carbon at 3590°F, silicon at 80°F, and tungsten at 76°F, 1520°F, and 2420°F.

Since Mie's solution is an infinite series, it is rather difficult to illustrate the effect of each variable. However, one may change each variable and study the effect of that variable on the absorption coefficient.

In Figure 16 the absorption coefficient of spherical particles of carbon at 3590°F is given as a function of radiation wavelength. At lower wavelengths, the absorption coefficient increases with wavelength and for wavelengths above 2800 Å the absorption coefficient is essentially independent of wavelength. Also, one can see that the absorption coefficient increases as the particle size decreases. This effect is more readily seen from Figure 17. In Figure 17, the absorption coefficient of carbon at 3590°F is plotted as a function of particle radius for radiation wavelengths of 2000 Å, 4000 Å, and 6000 Å. As the particle size decreases, the absorption coefficient increases to a maximum value and then decreases with particle size.

In Figures 18, 19, and 20, the absorption coefficient of spherical particles of tungsten is plotted as a function of radiation wavelength at temperatures of 76°F, 1520°F, and 2420°F. As can be seen from equations (51) and (52), the absorption coefficient is not directly a function of temperature. The absorption coefficient changes with temperature due to

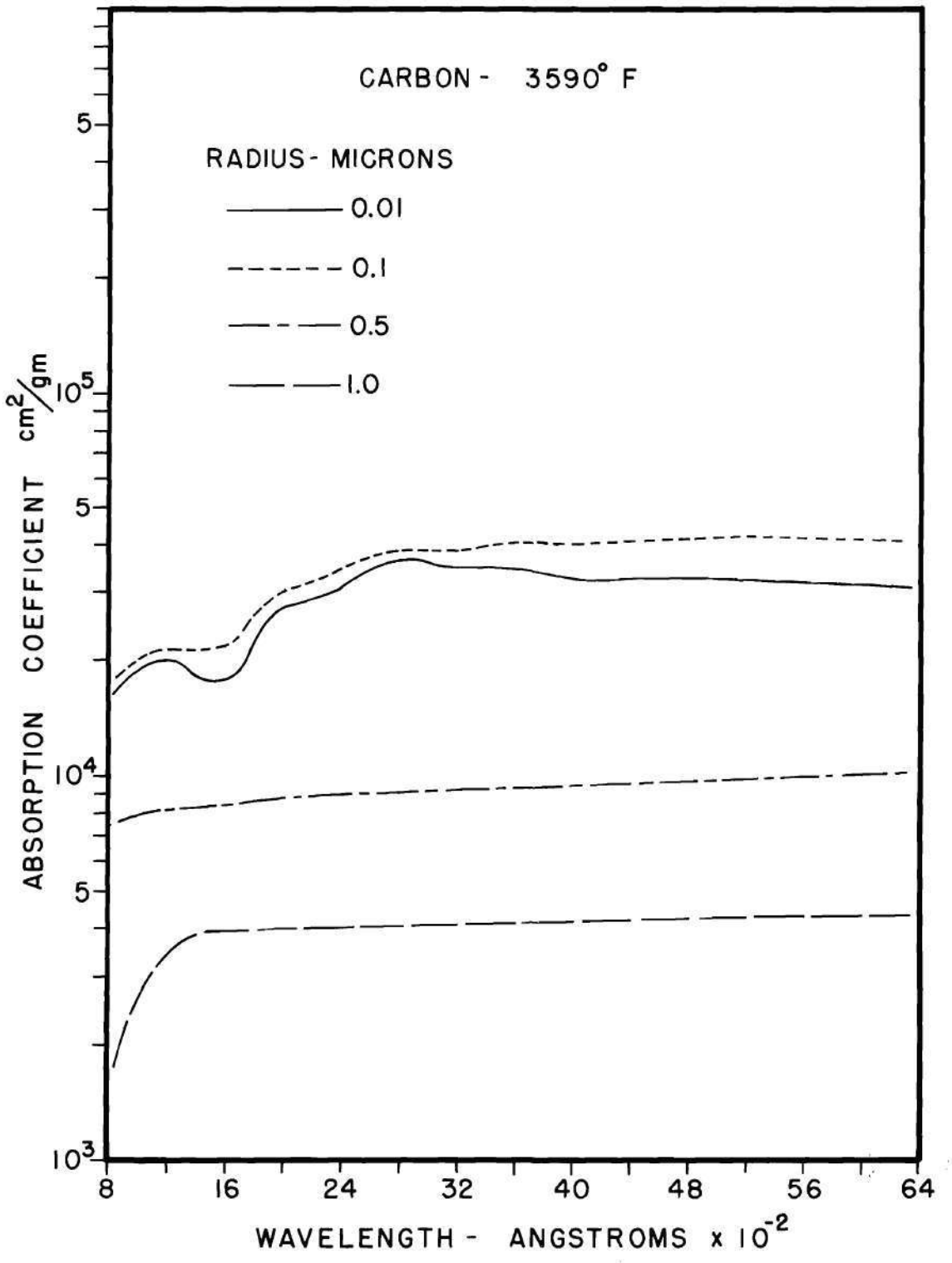

Figure 16. Theoretical Absorption Coefficient of Carbon as a Function of Radiation Wavelength

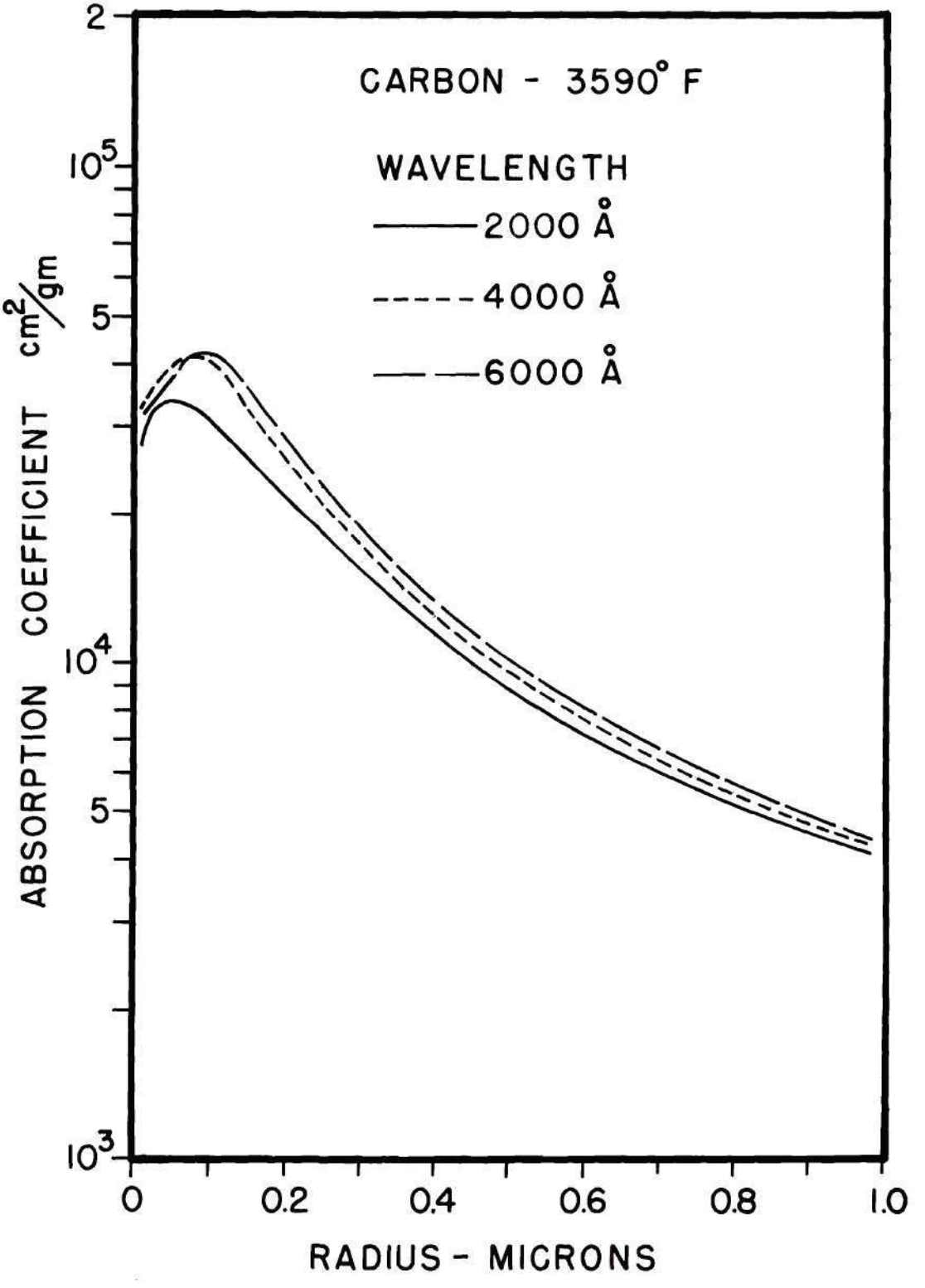

Figure 17. Theoretical Absorption Coefficient of Carbon as a Function of Particle Radius

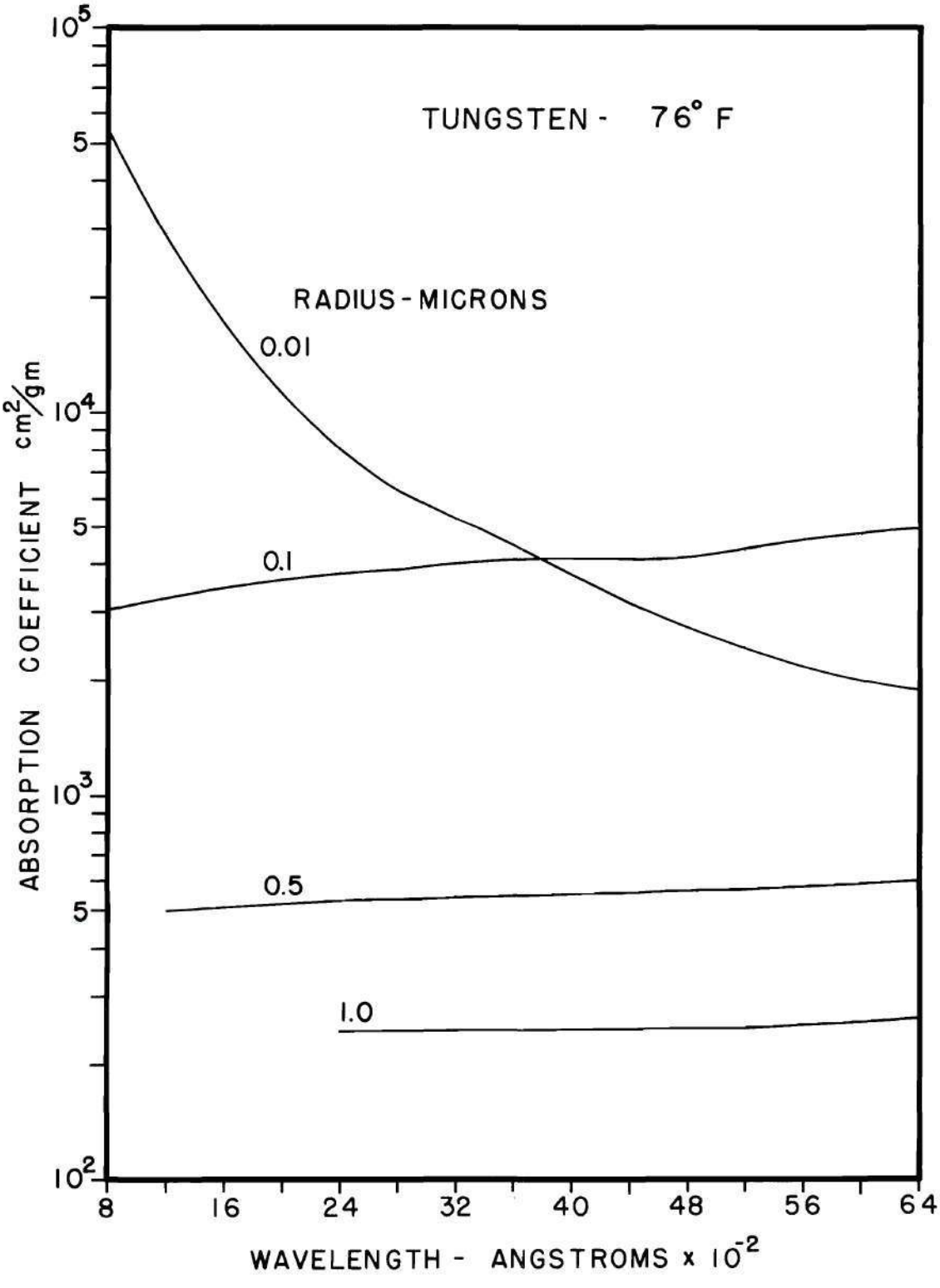

Figure 18. Theoretical Absorption Coefficient of Tungsten at 76°F as a Function of Radiation Wavelength

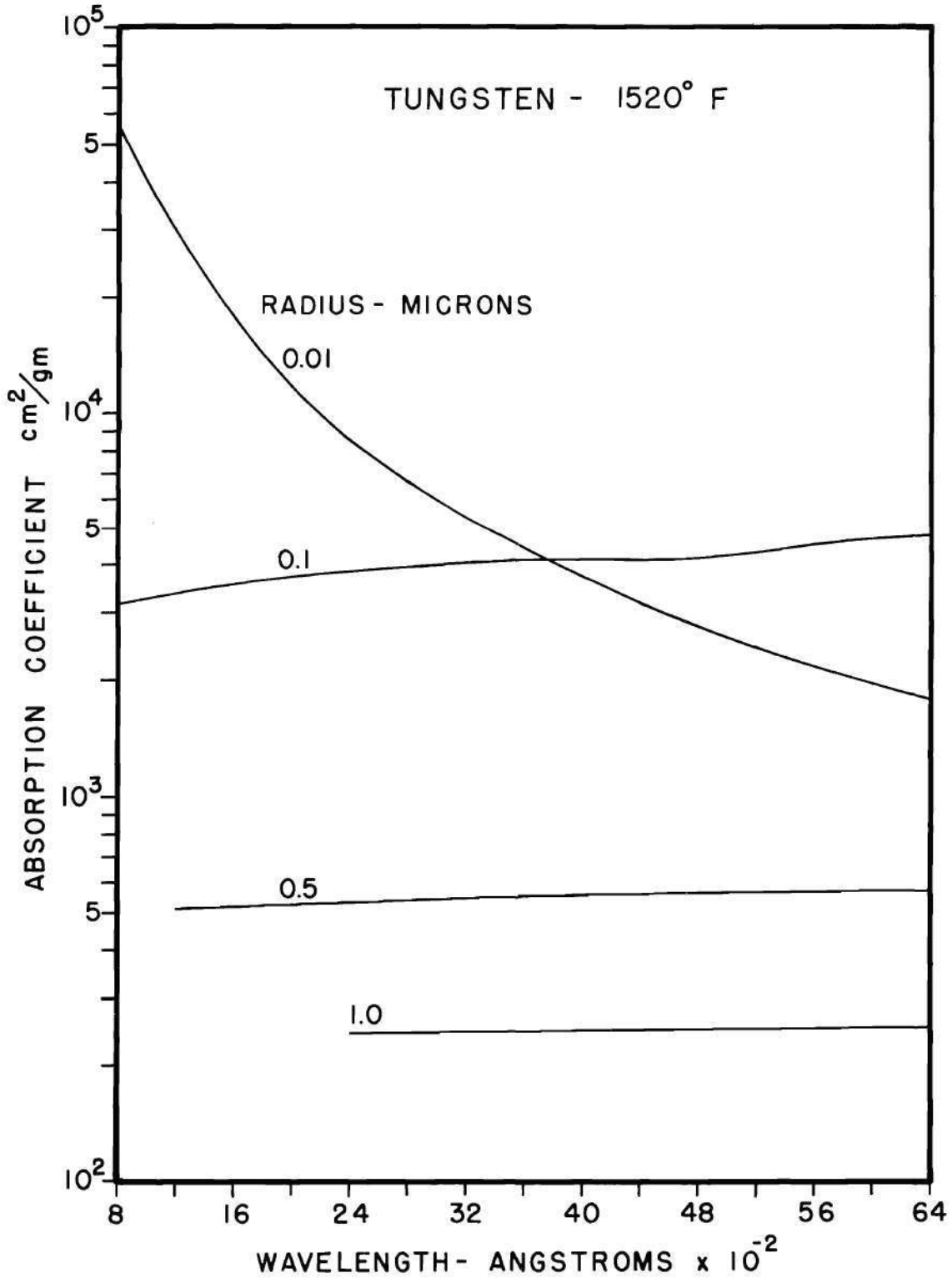

Figure 19. Theoretical Absorption Coefficient of Tungsten at 1520°F as a Function of Radiation Wavelength

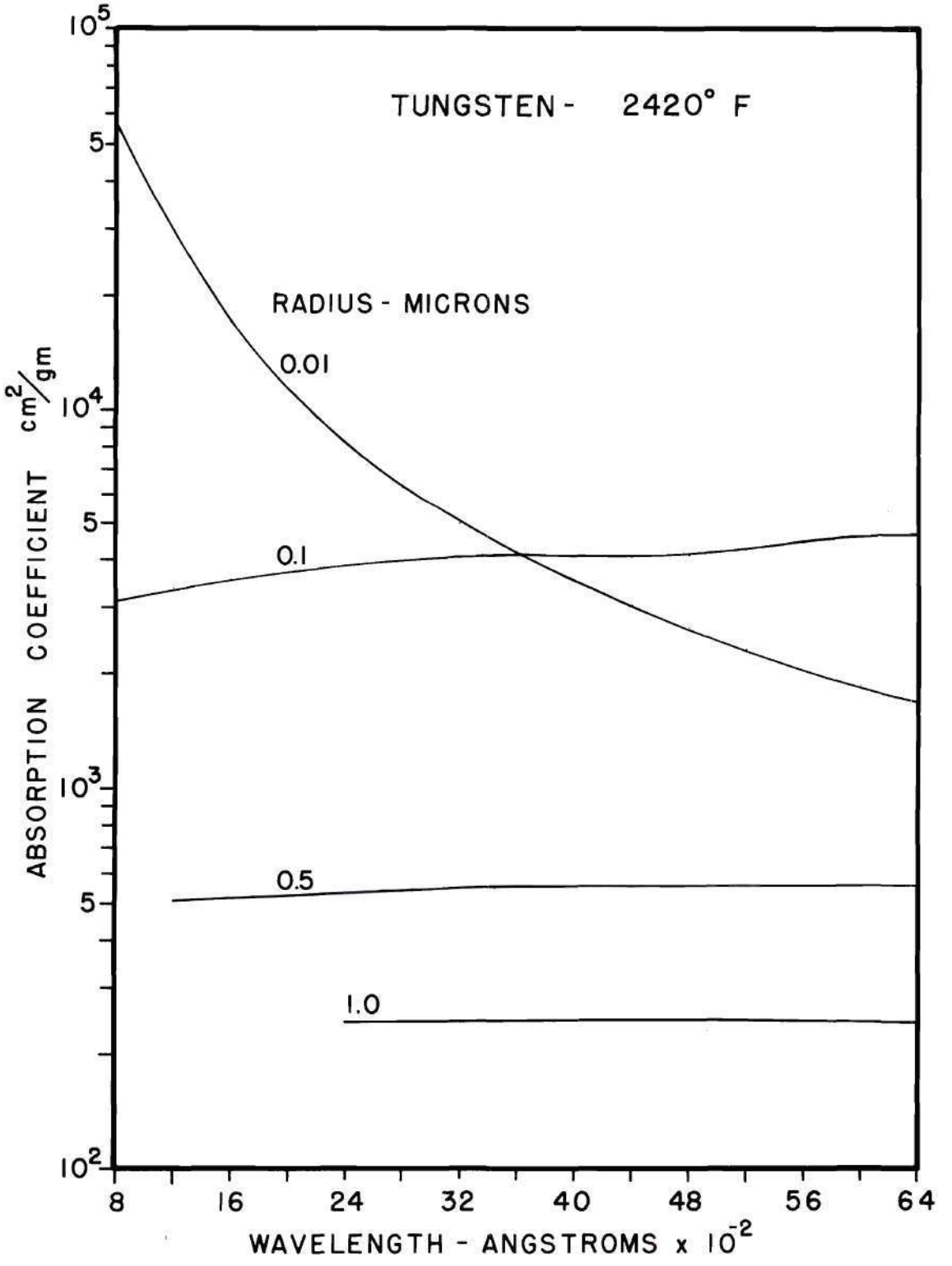

Figure 20. Theoretical Absorption Coefficient of Tungsten at 2420°F as a Function of Radiation Wavelength

the changes in the properties of the seed material, such as the electrical conductivity, inductive capacity, and magnetic permeability. The absorption coefficient for spherical particles of tungsten does not change significantly with temperature. At all three temperatures for very small particle diameters, the absorption coefficient decreases with radiation wavelength. But for particle diameters above 0.2 micron, the absorption coefficient is almost independent of radiation wavelength. As in the case of carbon, the absorption coefficient for tungsten particles decreases as the particle size decreases. This effect is seen more clearly in Figures 21, 22, and 23. At all three temperatures, it can be seen that the absorption coefficient increases as the particle size decreases until a maximum value is reached and then decreases with particle size. Also, it can be seen that the value of the particle size at which the absorption is a maximum increases with radiation wavelength. Since the variation of the absorption coefficient with temperature is small, it is rather difficult to study the effect of temperature from Figures 18 through 23. In Table 1, the absorption coefficient of 0.2 micron radius tungsten particles is given at various temperatures and radiation wavelengths. From this table it can be seen that the temperature dependence is very small.

Figure 24 illustrates the absorption coefficient of spherical particles of silicon at 80°F as a function of particle size for radiation wavelengths of 1200 Å and 2000 Å. Unlike carbon and tungsten, the absorption coefficient reaches a very high value for very small particle sizes.

In Figure 25, the absorption coefficients of spherical particles of three different materials are given for a radiation wavelength of 2000 Å as a function of particle radius. For particle radii greater than

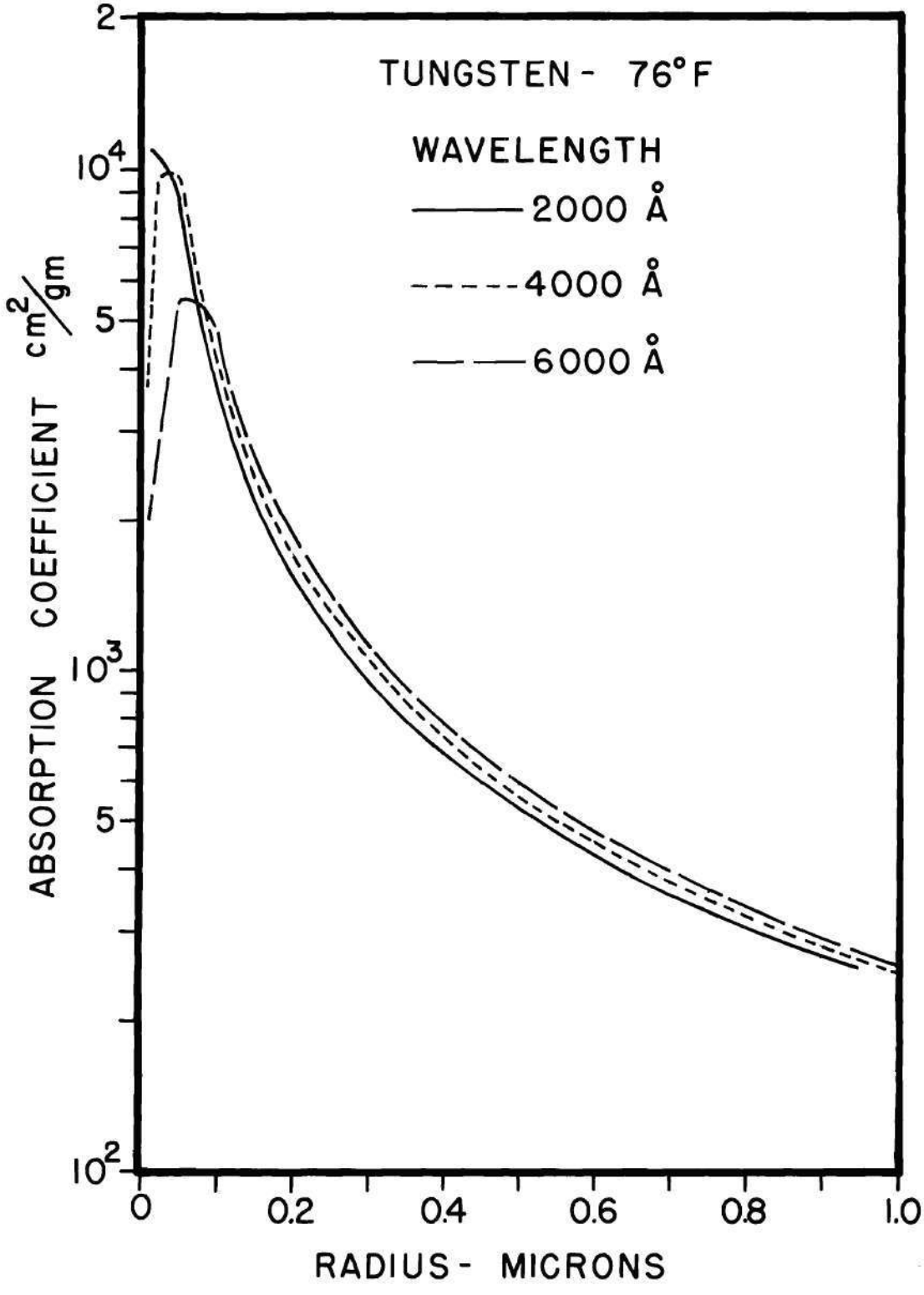

Figure 21. Theoretical Absorption Coefficient of Tungsten at 76°F as a Function of Particle Radius

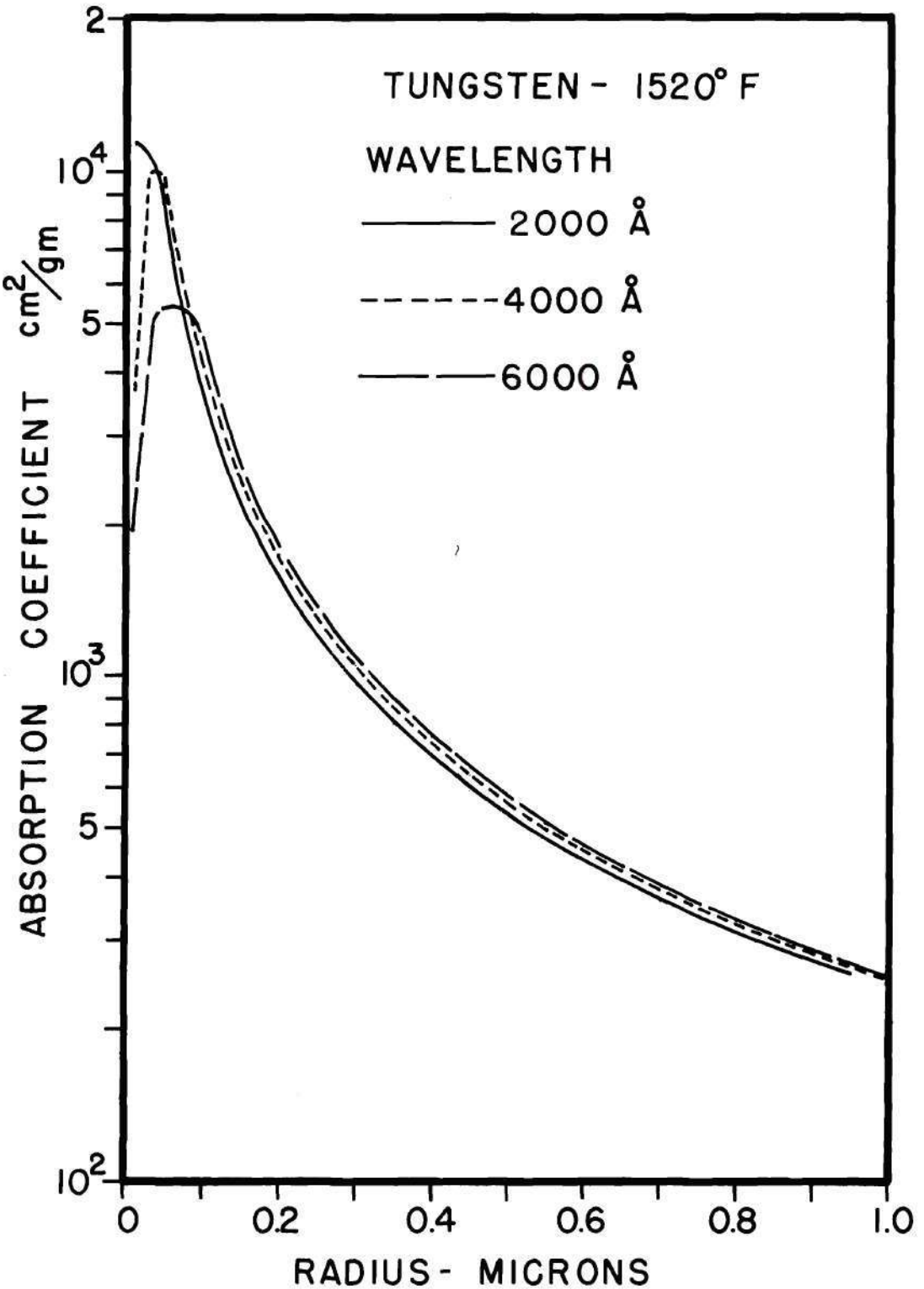

Figure 22. Theoretical Absorption Coefficient of Tungsten at 1520° F as a Function of Particle Radius

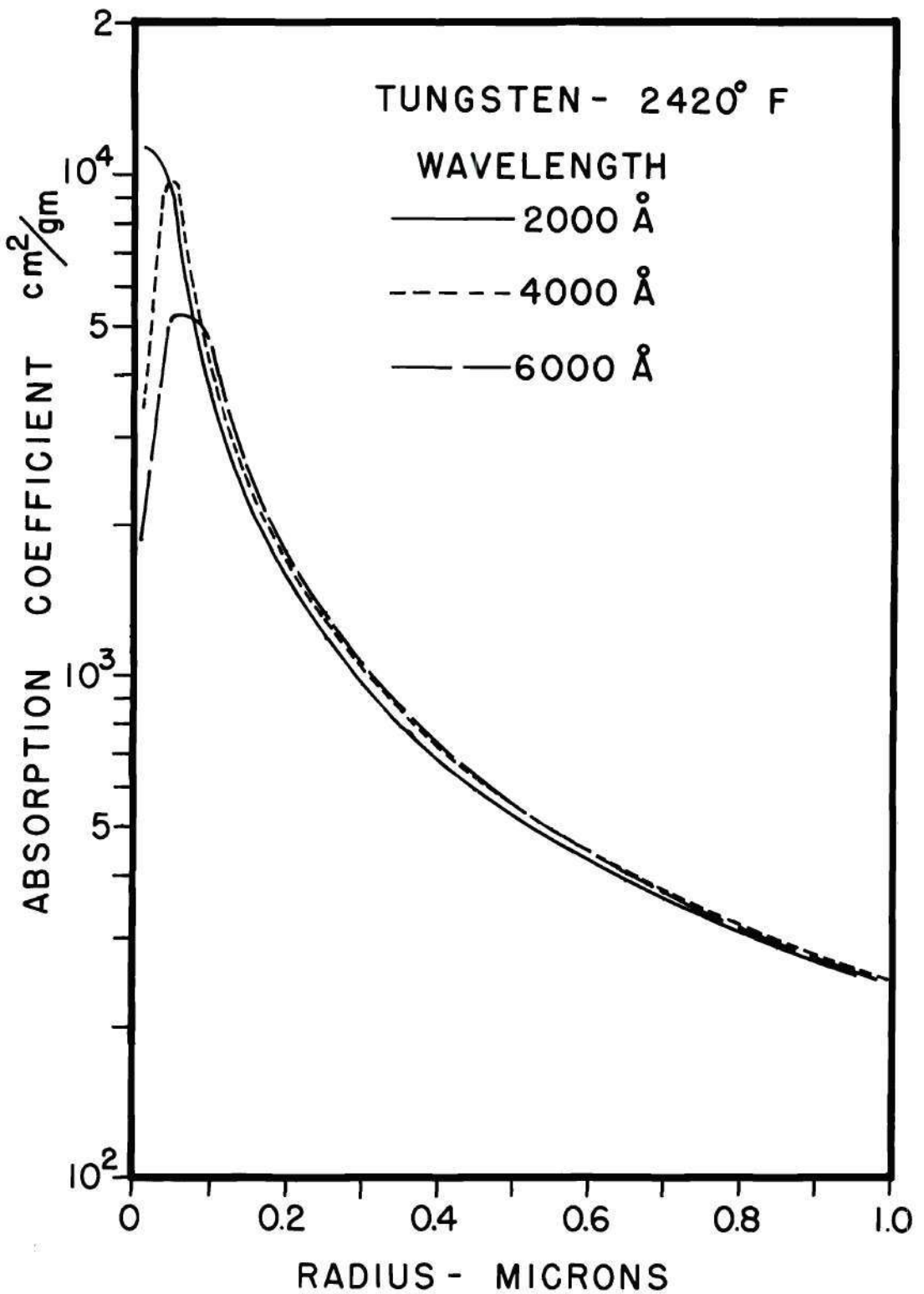

Figure 23. Theoretical Absorption Coefficient of Tungsten at 2420°F as a Function of Particle Radius

Table 1. Theoretical Absorption Coefficient of 0.2 Micron Radius Tungsten Particle at Various Wavelengths and Temperatures

Wavelength	Absorption Coefficient cm^2/gm		
(Å)	2420° F ($\times 10^4$)	1520° F ($\times 10^4$)	76° F ($\times 10^4$)
800	0.1377	0.1387	0.1365
1200	0.1456	0.1468	0.1442
1600	0.1505	0.1518	0.1493
2000	0.1544	0.1558	0.1534
2400	0.1587	0.1601	0.1583
2800	0.1613	0.1630	0.1618
3200	0.1642	0.1659	0.1655
3600	0.1676	0.1693	0.1694
4000	0.1692	0.1707	0.1707
4400	0.1733	0.1748	0.1743
4800	0.1738	0.1768	0.1762
5200	0.1719	0.1749	0.1760
5600	0.1743	0.1785	0.1815
6000	0.1755	0.1808	0.1859
6400	0.1795	0.1866	0.1939

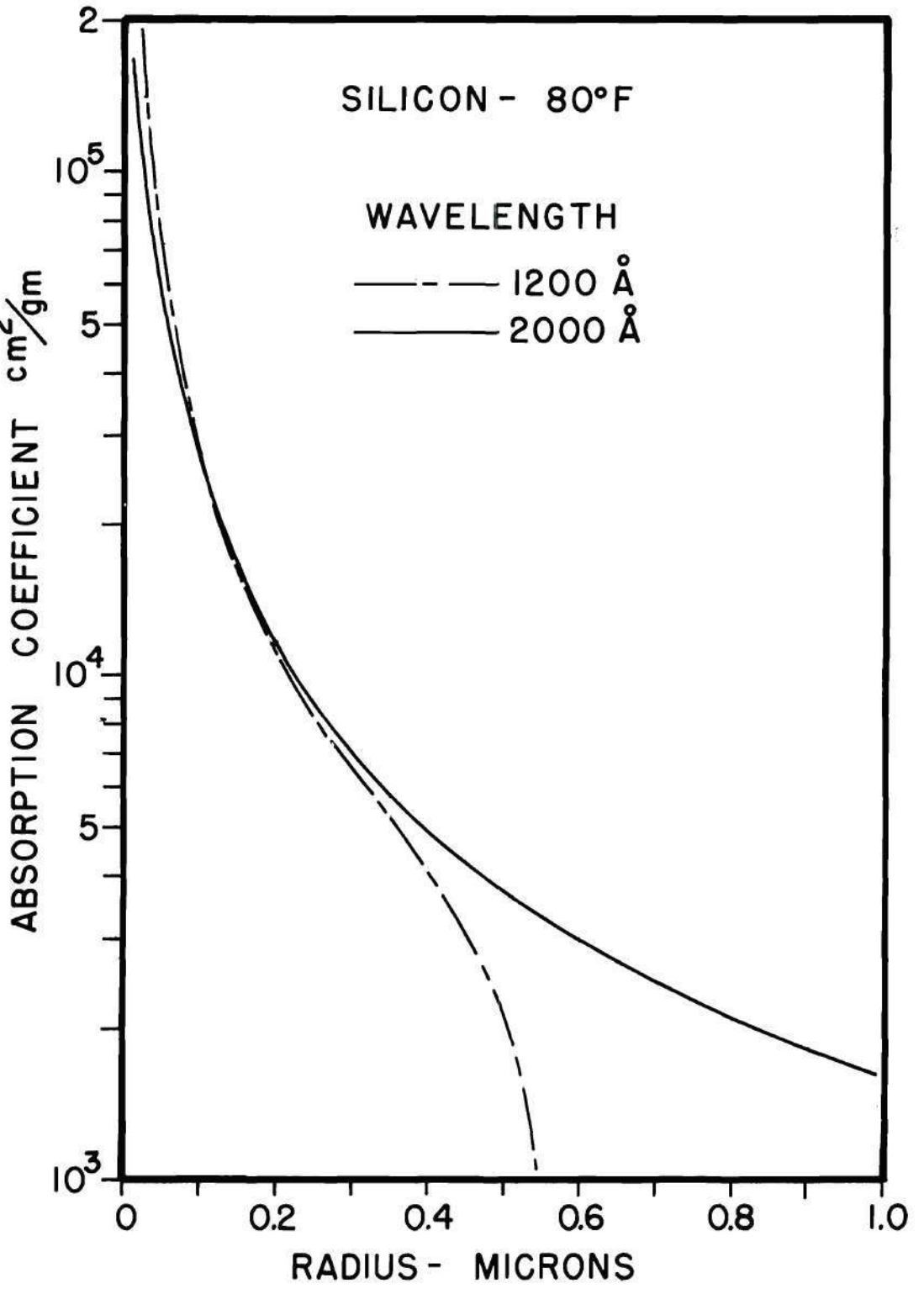

Figure 24. Theoretical Absorption Coefficient of Silicon as a Function of Particle Radius

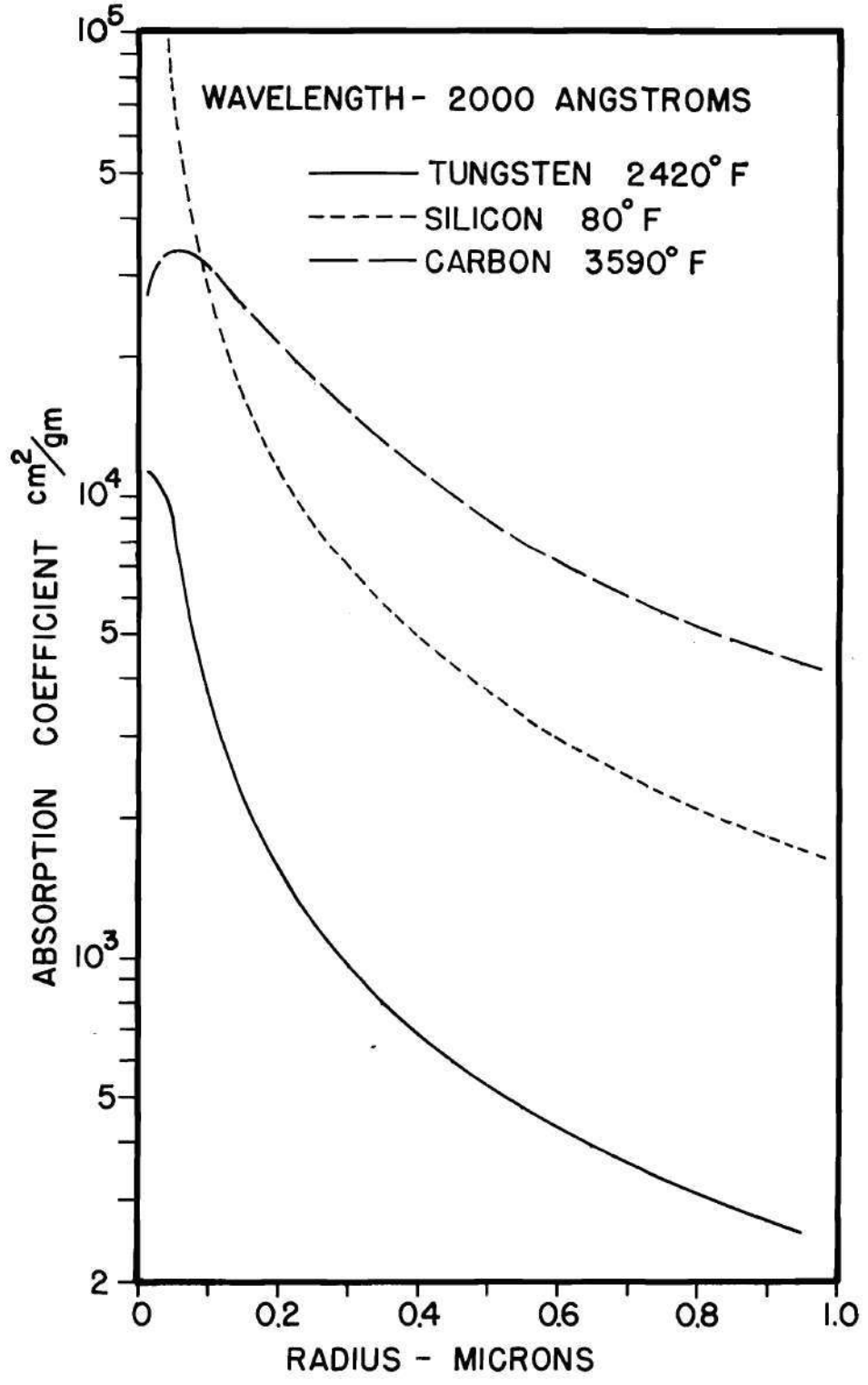

Figure 25. Theoretical Absorption Coefficient of Tungsten, Silicon, and Carbon as a Function of Particle Radius

0.1 micron carbon has the highest absorption coefficient, tungsten the smallest, and the absorption coefficient of silicon lies between the two. For particle radii smaller than 0.1 micron, silicon has the highest absorption coefficient compared to carbon and tungsten.

CHAPTER VII

EXPERIMENTAL RESULTS

The principal properties to be considered in selecting a seed material are high absorption coefficient per unit mass, high melting and boiling point temperatures, low neutron absorption cross section, and low reactivity with hydrogen. To obtain a higher mass attenuation coefficient a seed material of submicron-size particles is used. For the various submicron-sized powders, even of the same material produced by different processes, the properties such as particle size, shape, color, density, and composition vary from one type of powder to another. Since the mass attenuation coefficient of any particle seed depends on these factors, it is important to specify the properties of a particular seed material used. Many types of submicron-sized carbon powder are manufactured by converting hydrocarbons to elemental carbon and hydrogen. But the properties of these powders depend on the type of process used in converting hydrocarbons to carbon. The properties of various seed materials used in seeding the hydrogen in the experiment are given in Appendix C.

In general, aerosols of submicron-sized particles can be produced by a number of methods. Since smaller particles tend to have a higher mass attenuation coefficient, the aerosol produced should be well dispersed. The mixture of hydrogen and particles from the aerosol generator is expanded through a nozzle as shown in Figure 7 to allow the shear forces to further deagglomerate the particles. The degree of deagglomeration of

the particles can be studied by making electron micrographs. A number of electron micrographs of various seed materials were taken and are shown in Appendix D. From these electron micrographs it can be seen that each of the carbon particles was fairly spherical. The particles that are produced by blowing gas over the powder in a test tube are generally fairly large agglomerants. The electron micrographs show that aerosols produced by the aerosol generator and passed through the nozzle consist of highly dispersed particles. In the case of tungsten particles, the shape of the individual particle was much more irregular than carbon. It is rather difficult to define the size of such irregularly shaped particles. The electron micrographs illustrate the size and size distribution of the particles used in the experiment.

The mass attenuation coefficient of carbon aerosols has been measured for carbon of two varieties at temperatures up to 3450°F. The mass attenuation coefficient was also measured for a tungsten-hydrogen aerosol of two sizes at temperatures up to 3000°F and a silicon-hydrogen aerosol at room temperature.

Carbon-Hydrogen Aerosols

Carbon was first used as a seed material due to its high absorption coefficient, high sublimation temperature, and low neutron absorption cross section. The mass absorption coefficient is measured for Cabot Corporation Spheron 6 and Carbolac 2 carbon black. The results are tabulated in Appendix E. The mass absorption coefficient of carbon (Spheron 6) is presented as a function of radiation wavelength in Figure 26 at a temperature of 80°F. The absorption coefficient of spherical carbon particles

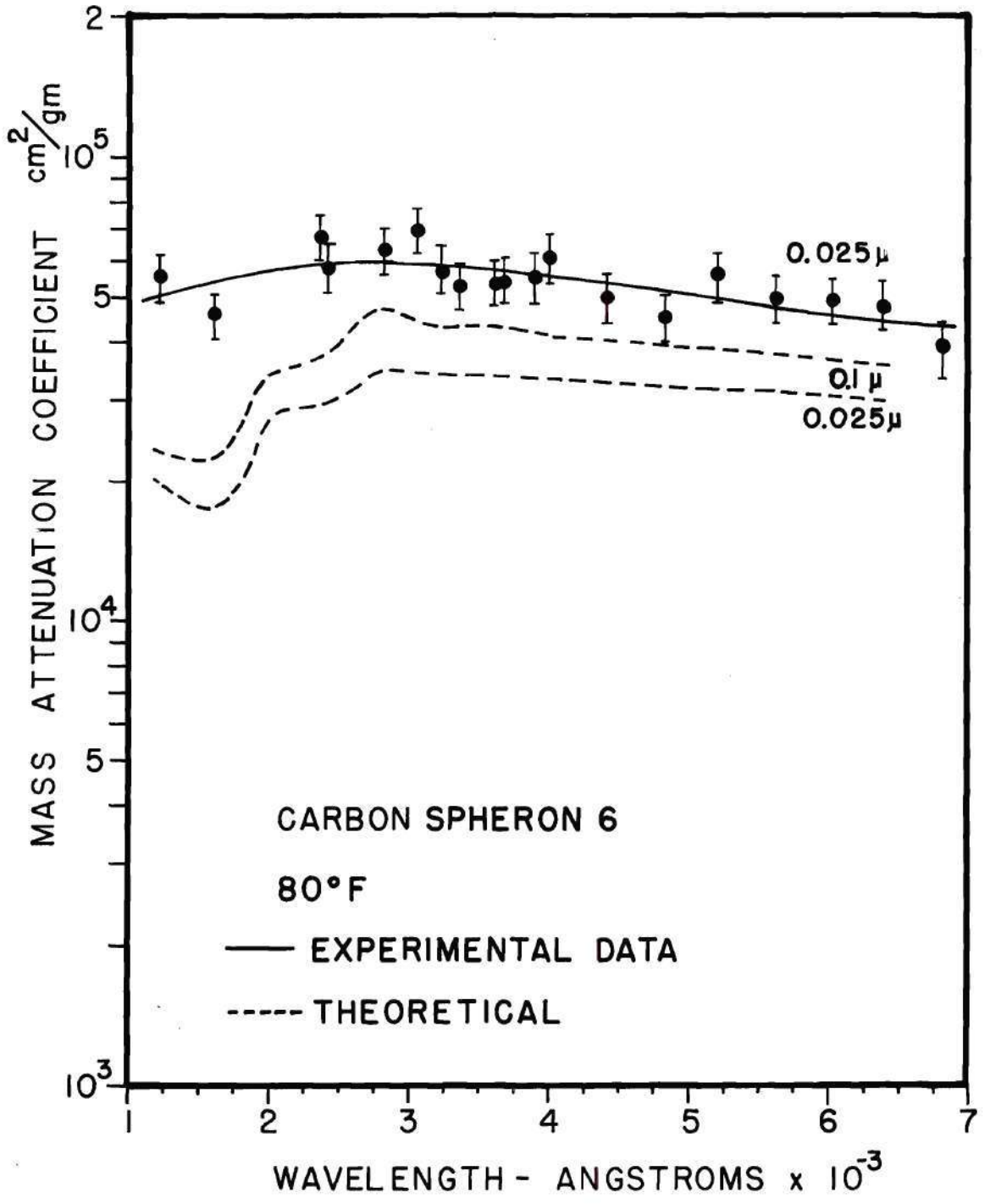

Figure 26. Attenuation Coefficient of Carbon-Hydrogen Aerosol at 80°F

of 0.025 and 0.10 micron diameters was calculated using the Mie theory and is also plotted in Figure 26. In general, a number of different types of curves such as straight line, exponential, or polynomial functions can be drawn through the experimental points. The Mie theory predicts that the absorption coefficient is represented by neither a straight line nor an exponential relation. A third degree polynomial compares well with the Mie theory results as shown in Figure 26. So a least squares third order polynomial was fitted to the experimental data and is shown in the graphs. In Figures 27 through 29, the mass attenuation coefficient is given at temperatures of 1130°F, 1480°F, and 1560°F. The mass absorption coefficient of carbon (Carbolac 2) is presented in Figures 30 through 32 as a function of radiation wavelength at temperatures of 2560°F, 2620°F, and 3450°F. In all of these cases, a third degree polynomial curve is fitted by the method of least squares through the experimental points using a computer program on the PDP-8 computer. The results indicated the mass absorption coefficient of the carbon-hydrogen aerosol to be essentially independent of wavelength over the range of wavelengths and temperatures investigated.

The results also indicate that Carbolac 2 has a slightly higher value of mass absorption coefficient compared with Spheron 6. This is essentially because of the smaller particle size of Carbolac 2 compared to Spheron 6. There is a slight tendency to decrease in mass absorption coefficient with increasing temperature. This may be a result of the disappearance of smaller particles due to the chemical reaction of the aerosol at higher temperatures.

It was found that the density of the aerosol entering the furnace

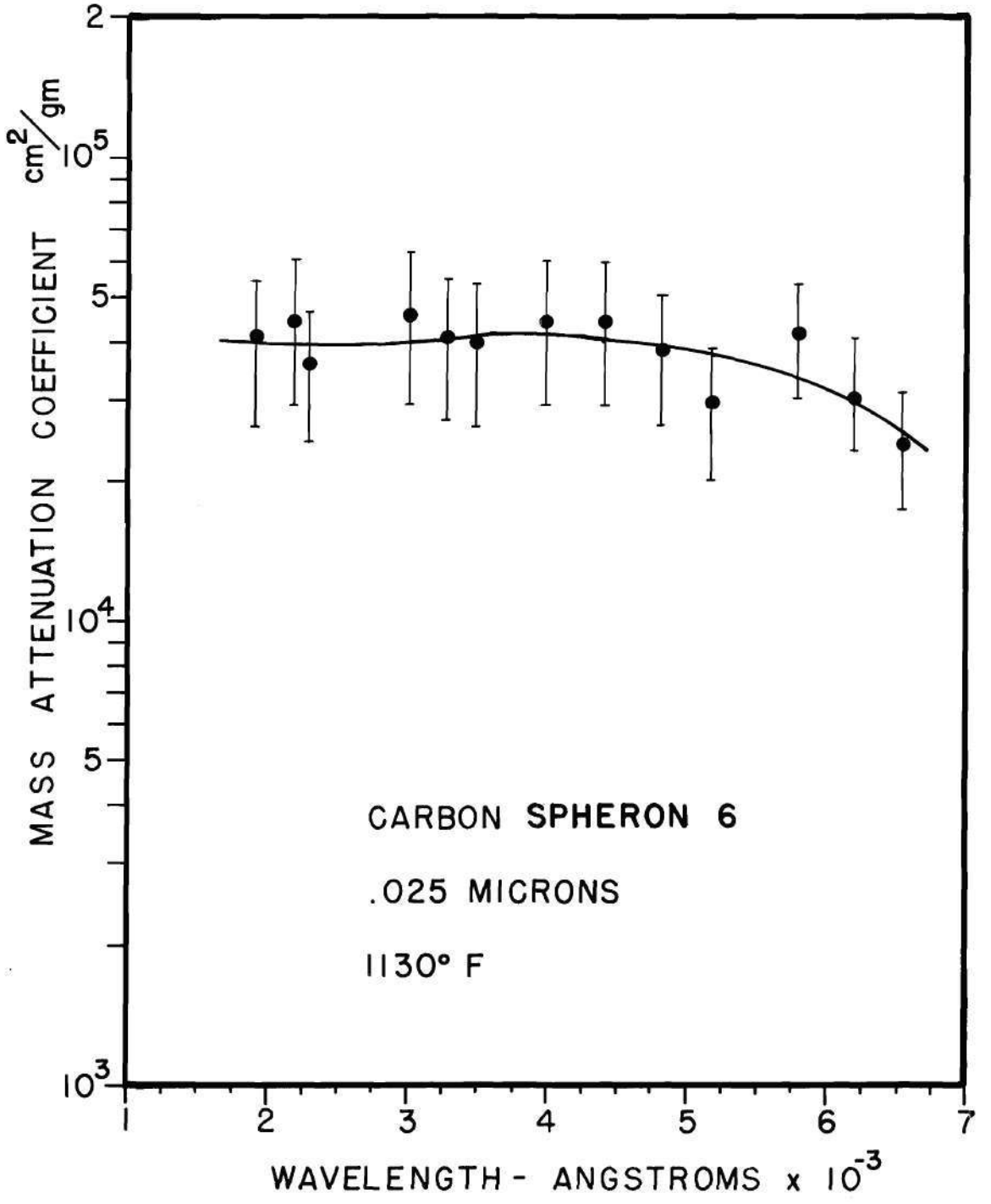

Figure 27. Attenuation Coefficient of Carbon-Hydrogen Aerosol at 1130° F

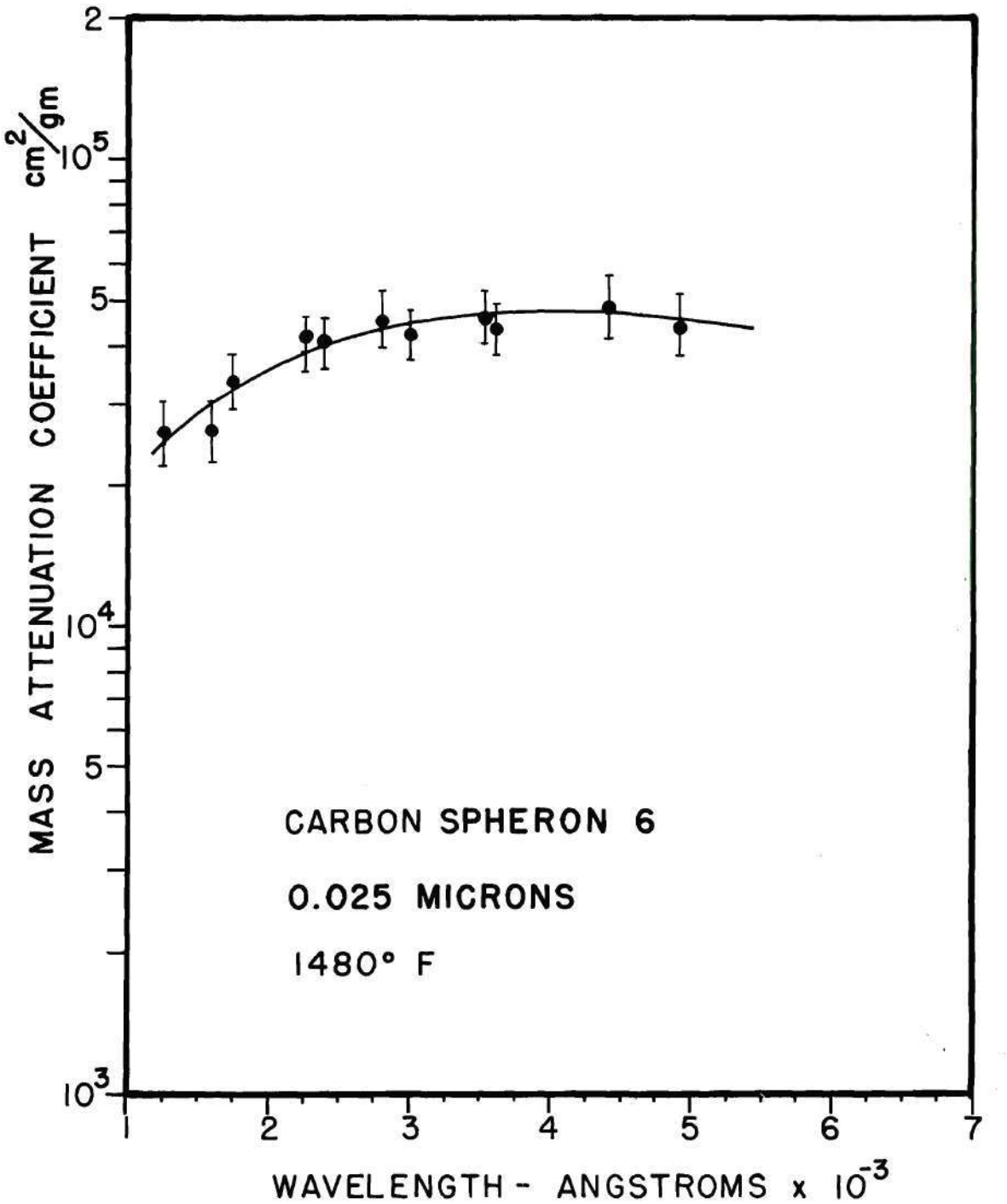

Figure 28. Attenuation Coefficient of Carbon-Hydrogen Aerosol at 1480°F

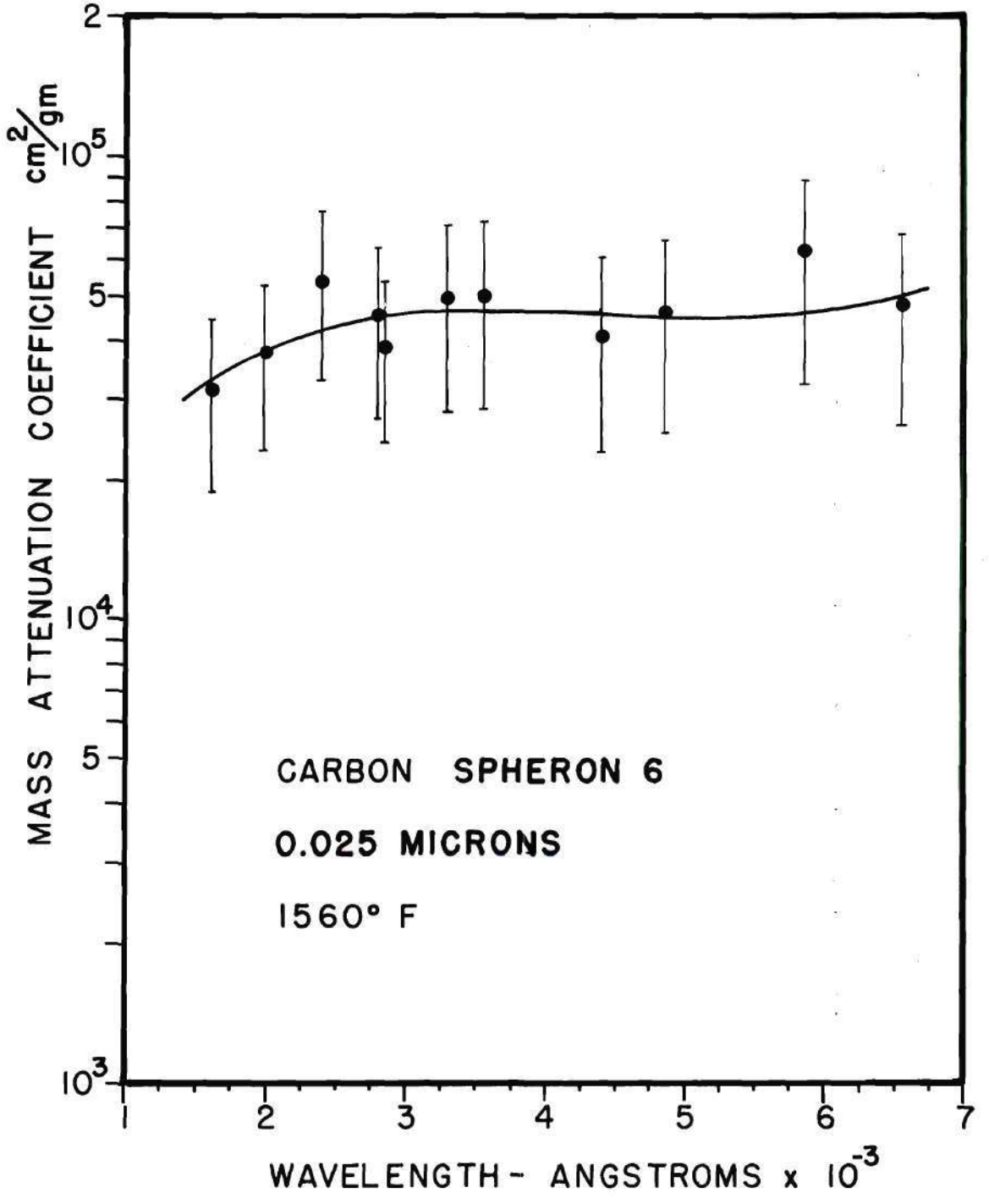

Figure 29. Attenuation Coefficient of Carbon-Hydrogen Aerosol at 1560°F

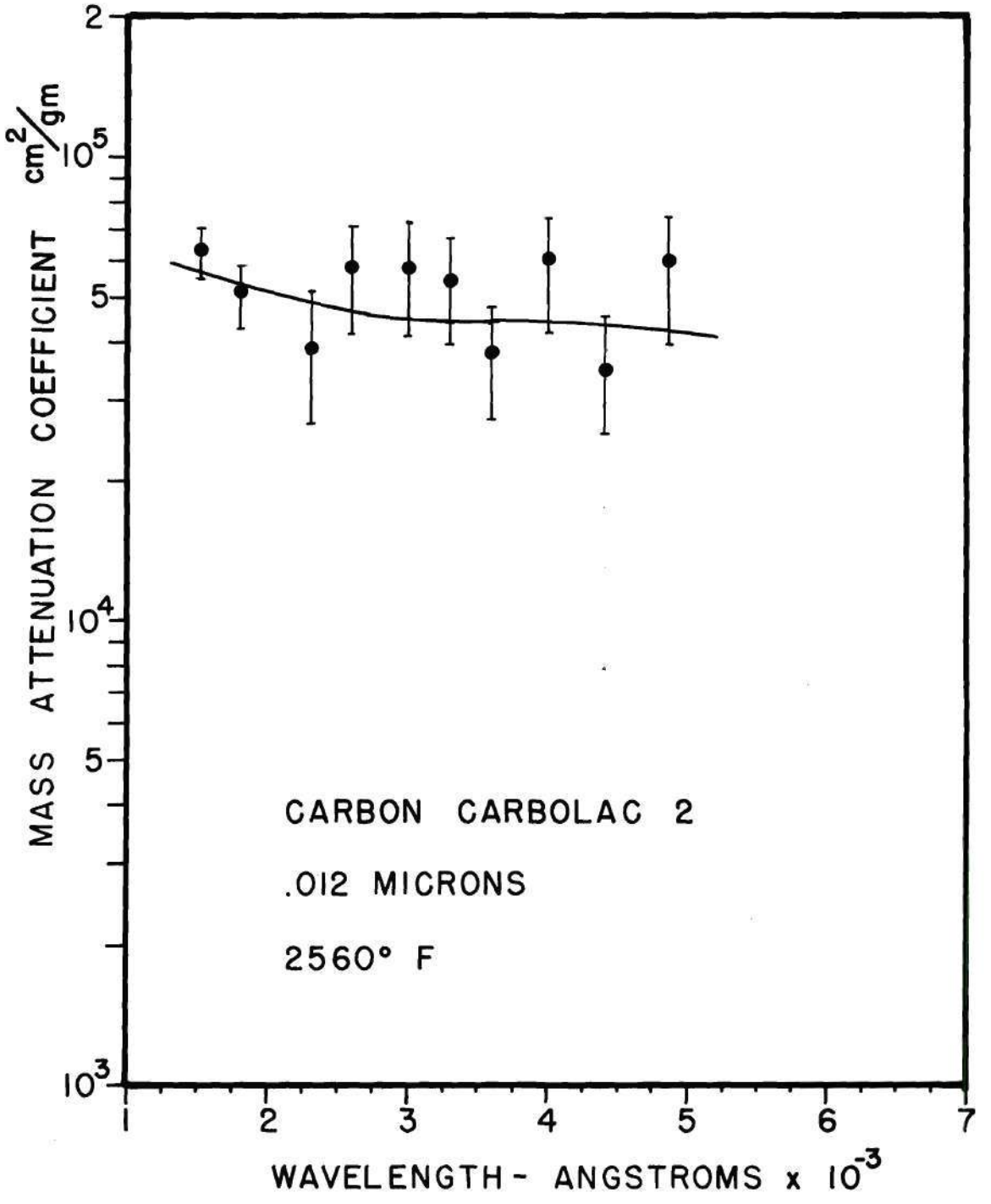

Figure 30. Attenuation Coefficient of Carbon-Hydrogen Aerosol at 2560°F

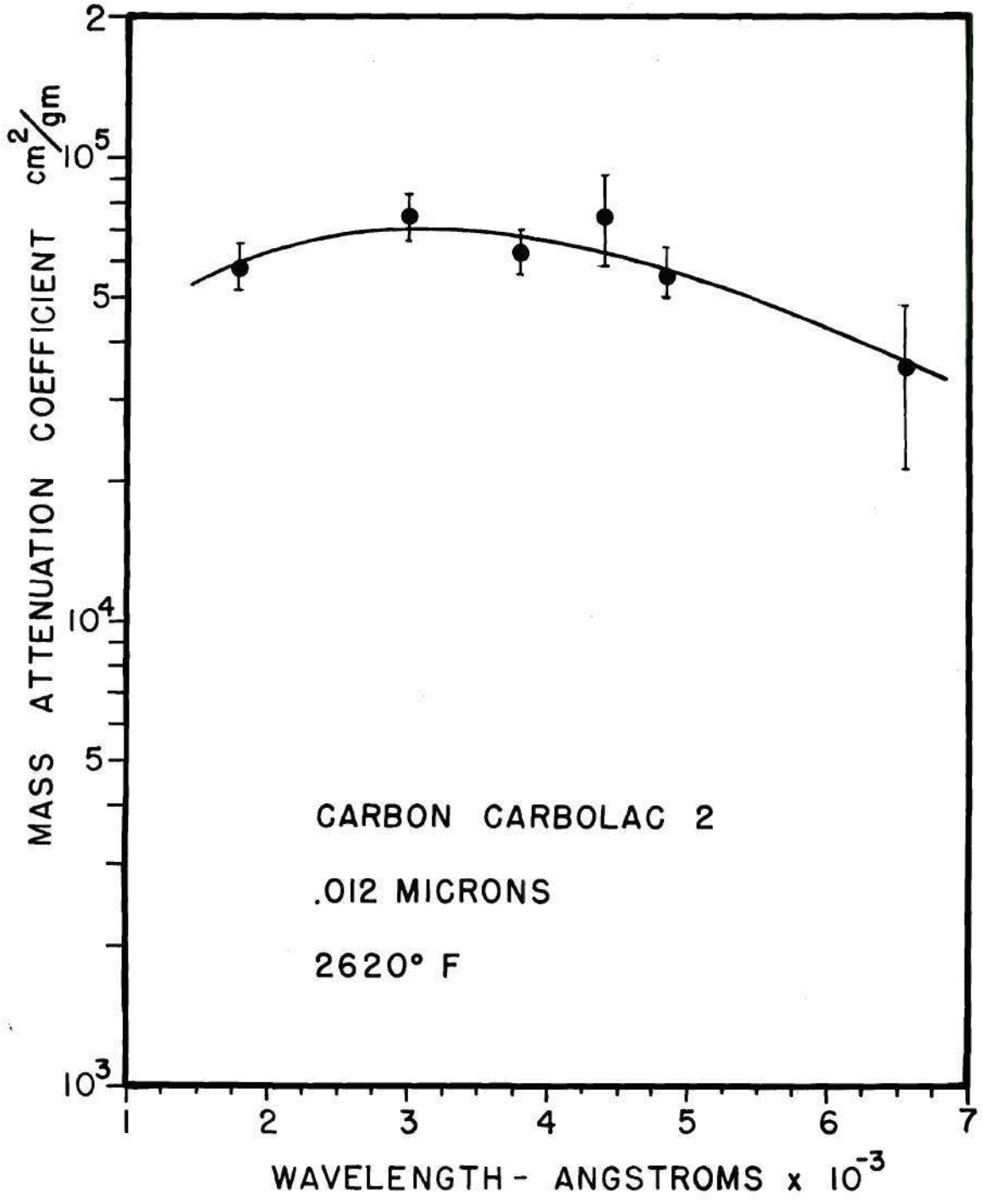

Figure 31. Attenuation Coefficient of Carbon-Hydrogen Aerosol at 2620°F

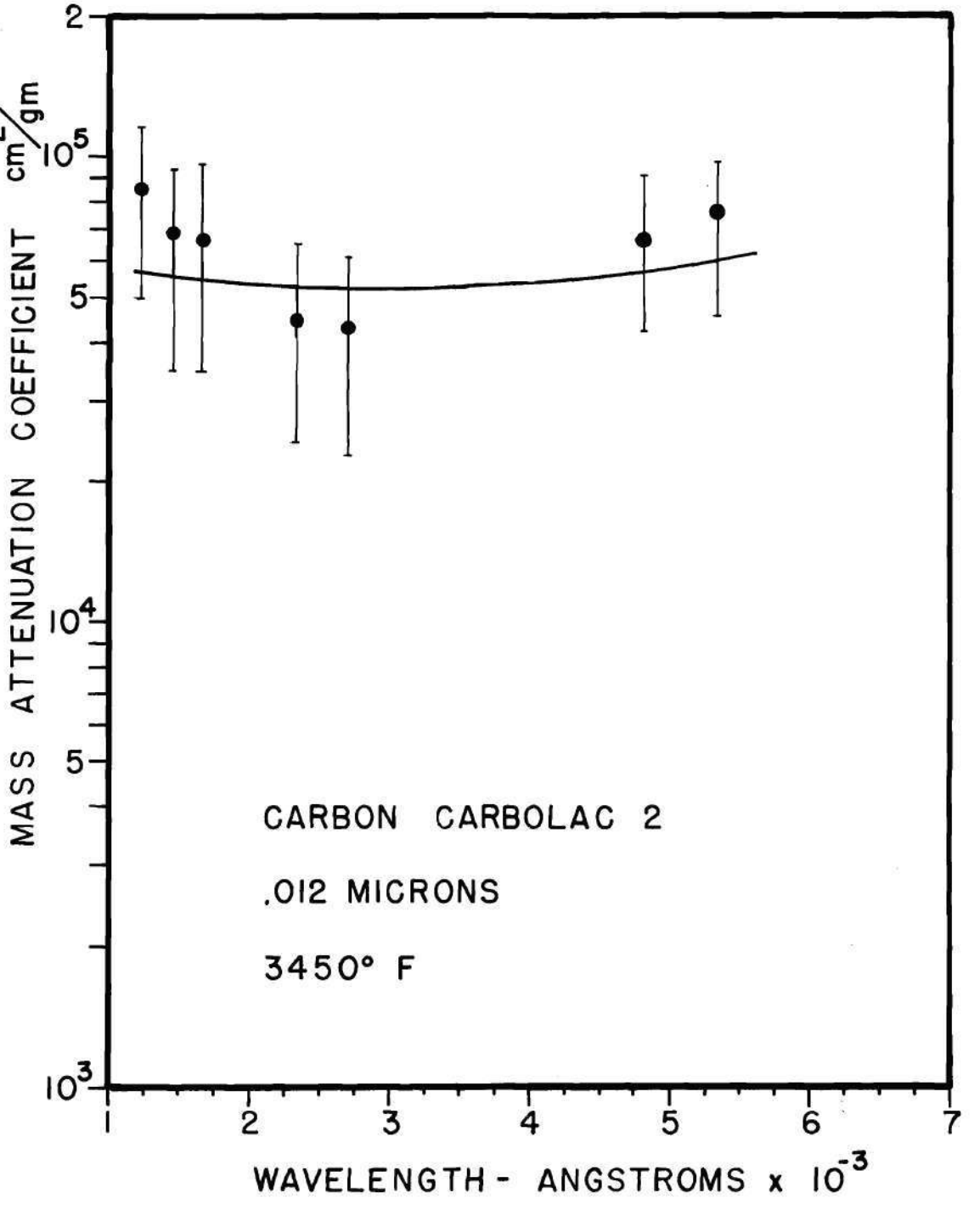

Figure 32. Attenuation Coefficient of Carbon-Hydrogen Aerosol at 3450°F

had to be increased tremendously in order to make attenuation measurements at higher temperatures. The required density was much greater than that which would have been expected due to thermal expansion of gas alone. It is thought that the additional seed material required at higher temperatures serves to produce sufficient concentrations of the reaction products to slow down the reaction rate so that the remaining unreacted particles are observed when the attenuation is measured.

To confirm the disappearance of carbon particles in hydrogen, the linear attenuation coefficient for a given aerosol concentration was measured at different temperatures. At all temperatures the aerosol concentration entering the furnace was maintained constant. Figure 33 shows the linear attenuation coefficient plotted for a hydrogen-carbon aerosol and a nitrogen-carbon aerosol. The experimental values are corrected for the change in the concentration of aerosol due to the thermal expansion of the gas. In the case of the hydrogen-carbon aerosol, the linear attenuation coefficient decreases drastically at temperatures above 1000°F compared to that of nitrogen-carbon aerosol.

Since at higher temperatures part of the carbon apparently undergoes chemical reaction, it is important to know roughly the percent of the carbon that has reacted at a given temperature. This is done by simultaneously sampling the aerosol before it enters the furnace and after it is heated in the furnace. From the difference in the aerosol concentration before and after heating, the percentage of carbon which has reacted is calculated. Figure 34 shows measured values of the percentage of carbon which has reacted as a function of temperature. It is seen that some carbon has reacted even at low temperatures near 1000°F. To confirm

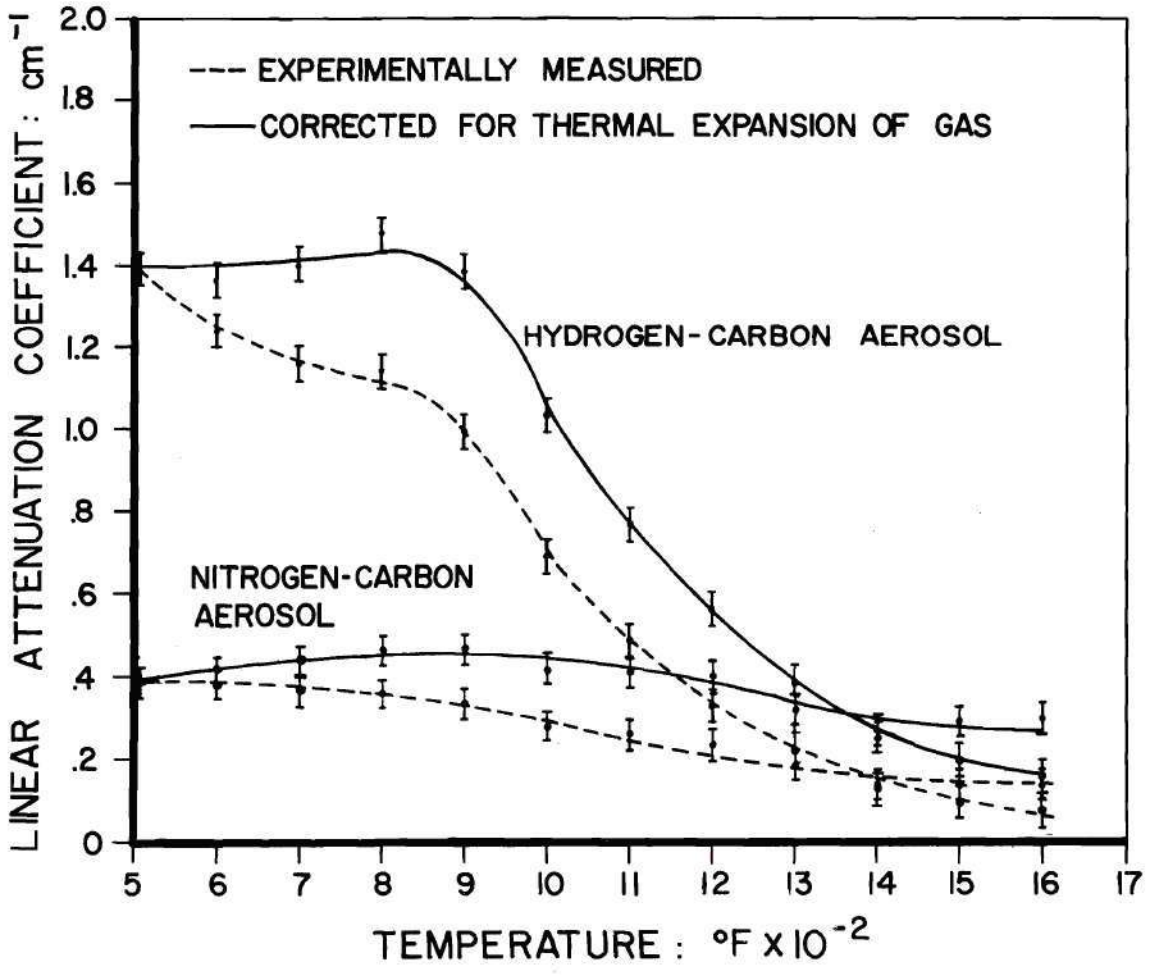

Figure 33. Linear Attenuation Coefficient of Carbon-Hydrogen and Carbon-Nitrogen Aerosols

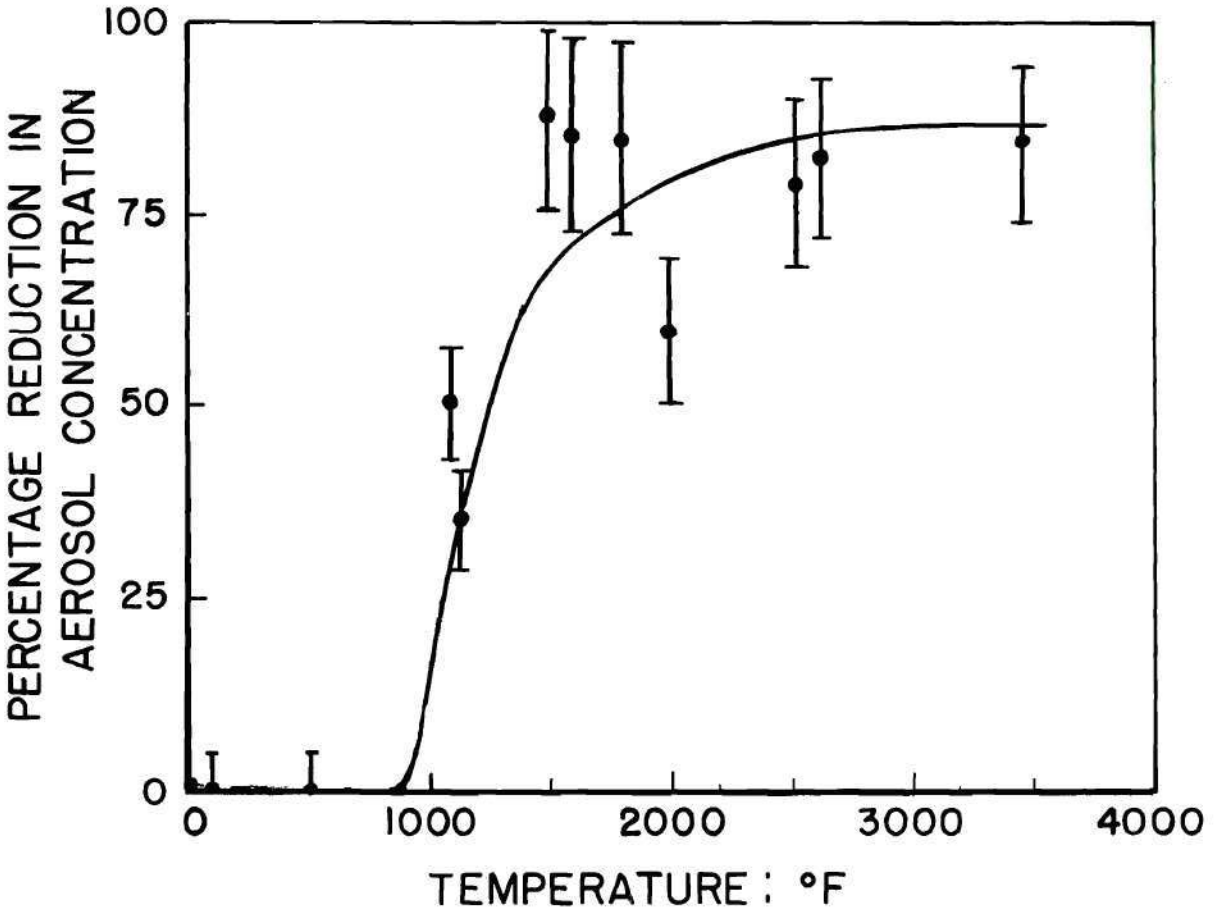

Figure 34. Percentage Reduction in Aerosol Concentration

the chemical reaction, the hot gas exhausting from the furnace was analyzed for methane in the mass spectrograph. The details are given in Appendix F.

To study the effect of chemical reactions on particle size, electron micrographs of the particles were taken after the particles were heated in the furnace. The electron micrographs are given in Appendix D.

Tungsten-Hydrogen Aerosols

The mass absorption coefficient of tungsten particles is measured for 0.04 micron and 0.2 micron diameter particles dispersed in hydrogen. The mass attenuation coefficient of 0.20 micron tungsten is presented as a function of radiation wavelength in Figure 35 at a temperature of 80°F. The absorption coefficient for spherical tungsten particles of diameters 0.02, 0.1, and 0.2 micron was calculated using the Mie theory and is presented in Figure 35. The electron micrographs in Figures 46 through 49 show that the tungsten particles are highly irregular in shape and are a mixture of different sizes. Thus, the experimental values are slightly higher than the theoretical values since the surface to volume ratio is higher. In Figures 35 through 37, the mass attenuation coefficient of 0.20 micron tungsten particles is presented as a function of radiation wavelength. In all of these cases a third degree polynomial is fitted through the experimental points. No significant conclusions are drawn from the shape of these curves.

As in the case of carbon, the mass absorption coefficient of tungsten was found to be essentially independent of wavelength over the range of wavelengths and temperatures investigated. The mass absorption

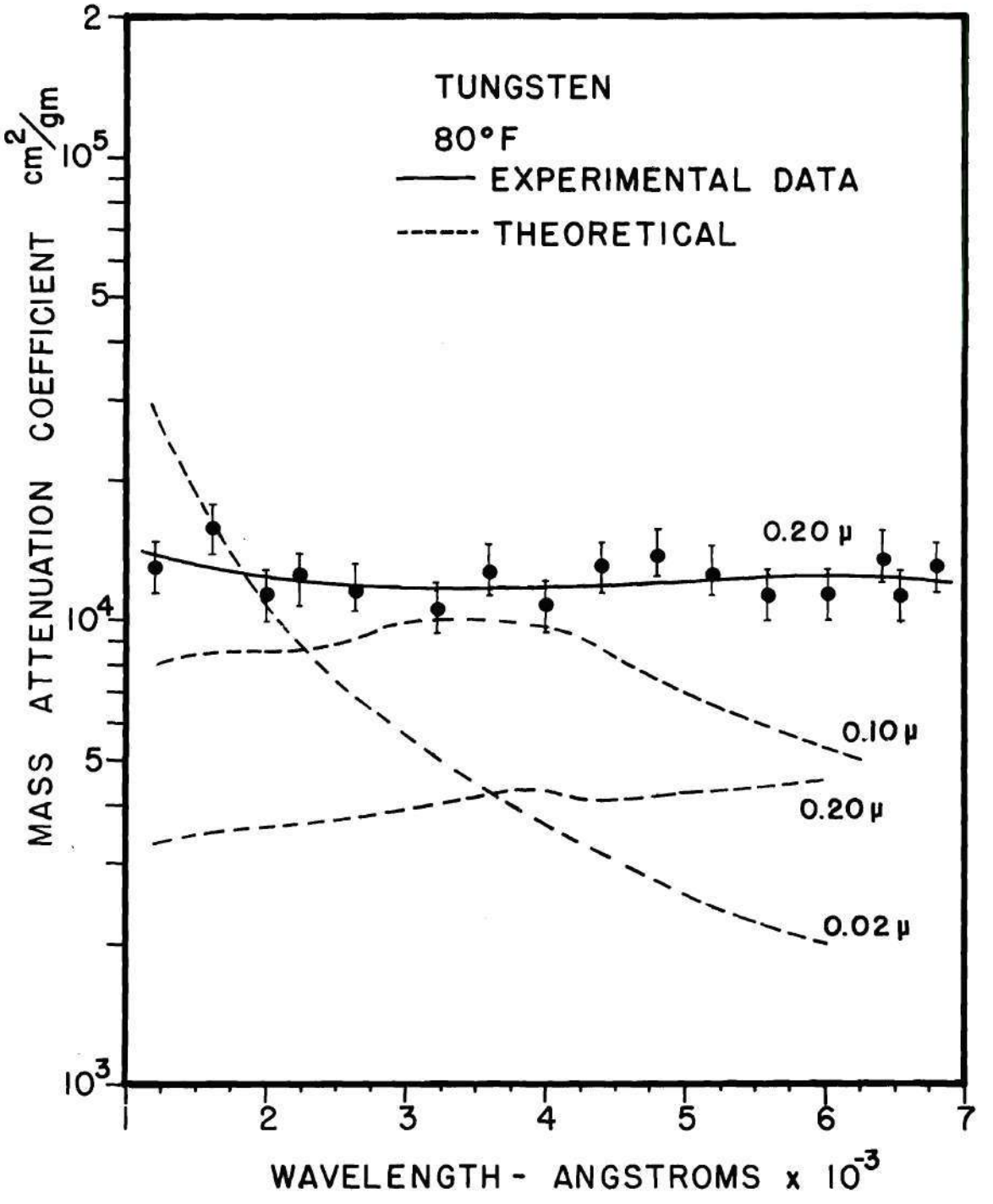

Figure 35. Attenuation Coefficient of Tungsten-Hydrogen Aerosol at 80°F

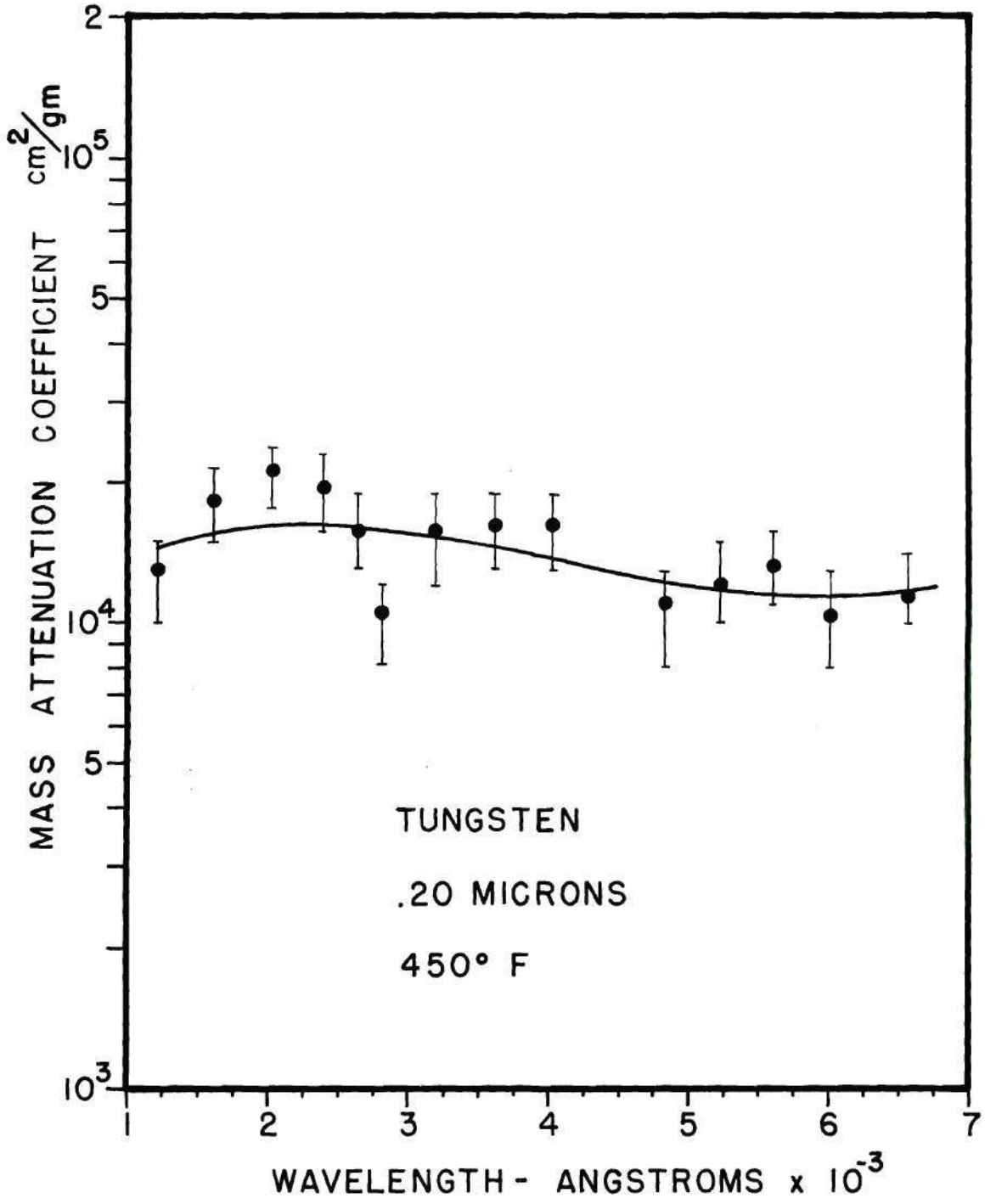

Figure 36. Attenuation Coefficient of Tungsten-Hydrogen Aerosol at 450°F

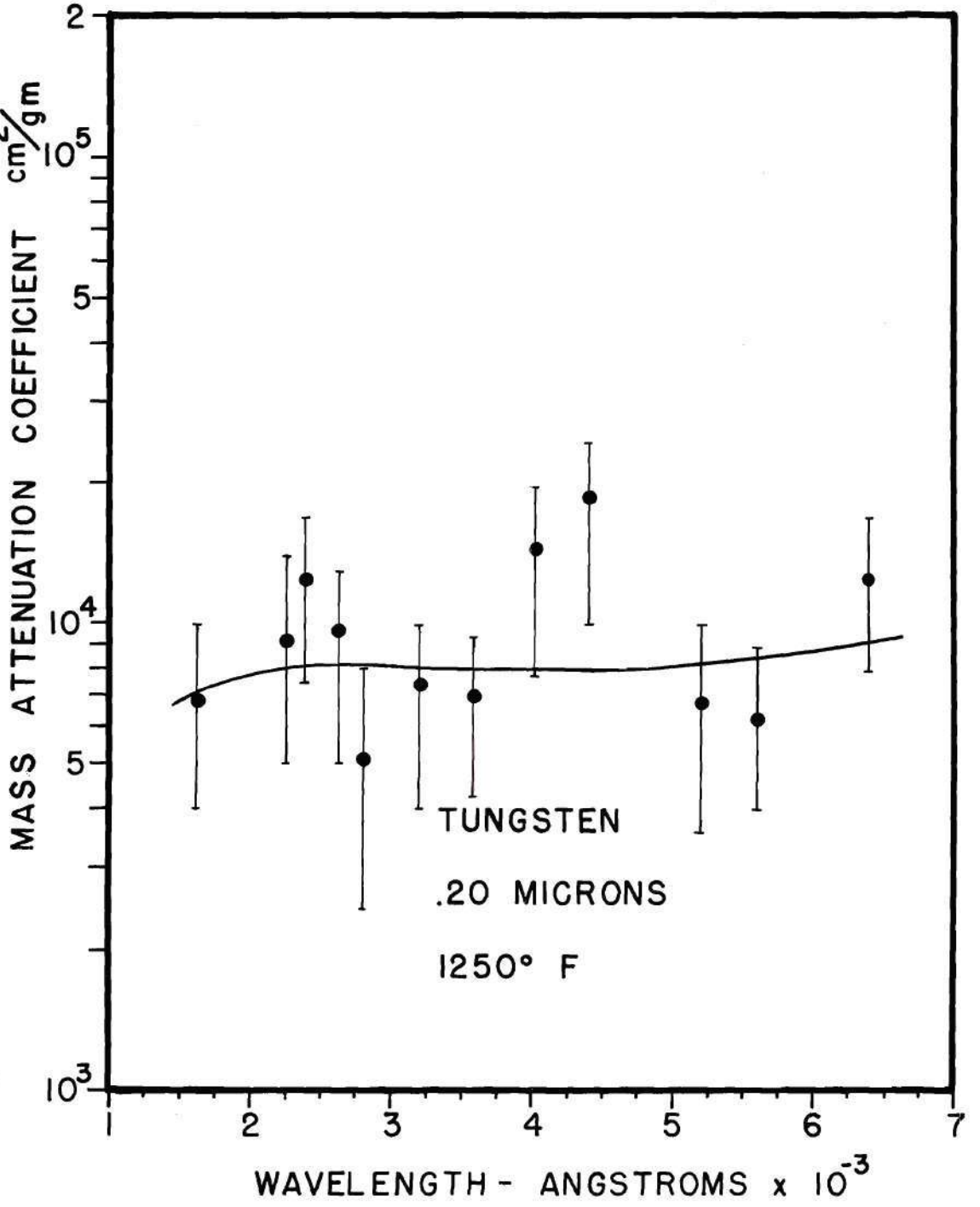

Figure 37. Attenuation Coefficient of Tungsten-Hydrogen Aerosol at 1250°F

coefficient of tungsten is about 20,000 cm^2/gm compared to carbon which has a value of about 50,000 cm^2/gm. In Figures 38 through 42, the mass absorption coefficient of tungsten of .04 micron diameter is presented as a function of radiation wavelength at temperatures of from 80°F to 3000°F. It has been found that tungsten particles of 0.2 micron have a lower mass attenuation coefficient compared to 0.04 micron particles, as expected from equation (56).

Silicon-Hydrogen Aerosols

The theoretical calculations indicate that the silicon has a higher mass absorption coefficient than both carbon and tungsten for sizes below 0.1 micron. The mass absorption coefficient of submicron-sized silicon particles was measured at ambient temperatures and the results are presented in Figure 43. The absorption coefficient for spherical silicon particles of diameters 0.1 and 0.2 micron was calculated using the Mie theory and is also presented in Figure 43 over a limited wavelength range. As in the case of tungsten, the electron micrographs indicate that the particles are nonspherical and are of various sizes. The submicron-sized silicon particles investigated have a mass absorption coefficient of about 65,000 cm^2/gm and are independent of wavelength in the wavelength range investigated.

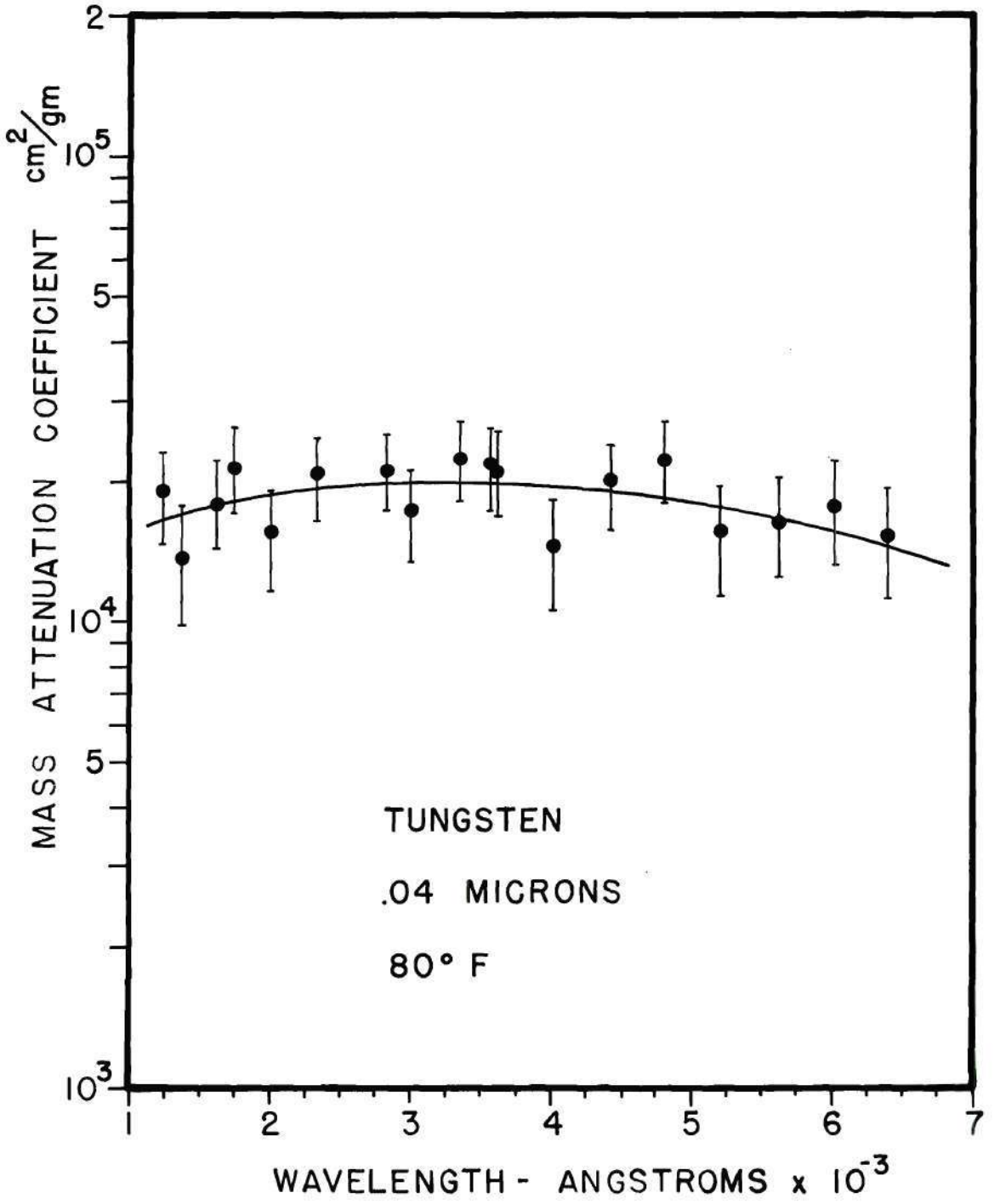

Figure 38. Attenuation Coefficient of Tungsten-Hydrogen Aerosol at 80°F

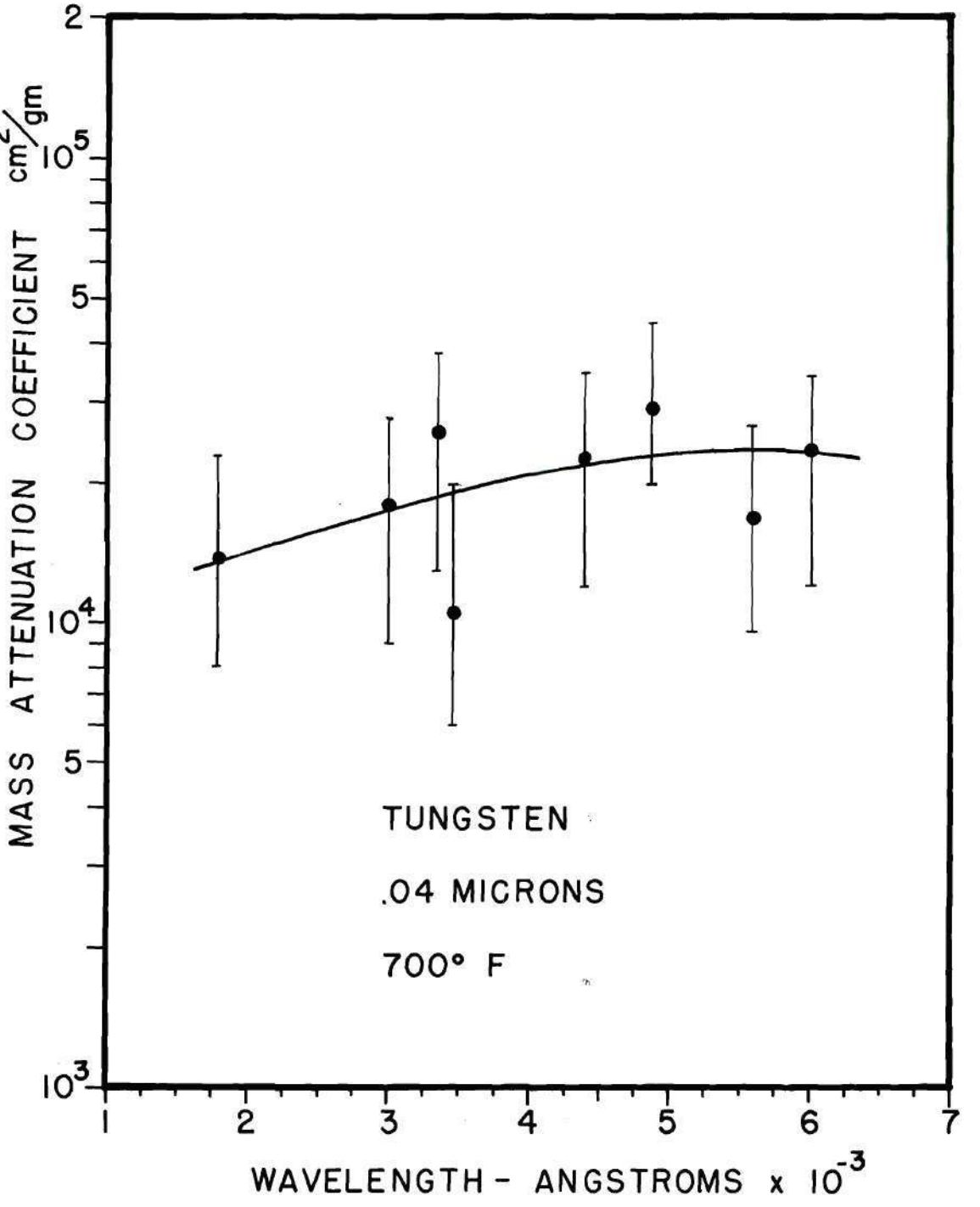

Figure 39. Attenuation Coefficient of Tungsten-Hydrogen Aerosol at 700°F

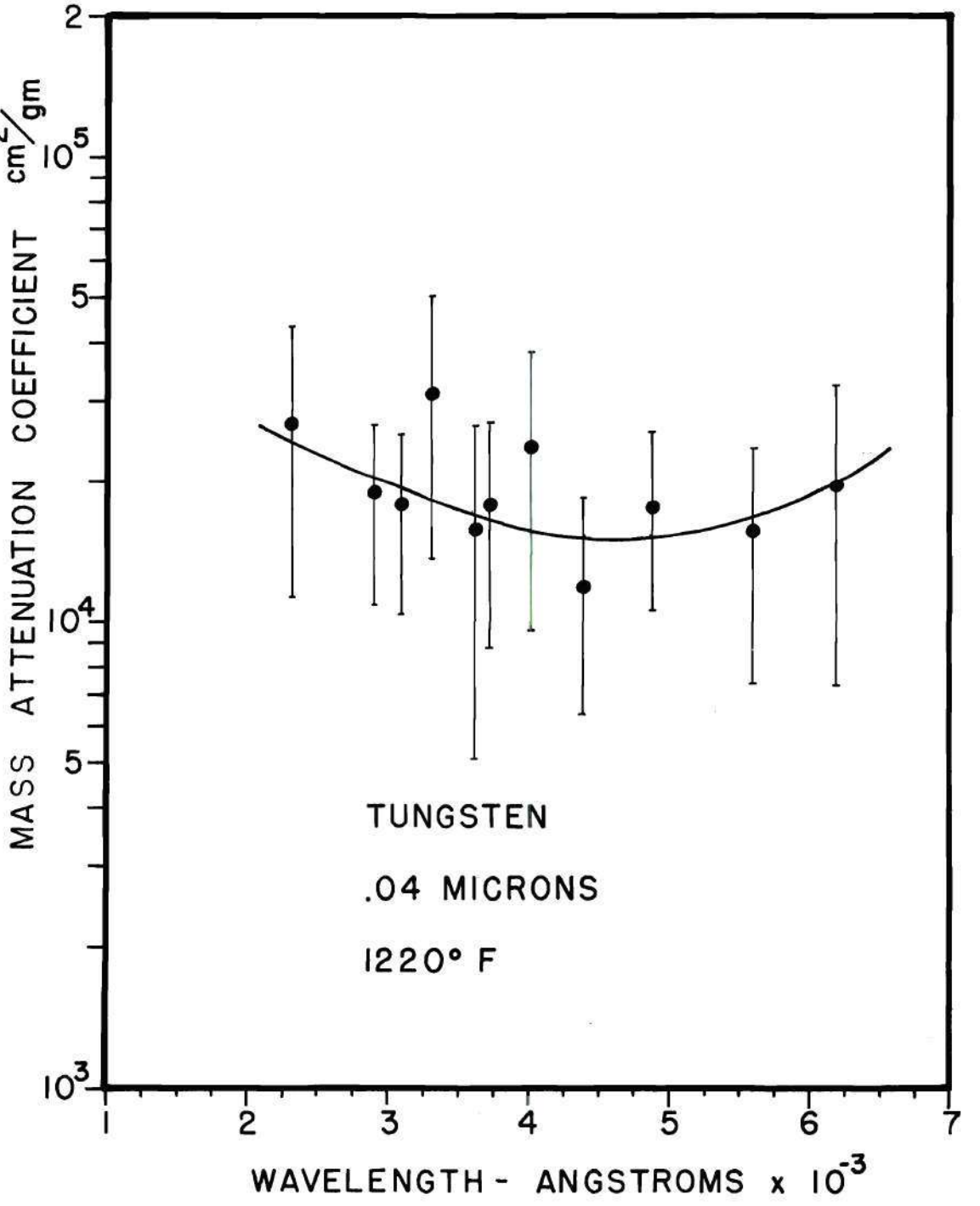

Figure 40. Attenuation Coefficient of Tungsten-Hydrogen Aerosol 1220°F

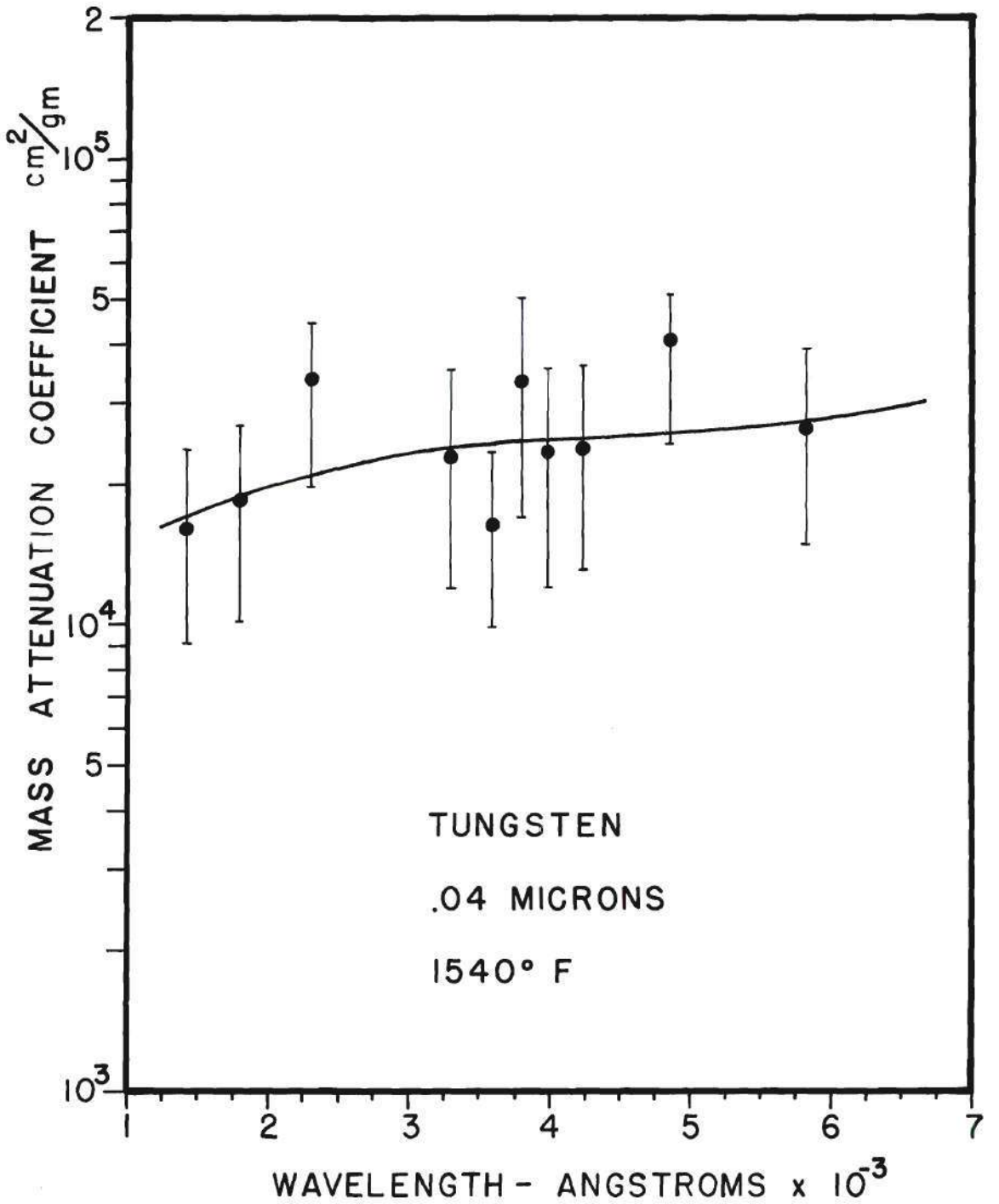

Figure 41. Attenuation Coefficient of Tungsten-Hydrogen Aerosol at 1540°F

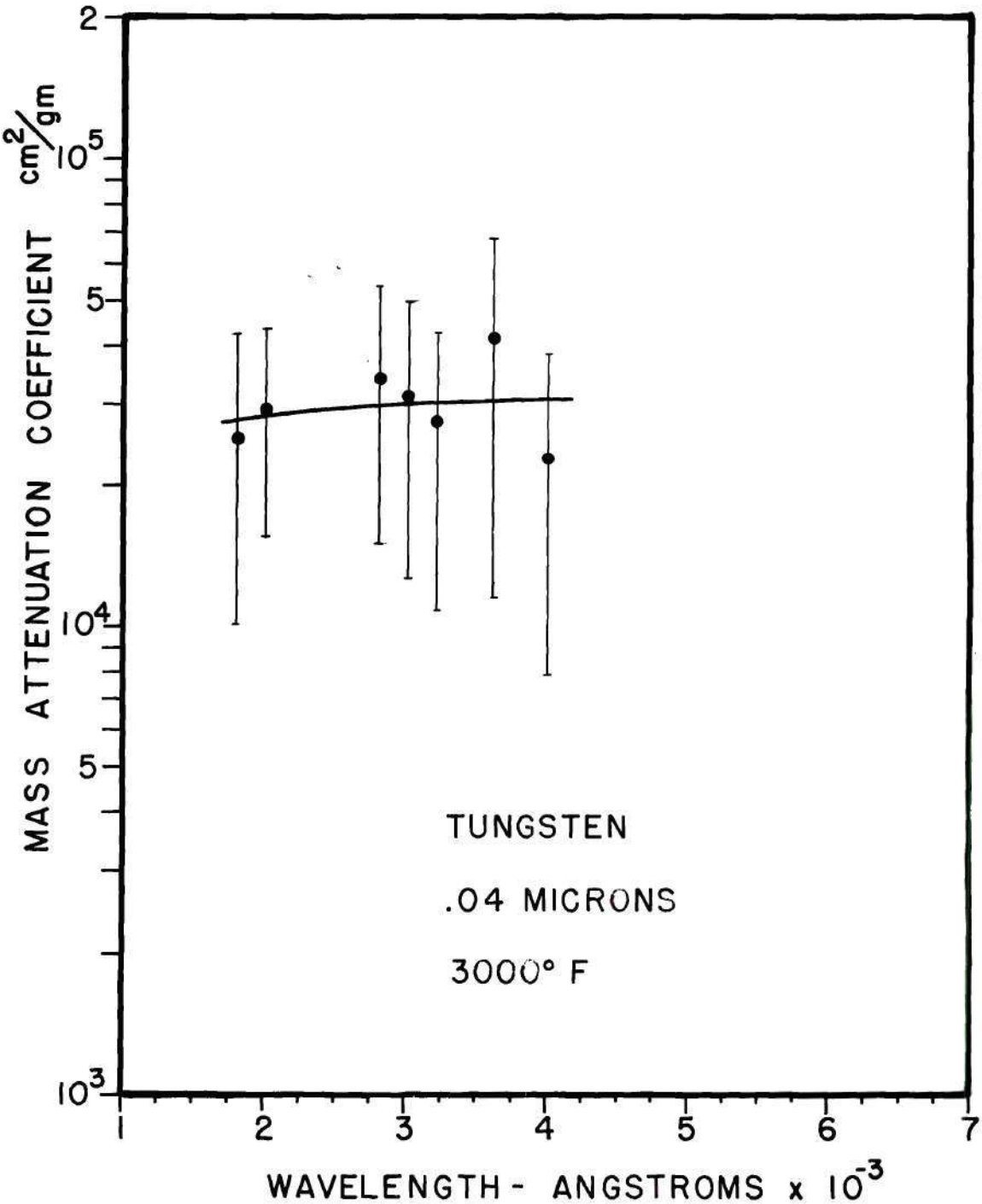

Figure 42. Attenuation Coefficient of Tungsten-Hydrogen Aerosol at 3000° F

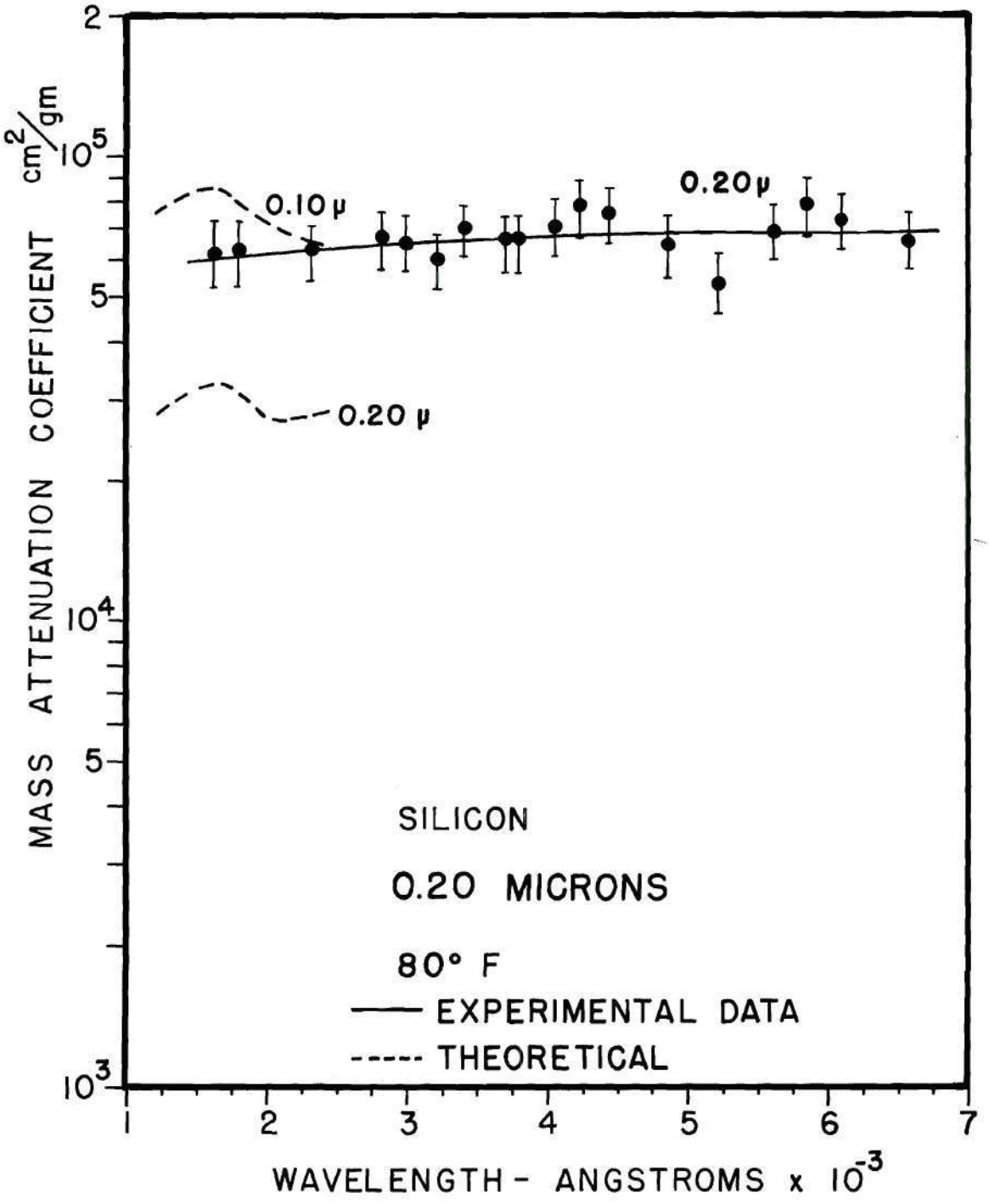

Figure 43. Attenuation Coefficient of Silicon-Hydrogen Aerosol at 80°F

CHAPTER VIII

CONCLUSIONS AND RECOMMENDATIONS

Conclusions

The purpose of this research was to measure the mass attenuation coefficient of hydrogen seeded with submicron-sized particles of various seed materials at elevated temperatures. The measured values have been compared with values calculated using Mie's theory.

Submicron-sized carbon particles with a diameter of 25 millimicrons and less have a high absorption coefficient of the order of 50,000 cm^2/gm which is relatively independent of wavelength and temperature over the wavelength range from 1200 Å to 6000 Å and temperatures up to 3500°F. The mass absorption coefficients calculated using the Mie theory indicate that there is a wavelength dependence for particles of a single size. However, the mass absorption coefficient of a real cloud of particles may correspond to particles of many different sizes such that the sum is essentially wavelength independent. Also, one must remember that in the real case the particles generally are not spheres but are irregularly shaped.

At relatively high temperatures, a large fraction of the carbon disappears apparently due to the chemical reactions between hydrogen and carbon. This is undesirable if carbon is to be used as a seeding material in the gaseous core nuclear rocket engine because as the carbon disappears the aerosol becomes more and more transparent, thereby defeating the pur-

pose of seeding the propellant. One method of overcoming this difficulty may be by using carbon particles of larger diameters which will react with hydrogen more slowly. The larger particles would have a smaller mass attenuation coefficient.

Other seed materials that have been investigated are submicron-sized tungsten and silicon powders. In the case of tungsten particles, the absorption coefficient varies from 10,000 cm^2/gm to 20,000 cm^2/gm depending upon the average size of the particles. Unlike carbon, tungsten particles do not disappear at high temperatures. The experimental values of the mass attenuation coefficient are independent of wavelength and temperature over the range of wavelengths and temperatures investigated. The mass absorption coefficient of tungsten particles calculated using the Mie theory indicates that it is independent of temperature up to 2420° F.

The submicron-sized silicon particles at room temperature have a higher absorption coefficient than carbon and tungsten. The Mie theory indicates that this is only true when the particle size is below 0.1 micron. As the particle size increases, the absorption coefficient drops more rapidly than for carbon, so for particle sizes above 0.1 micron, carbon has a higher absorption coefficient than silicon. The experimentally measured attenuation coefficient is about 65,000 cm^2/gm.

The experimentally measured values of the mass attenuation coefficient are not in direct agreement with theoretically calculated values for spherical particles of a single size. This is because, as the electron micrographs illustrate, the particles are highly irregular in shape and are of various sizes.

Recommendations

The pressure inside the gaseous core nuclear rocket engine would probably be in the range of 100-500 atmospheres,[13] and this would indicate that the absorption parameters should be measured not only as a function of temperature and radiation wavelength but also as a function of pressure. Since the carbon-hydrogen data indicate that chemical reactions take place at higher temperatures and the reaction rates are pressure dependent, it is recommended that the mass attenuation coefficient be measured at higher pressures. Larger carbon particles should be investigated so that the disappearance of the particles is not as pronounced as in the case of 12 and 25 millimicron particles.

The experimental setup can be further improved to take data up to radiation wavelengths of 8000 Å. The photomultiplier presently used is not sensitive in the range above 6000 Å. By using a photomultiplier, such as the EMI 9558QB, sensitive to radiation of wavelength up to 8000 Å, data can be taken in this range.

A more accurate and precise method of measuring the aerosol densities should be used to reduce the error in density measurements which in turn reduces the error in the mass attenuation coefficient.

It is recommended further that the aerosol heating furnace be designed in such a way that the heating element can be more easily replaced without affecting the thermocouples. It is also recommended that the thermocouple holders be made as small as possible so that the gas flow is less disturbed.

In the case of heavy particles like tungsten, a different type of aerosol generator should be used to obtain a dense aerosol so that con-

siderable attenuation can be achieved at higher temperatures. The higher the attenuation the lower will be the error in the mass attenuation coefficient.

A large amount of data can be taken with the present experimental setup. The present data analysis procedure is complicated and time consuming, so the amount of data that can be analyzed is limited. The data handling capability can be increased considerably by employing an automated data collection and reduction system. One suggested approach is to record the intensities from the three photomultipliers on a tape recorder and analyze this information using the computer.

The effluent from the furnace can be analyzed to measure chemical products which may be produced from hydrogen-particle reactions. The effect of chemical reactions on the particle size can be studied more accurately by taking electron micrographs of particles which have been heated. Expensive seed materials can be filtered out and reused in the experiments.

APPENDICES

APPENDIX A

EXPERIMENTAL PROCEDURE

The experimental procedure for a single run in which data were taken is outlined below. A "run" involved taking attenuation data at a single temperature for a series of wavelengths. This involved the following operations.

1. Open the exhaust fan duct by pushing the tie rod.
2. Plug in 220 VAC plug and two 110 VAC plugs.
3. Turn on 28 VDC power supply on console; green light will come on on the pressurization system on the console.
4. Turn on the duct fan, effluent blower, and relay switch and pull out the scram button; red light near scram button will come on.
5. Press the reset button; red light will go off and a green light will come on near scram button indicating 110 VAC/220 VAC power is available for the whole system.
6. Turn on the Honeywell oscillograph and allow it to warm up for a few minutes.
7. Turn on the digital voltmeter and, by shorting the input leads, set the zero; zero has to be checked occasionally.
8. Turn on the photomultiplier power supplies.
9. Turn on all three of the picoammeters.
10. Turn on the capillary discharge power supply.
11. Turn on the coolant water to the capillary discharge light

source and inspect the outlet to make sure that the coolant has a steady flow of water.

12. Turn on the coolant water to furnace jacket.

13. Turn on the water to cool the furnace stack. In this case, the valve is opened so that water just overflows at the outlet.

14. Turn on the spectrometer pressure gauge.

15. Turn on the spectrometer vacuum pump.

16. Turn off the two valves in the sampling line and replace two new filter papers, weighed initially, then turn on the valves on the sampling line.

17. Open the solenoid purge valve to the sampling bottles by throwing the sampling switch on the panel to purge.

18. Open the nitrogen purge by slowly opening the hand valve on the console. This allows nitrogen to bubble through the bottles which can be seen through the Plexiglas window.

19. Open the valve on the hydrogen cylinder for the side ports and adjust the pressure on regulator to about 20 psig.

20. Open the valves on the main nitrogen cylinders and adjust the pressure to about 400 psig.

21. Close the pressure release valve, direct valve, and bypass valve on the console.

22. By turning on a switch on the console, open all the solenoid valves in the gas line which allows the gas to the system.

23. Adjust the flow rate in the side ports by adjusting the valves on the flowmeters.

24. Open the bypass valve to allow the main flow to the furnace.

25. Allow the system to flush out well with nitrogen.

26. Turn on the main heater power supply by operating the 220 V power switch.

27. Open the valves on the flow meters to flow hydrogen into the side ports and adjust the flow.

28. By turning the rheostat clockwise, apply a few volts to the heater and carefully watch the rise in temperature from the digital voltmeter reading.

29. Turn on the high voltage on the photomultipliers by turning on a switch on the power supply.

30. Note the dark current from photomultipliers on the picoammeters.

31. Turn on the monitor light source.

32. Turn on capillary discharge vacuum pump.

33. Turn on capillary discharge fan.

34. Apply a voltage to capillary discharge light to get a discharge.

35. Turn on hydrogen gas for capillary discharge light source.

36. Check water flowing to the capillary discharge light source and adjust if required.

37. Bring the nitrogen flowing in the furnace to the required temperature by increasing the voltage on the heating element in steps of five volts.

38. Turn on power to synchronous motor.

39. Turn on 28 VDC relay power.

40. Turn on automatic drive switch.

41. When the required temperature is approached, change the main flow gas from nitrogen to hydrogen.

42. Adjust the variac to get the required temperature again.

43. Open the shutter between the light source and the furnace.

44. When everything is in order, scan the spectrum without particles.

45. Note that a green light will come on during the forward scanning of the spectrum.

46. As the green light goes off and a red light comes on, close the shutter between the light source and the furnace.

47. Note that the red light will turn off at the end of the spectrum scan.

48. The visicorder gives a plot of intensity versus wavelength without particles, first with shutter open, then with shutter closed.

49. Open the shutter by pressing the rubber ball.

50. Turn on the aerosol generator.

51. Open the direct valve on the console and adjust to get an attenuation of about 10:1 if possible.

52. Turn on the sampling vacuum pump.

53. Press the scanning switch and, at the same time, turn on the sampling switch to draw the aerosol through the sampling apparatus.

54. When the light indicates the end of the forward scan, turn off the sampling switch and, at the same time, close the shutter.

55. The visicorder gives a plot of intensity versus wavelength with particles.

56. Turn off the aerosol generator.

57. Run the experiment again without particles and make sure the intensities of all the photomultipliers have come back to the original values.

58. If the intensities did not come back, adjust the flow rate in the side port and repeat the experiment with and without particles.

59. From the data obtained, calculate the attenuation coefficient of hydrogen with particles at different wavelengths and at a given temperature.

60. Change the main flow from hydrogen to nitrogen.

61. Turn off the two valves in the sampling line and take the samples; replace with new filters.

62. Turn on the two valves in the sampling line once a new filter is replaced.

63. Measure the amount of water displaced in two sampling bottles.

64. Change the temperature of the main gas flow to a different value and repeat the experiment.

APPENDIX B

DATA REDUCTION AND ERROR ANALYSIS PROGRAM

The computer program written for data reduction and analysis is in FORTRAN IV and the program is run on the UNIVAC 1108 at Georgia Tech. The input data to the program are taken from the intensity plots obtained from the Honeywell visicorder. For a given temperature, the program calculates the linear attenuation coefficient at various radiation wavelengths from the intensity data with and without particles. The linear attenuation coefficient is divided by the aerosol density calculated at that wavelength to give the mass attenuation coefficient. The program writes the input data and results are presented in the computer output.

The program also calculates the percentage error associated with the mass attenuation coefficient. The estimated error of each input intensity together with the estimated error of the aerosol density is utilized by the program. The percentage error associated with the mass attenuation coefficient is calculated at each wavelength.

```
      PARAMETER II=17,JJ=30
      DIMENSION TEMP(II),RHOC(II),RHOH(II),AICB(II),AICA(II),AIHB(II),
     1AIHBS(II),AIHA(II),AIHAS(II),J1(II),L1(II),R(II),PART(II)
      DIMENSION DELCOL(II,JJ),AICPCO(II,JJ),DELHOT(II,JJ),
     1LEM(II,JJ),AICP(II,JJ),AICPS(II,JJ),AIHP(II,JJ),AIHPS(II,JJ),
     2AIWB(II,JJ),AIWBS(II,JJ),AIWP(II,JJ),AIWPS(II,JJ),AIWA(II,JJ),
     3AIWAS(II,JJ),AK(II,JJ),AKPRIM(II,JJ),RHOCOP(II,JJ),RHOCO(II,JJ),
     4RHOHOT(II,JJ),AIHPB(II,JJ),AIWAV(II,JJ),AIWPB(II,JJ),
     5AIHPSH(II,JJ),AIHBP(II,JJ),SRHOC(II,JJ),SRHOCP(II,JJ),
     6AICPD(II,JJ),AIHPHO(II,JJ),JELCOL(II,JJ),JELHOT(II,JJ)
      DIMENSION PIWB(II),PIWBS(II),PIWA(II),PIWAS(II),PIWP(II),
     1PIWPS(II),PRHOC(II),PICP(II),PICB(II),PICA(II),PICPS(II),
     2PIHP(II),PIHPS(II),PRHOH(II),PIHB(II),PIHBS(II),PIHA(II),
     3PIHAS(II)
      DIMENSION DIHBPD(JJ),PKPP(JJ),DKP(JJ)
      READ (5,1) I1,X
    1 FORMAT(I2, F7.2)
    2 FORMAT (5X,I3,15X,F5.2)
      WRITE(6,2)  I1,X
      DO 29 M=1,I1
    3 FORMAT(I3,I8,F6.0,2F11.8,6F6.3,F5.3)
      READ (5,3) J1(M),L1(M),TEMP(M),RHOC(M),RHOH(M),AICB(M),AICA(M),
     1AIHB(M),AIHBS(M),AIHA(M),AIHAS(M),R(M)
    4 FORMAT(1H1,I3,I8,F6.0,2F11.8,6F6.3,F5.3)
      WRITE(6,4) J1(M),L1(M),TEMP(M),RHOC(M),RHOH(M),AICB(M),AICA(M),
     1AIHB(M),AIHBS(M),AIHA(M),AIHAS(M),R(M)
    5 FORMAT (4A6 )
      READ (5,5)  (PART(I),I=1,4)
      WRITE(6,5)  (PART(I),I=1,4)
    6 FORMAT(14(F4.2,1X),/,4(F4.2,1X))
      READ (5,6) PICB(M),PIHB(M),PIWB(M),PIHBS(99),PIWBS(M),PICP(M),
     1PIHP(M),PIWP(M),PICPS(M), PIHPS(M), PIWPS(M), PICA(M),PIHA(M),
     2PIWA(M),PIHAS(M),PIWAS(M),PRHOC(M),PRHOH(M)
    7 FORMAT (5X,18F5.3)
      WRITE(6,7) PICB(M),PIHB(M),PIWB(M),PIHBS(99),PIWBS(M),PICP(M),
     1PIHP(M),PIWP(M),PICPS(M), PIHPS(M), PIWPS(M), PICA(M),PIHA(M),
     2PIWA(M),PIHAS(M),PIWAS(M),PRHOC(M),PRHOH(M)
      J = J1(M)
      DO 9 K=1,J
    8 FORMAT (5X,F5.2,5X,F5.3,5X,F5.3,10X,F5.2,5X,F5.3,5X,F5.3)
      READ (5,8) DELCOL(M,K),AICPCO(M,K),AICPD(M,K),DELHOT(M,K),
     1AIHPHO(M,K),AIHPSH(M,K)
      WRITE(6,8) DELCOL(M,K),AICPCO(M,K),AICPD(M,K),DELHOT(M,K),
     1AIHPHO(M,K),AIHPSH(M,K)
    9 CONTINUE
      DO 10 K=1,J
      JELCOL(M,K) = 316*DELCOL(M,K)
   10 JELHOT(M,K) = 316*DELHOT(M,K)
      L2= L1(M)
      DO 13 L=1,L2
   11 FORMAT(5X,I5,7(5X,F5.3),/,3(5X,F5.3))
      READ (5,11)LEM(M,L),AIWB(M,L),AIWBS(M,L),AIWP(M,L),AIHP(M,L),
```

```
     1AICP(M,L),AIWPS(M,L),AIHPS(M,L),AICPS(M,L),AIWA(M,L),AIWAS(M,L)
  12 FORMAT (5X,I5,10F5.3)
     WRITE(6,12)LEM(M,L),AIWB(M,L),AIWBS(M,L),AIWP(M,L),AIHP(M,L),
     1AICP(M,L),AIWPS(M,L),AIHPS(M,L),AICPS(M,L),AIWA(M,L),AIWAS(M,L)
  13 CONTINUE
     AICAV =(0.5)*(AICB(M)+AICA(M))
     AIHAV = (0.5)*(AIHB(M)-AIHBS(M)+AIHA(M)-AIHAS(M))
     DICAVS =0.25*((AICB(M)*PICB(M))**2+(AICA(M)*PICA(M))**2)
     PICAVS = DICAVS/AICAV**2
     DIHAVS = 0.25*((AIHB(M)*PIHB(M))**2+(AIHBS(M)*PIHBS(M))**2+
     1(AIHA(M)*PIHA(M))**2+(AIHAS(M)*PIHAS(M))**2)
     PIHAVS = DIHAVS/AIHAV**2
     SDELHO = 0.0
     SDELCO = 0.0
     SUM1 = 0.0
     SUM2 = 0.0
     SUM5 = 0.0
     SUM6 = 0.0
     SUM7 = 0.0
     SUM8 = 0.0
     DO 14 K=1,J
     SUM1 = SUM1+(DELCOL(M,K)*(ALOG(AICAV/AICPCO(M,K))))
     SDELCO = SDELCO+DELCOL(M,K)
  14 SDELHO = SDELHO+DELHOT(M,K)
     RC = (RHOC(M)*SDELCO)/SUM1
     DO 15 K=1,J
     SRHOC(M,K) = RC*(ALOG(AICAV/AICPCO(M,K)))
     SRHOCP(M,K) = RC*(ALOG(AICAV/AICPD(M,K)))
     AIHBP(M,K) = AIHPHO(M,K)-AIHPSH(M,K)*SRHOC(M,K)/SRHOCP(M,K)
  15 SUM2 = SUM2+(DELHOT(M,K)*(ALOG(AIHAV/AIHBP(M,K))))
     RH = (RHOH(M)*SDELHO)/SUM2
     DO 16 K=1,J
     DIHBPD(K) = (AIHPHO(M,K)*PIHP(M))**2+(SRHOC(M,K)*AIHPSH(M,K)*
     1PIHPS(M)/SRHOCP(M,K))**2+(AIHPSH(M,K)*SRHOC(M,K)*PPHOC(M)/
     2SRHOCP(M,K))**2+(AIHPSH(M,K)*SRHOC(M,K)*PRHOC(M)/SRHOCP(M,K))**2
     SUM5 = SUM5+((DELHOT(M,K)*(RH**2)/(RHOH(M)*SDELHO*AIHBP(M,K)
     1))**2)*DIHBPD(K)
     SUM6 =SUM6+( DELHOT(M,K)/AIHAV)
     SUM7 = SUM7 + ( DELCOL(M,K)*(PICAVS)**0.5)
  16 SUM8 = SUM8 +  (DELCOL(M,K)*PICP(M)*(RC**2)/(RHOC(K)*SDELCO))**2
     DRHS =  (RH*PRHOH(M))**2 +((SUM6*(RH**2)/(RHOH(M)*SDELHO))**2)
     1*DIHAVS+SUM5
     DRCS = (RC*PRHOC(M))**2 + (SUM7*(RC**2)/(RHOC(M)*SDELCO))**2
     1+SUM8
     DO 17 L=1,L2
     AIHPB(M,L) = AIHP(M,L)-AIHPS(M,L)*(ALOG(AICAV/AICP(M,L)))/
     1ALOG(AICAV/AICPS(M,L))
     AIWAV(M,L) = 0.5*(AIWB(M,L)-AIWBS(M,L)+AIWA(M,L)-AIWAS(M,L))
     RHOCO(M,L) = RC*ALOG(AICAV/AICP(M,L))
     RHOCOP(M,L)= RC*ALOG(AICAV/AICPS(M,L))
     RHOHOT(M,L)= RH*ALOG(AIHAV/AIHPB(M,L))
     AIWPB(M,L) = AIWP(M,L)-AIWPS(M,L)*RHOCO(M,L)/RHOCOP(M,L)+0.25*
     1(AIWBS(M,L)+AIWAS(M,L))*(1.0+AIHPB(M,L)/AIHAV)*(RHOCO(M,L)/
     2RHOCOP(M,L)-1.0)
     AK(M,L) = ALOG(AIWAV(M,L)/AIWPB(M,L))/X
     AKPRIM(M,L) = AK(M,L)/RHOHOT(M,L)
     DIHPBS = (AIHP(M,L)*PIHP(M))**2 + (RHOCO(M,L)*AIHPS(M,L)*PIHPS(M)/
     1RHOCOP(M,L))**2 +2.0*( AIHPS(M,L)*RHOCO(M,L)*PRHOC(M)/RHOCOP(M,L))
```

```
   2**2
    PIHPBS = DIHPBS/(AIHPB(M,L))**2
    PRHOHO = DRHS/(RH)**2 + (PIHAVS+PIHPBS)/(ALOG(AIHAV/AIHPB(M,L)))
   1**2
    DIWAVS = 0.25*((AIWB(M,L)*PIWB(M))**2 + (AIWBS(M,L)*PIWBS(M))**2+
   1(AIWA(M,L)*PIWA(M))**2 + (AIWAS(M,L)*PIWAS(M))**2)
    C1 =  AIWBS(M,L) + AIWAS(M,L)
    C2 = 1.0+AIHPB(M,L)/AIWAV(M,L)
    C3 = RHOCO(M,L)/RHOCOP(M,L) - 1.0
    DC1S = (0.25*C2*C3*AIWBS(M,L)*PIWBS(M))**2
    DC2S = (0.25*C2*C3*AIWAS(M,L)*PIWAS(M))**2
    DC3S =((0.25*C1*C3/AIWAV(M,L))**2)*DIHPBS
    DC4S =((0.25*C1*C3*AIHPB(M,L)/(AIWAV(M,L))**2 )**2)*DIWAVS
    DC5S = (0.25*C1*C2*RHOCO(M,L)*PRHOC(M)/RHOCOP(M,L))**2
    DC6S = DC5S
    DCSS = DC1S+DC2S+DC3S+DC4S+DC5S+DC6S
    DRHOCN =((ALOG(AICAV/AICP(M,L)))**2)*DRCS +(RC**2)*PICAVS +
   1(RC*PICP(M))**2
    DRHOCP =((ALOG(AICAV/AICPS(M,L)))**2)*DRCS +(RC**2)*PICAVS +
   1(RC*PICPS(M))**2
    DBS = (RHOCO(M,L)*AIWPS(M,L)*PIWPS(M)/RHOCOP(M,L))**2  +
   1(AIWPS(M,L)/RHOCOP(M,L))**2 *DRHOCN +(AIWPS(M,L)*RHOCO(M,L)/
   2(RHOCOP(M,L))**2)**2 *DRHOCP
    DAS = (AIWP(M,L)*PIWP(M))**2
    PIWPB = (DAS+DBS+DCSS)/(AIWPB(M,L))**2
    PIWAV =(0.25*((AIWB(M,L)*PIWB(M))**2 + (AIWBS(M,L)*PIWBS(M))**2 +
   1 (AIWA(M,L)*PIWA(M))**2 +(AIWAS(M,L)*PIWAS(M))**2))/AIWAV(M,L)**2
    PKS = (PIWAV+PIWPB)/ (ALOG(AIWAV(M,L)/AIWPB(M,L)))**2
    PKPS = PKS + PRHOHO
    PKP = SQRT(PKPS)
    PKPP(L)=100.0*PKP
17 DKP(L) = AKPRIM(M,L)*PKP
18 FORMAT(1H1,5X,15HSEED MATERIAL: ,4A6, 21X,15HPARTICLE SIZE: ,F4.3,
   19H MICRON .,//,36X,14H TEMPERATURE =,F6.0,3H F.,///,43X,
   210HDATA INPUT,//)
    WRITE (6,18) (PART(I),I=1,4),R(M),TEMP(M)
19 FORMAT(5X,6H ICB= ,F5.3,3X,6H IHB =,F5.3,3X,7H IHAS =,F5.3,3X,
   17H IHBS =,F5.3,3X,6H IHA =,F5.3,3X,6H ICA =,F5.3,////,22X,6HRHOC =
   2,F10.8,21X,6HRHOH =,F10.8,//)
    WRITE (6,19) AICB(M),AIHB(M),AIHAS(M),AIHBS(M),AIHA(M),AICA(M),
   1RHOC(M),RHOH(M)
20 FORMAT(1H,15X,6HDELCOL,5X,6HAICPCO,5X,5HAICPD,10X,6HDELHOT,5X,
   16HAIHPHO,5X,6HAIHPSH,/)
    WRITE (6,20)
    DO 22 K=1,J
21 FORMAT(1H0,16X,I4,5X,F6.3,5X,F5.2,12X,I4,5X,F6.3,5X,F6.3)
22 WRITE (6,21) JELCOL(M,K),AICPCO(M,K),AICPD(M,K),JELHOT(M,K),
   1AIHPHO(M,K),AIHPSH(M,K)
23 FORMAT(1H0,//,6X,5HLEMDA,3X,4H IWB,4X,4HIWBS,4X,4H IWP,4X,4H IHP,
   14X,4H ICP,4X,4HIWPS,4X,4HIHPS,4X,4HICPS,4X,4H IWA,4X,4HIWAS,/)
    WRITE (6,23)
    DO 25 L=1,L2
24 FORMAT (1H0,5X,I4,E10.3, 9E8.3)
25 WRITE (6,24) LEM(M,L),AIWB(M,L),AIWBS(M,L),AIWP(M,L),AIHP(M,L),
   1AICP(M,L),AIWPS(M,L),AIHPS(M,L),AICPS(M,L),AIWA(M,L),AIWAS(M,L)
    WRITE (6,30) (PART(I),I=1,4),R(M),TEMP(M)
26 FORMAT(1H,14X,10HWAVELENGTH,5X,6HK CM-1,5X,4HRHO ,6X,6HK MASS,
   15X,5HDEL K,6X,10HPCT ERROR /
```

```
  215X,9HANGSTROMS,16X,6HGMS/CC,5X,6HCM2/GM,5X,6HCM2/GM//)
   WRITE (6,26)
   DO 28 L=1,L2
27 FORMAT(1H0,I21,F13.4,F12.7,F10.0,F11.0,F11.2)
28 WRITE (6,27) LEM(M,L),AK(M,L),RHOHOT(M,L),AKPRIM(M,L),DKP(L),
  1PKPP(L)
29 CONTINUE
30 FORMAT(1H1,14X,14HSEED MATERIAL:,4A6,14HPARTICLE SIZE:,F4.3,
  19H MICRON .,//,36X,14H TEMPERATURE =,F6.0,3H F.,////,42X,
  28H RESULTS//)
   END
```

SEED MATERIAL: TUNGSTEN PARTICLE SIZE: .040 MICRON .

TEMPERATURE = 3000. F.

DATA INPUT

ICB= .780 IHB = .350 IHAS = .000 IHBS = .000 IHA = .350 ICA = .770

RHOC = .00005990 RHOH = .00000229

DELCOL	AICPCO	AICPD	DELHOT	AIHPHO	AIHPSH
979	.260	.67	979	.330	.000
2528	.200	.73	2528	.340	.000
979	.180	.68	979	.330	.000
1927	.240	.51	1927	.330	.000
1832	.210	.20	1832	.330	.000

LEMDA	IWB	IWBS	IWP	IHP	ICP	IWPS	IHPS	ICPS	IWA	IWAS
1800	.815-00	.000	.750-00	.330-00	.185-00	.000	.000	.700-00	.815-00	.000
2000	.220-00	.000	.190-00	.320-00	.175-00	.000	.000	.675-00	.220-00	.000
2300	.435-00	.000	.410-00	.326-00	.180-00	.000	.000	.670-00	.440-00	.000
2800	.280-00	.000	.250-00	.330-00	.280-00	.000	.000	.620-00	.280-00	.000
3000	.300-00	.000	.275-00	.330-00	.260-00	.000	.000	.650-00	.310-00	.000
3200	.400-00	.000	.370-00	.330-00	.250-00	.000	.000	.675-00	.410-00	.000
3400	.850-00	.000	.810-00	.330-00	.250-00	.000	.000	.670-00	.860-00	.000
3600	.910-00	.000	.850-00	.340-00	.250-00	.000	.000	.650-00	.910-00	.000
4000	.560-00	.600-02	.520-00	.330-00	.240-00	.600-02	.000	.620-00	.560-00	.600-02

SEED MATERIAL:TUNGSTEN PARTICLE SIZE:.040 MICRON .

TEMPERATURE = 3000. F.

RESULTS

WAVELENGTH ANGSTROMS	K CM-1	RHO GMS/CC	K MASS CM2/GM	DEL K CM2/GM	PCT ERROR
1800	.0693	.0000027	25542.	15906.	62.27
2000	.1222	.0000041	29582.	14196.	47.99
2300	.0541	.0000033	16525.	10306.	62.36
2800	.0944	.0000027	34827.	20535.	58.96
3000	.0863	.0000027	31819.	19009.	59.74
3200	.0753	.0000027	27776.	16995.	61.19
3400	.0451	.0000027	16615.	11821.	71.15
3600	.0568	.0000013	42548.	41919.	98.52
4000	.0636	.0000027	23467.	15546.	66.25

APPENDIX C

TYPICAL PROPERTIES OF SEED MATERIALS

The various submicron-sized particles of the same material can be produced by a number of different manufacturing processes. The physical properties of these materials vary from one kind of material to another. Since the mass attenuation coefficient of any material depends on its physical properties, it is important to note the physical properties of possible seed materials. Listed below are some of the physical properties of the seed materials of interest.

Carbon

Source: Cabot Corporation

	Spheron 6	Carbolac 2	Sterling MT
Smallest particle diameter	0.025 μ	0.012 μ	0.250 μ
Surface Area	110 sq meters per gram	850 sq meters per gram	7 sq meters per gram
Fixed carbon	95%	87%	99.5%
Volatile content	5%	13%	0.5%
Bulk density	22 lb/cft	6 lb/cft	33 lb/cft

Tungsten

Source: Vitro Laboratories

Color : Black to gray

Smallest particle diameter 0.04 to 0.2 micron

Bulk density	from 1 to 3 gm/cc
Surface area	4 to 6 sq meters/gm
Stability	finer sizes pyrophoric in air
Particle shape	irregular

Silicon

Source: Consolidated Astronautics

Purity: 98%

Mesh size: -200

APPENDIX D

ELECTRON MICROGRAPHS OF AEROSOL PARTICLES

The electron micrographs of various seed materials taken under various operating conditions are given in Figures 44 through 51. An aerosol of submicron-sized particles can be produced by a number of different methods. The aerosol produced can be collected on a microscope grid in a number of ways. The electrostatic precipitation sampling method gives a quite representative sample of particles. All of the samples given in the illustrations are obtained by the electrostatic precipitation method. Aerosols of submicron-sized particles are produced by passing gas through a test tube containing submicron-sized particles unless otherwise stated.

Figure 44 shows the electron micrographs of carbon particles of four different varieties taken under the same magnification. Figure 45 shows the electron micrograph of carbon (Spheron 6) particles deagglomerated through a nozzle at various magnifications. In Figures 46 and 47, the electron micrographs of tungsten particles are shown both before and after deagglomeration through a nozzle. Figure 48 shows the electron micrographs of submicron-sized particles of four different sizes under the same magnification. In Figure 49, the same four sizes of tungsten are shown at a higher magnification. In Figure 50, electron micrographs of tungsten, tungsten carbide, silicon, and silicon carbide are shown under the same magnification. Figure 51 shows the electron micrographs

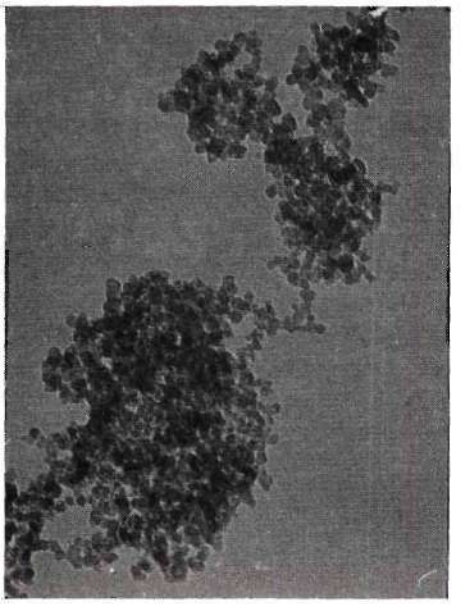

Carbolac 2: 0.012 Micron.

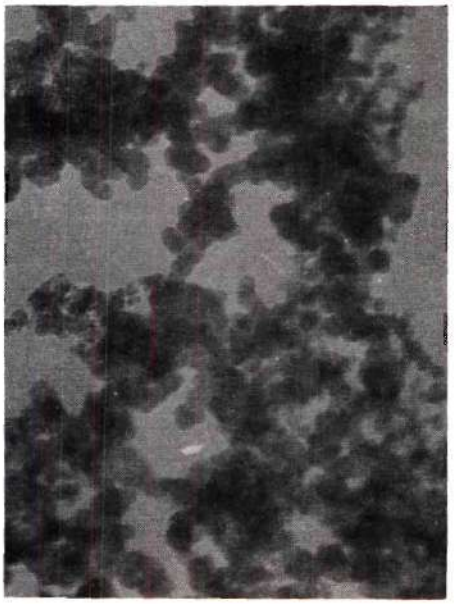

Black Pearls: 0.012 Micron.

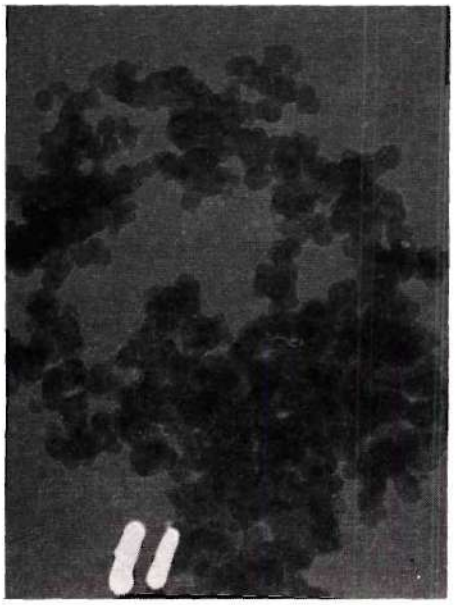

Spheron 6: 0.025 Micron.

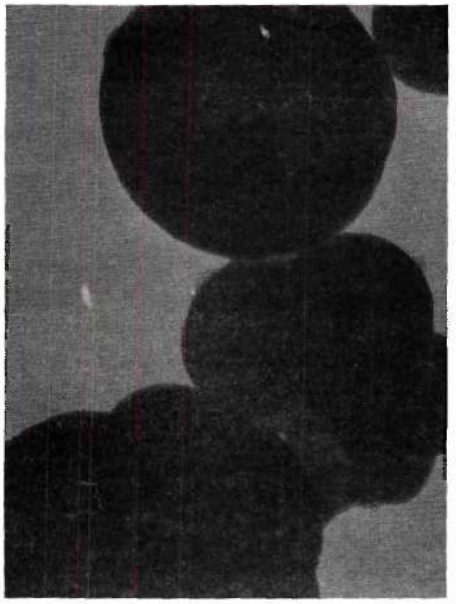

Sterling M.T.: 0.250 Micron.

0.1 Micron.

Figure 44. Electron Micrographs of Various Types of Carbon Particles

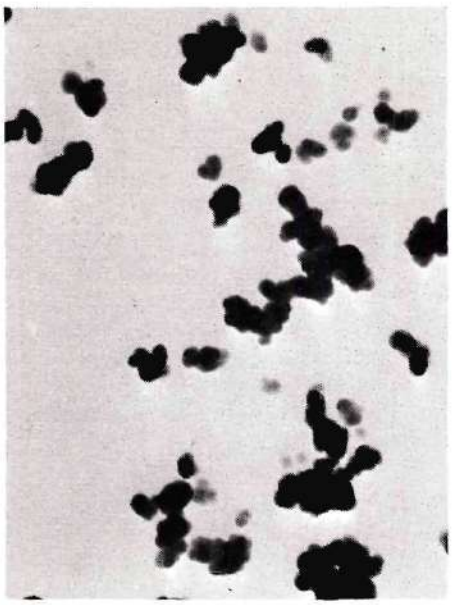

0.1 Micron.

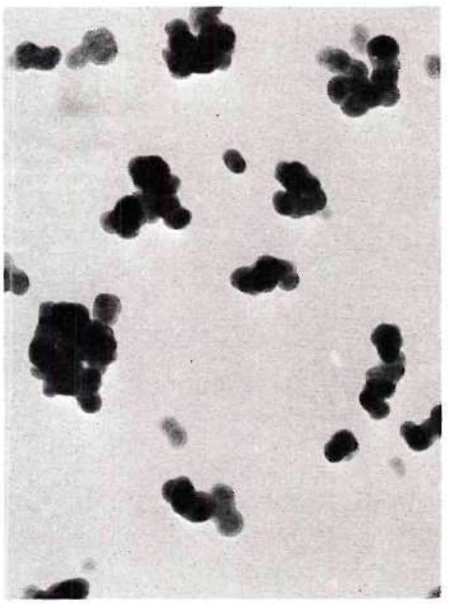

0.1 Micron.

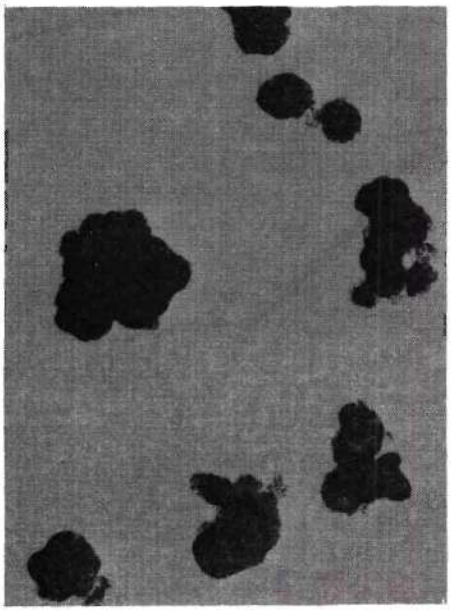

0.1 Micron.

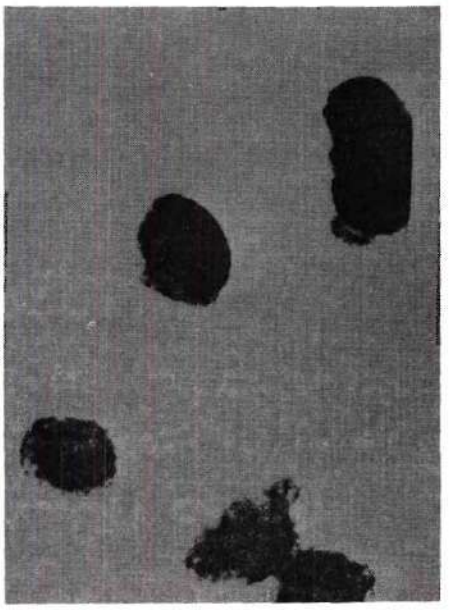

0.1 Micron.

Figure 45. Electron Micrographs of Carbon (Spheron 6) When Deagglomerated by Nozzle.

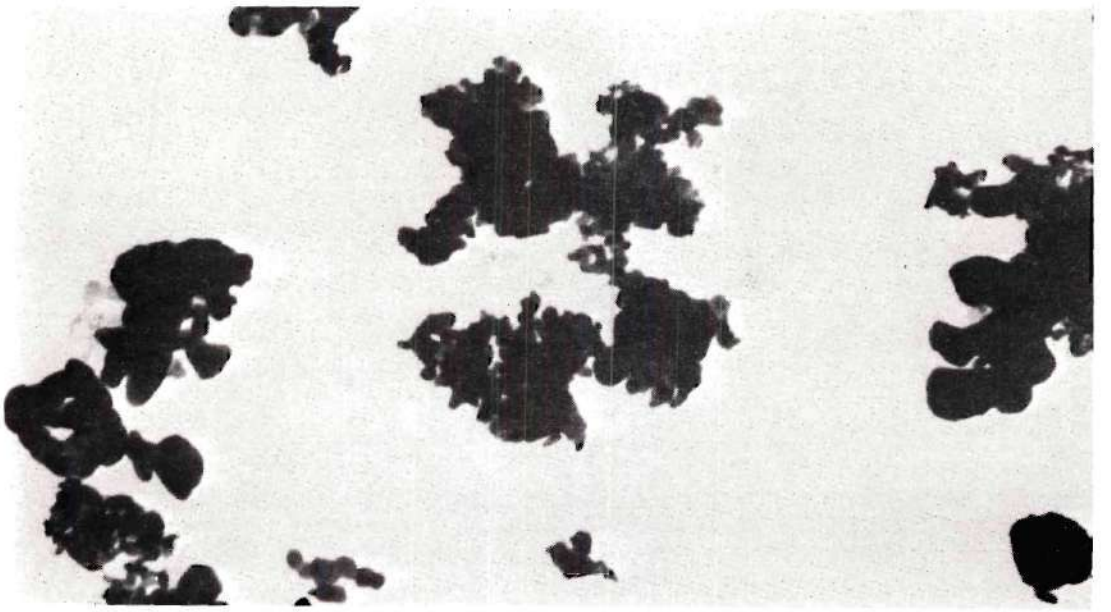

Without Deagglomeration.

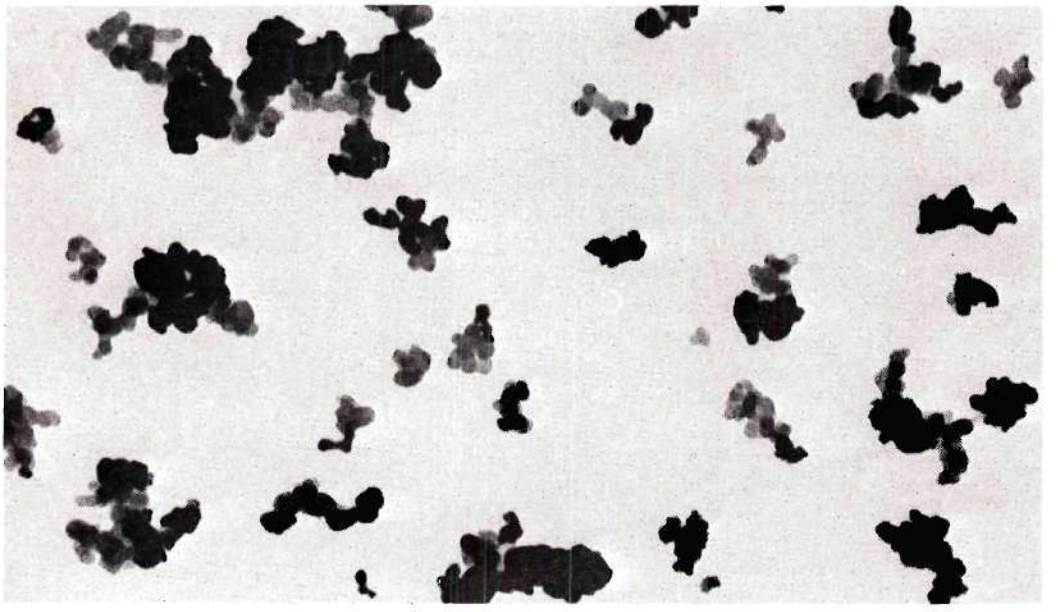

With Deagglomeration.

0.1 Micron.

Figure 46. Electron Micrographs of Tungsten Particles With and Without Deagglomeration

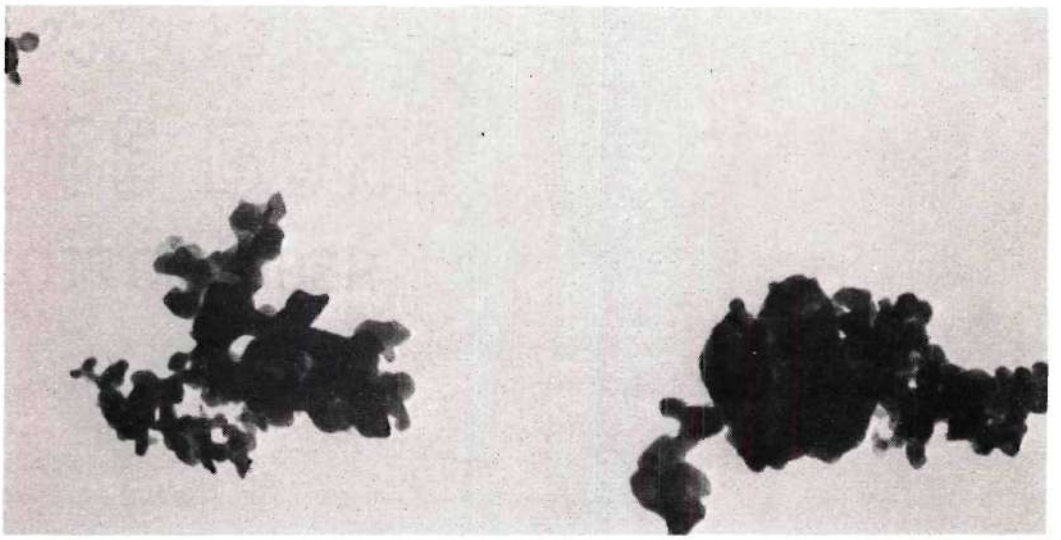

Without Deagglomeration.

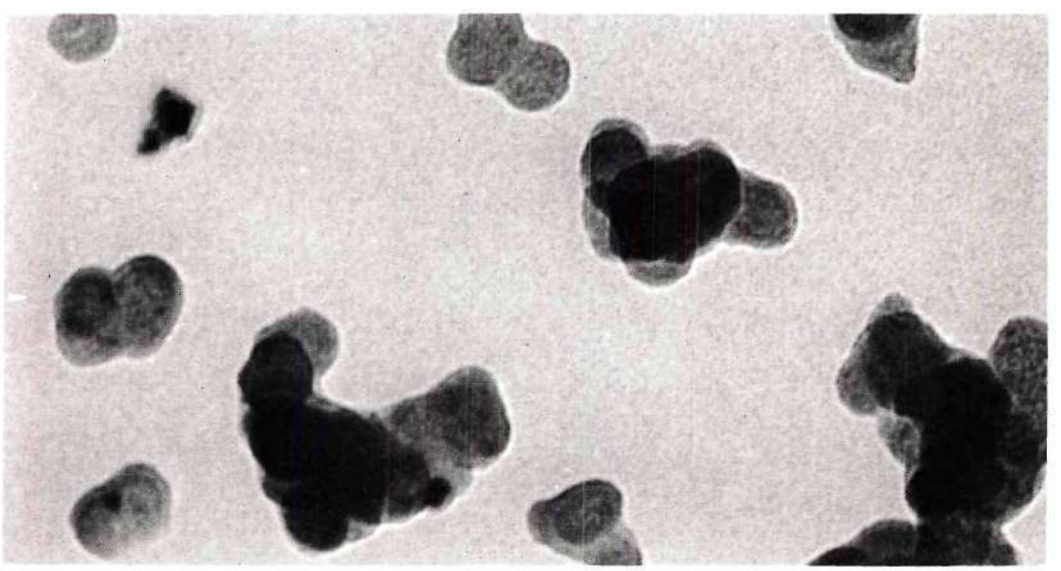

With Deagglomeration.

0.1 Micron.

Figure 47. Electron Micrographs of Tungsten Particles With and Without Deagglomeration

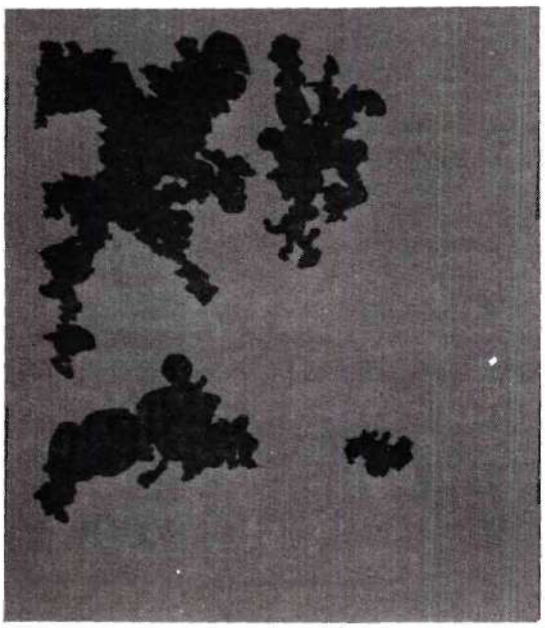

0.2 Micron.

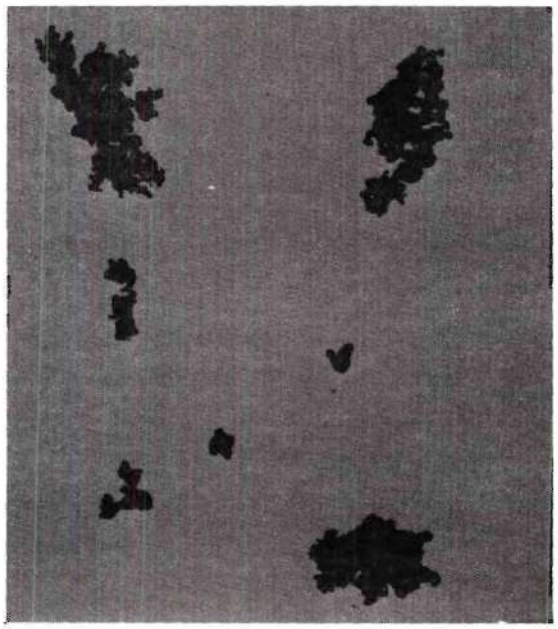

0.1 Micron.

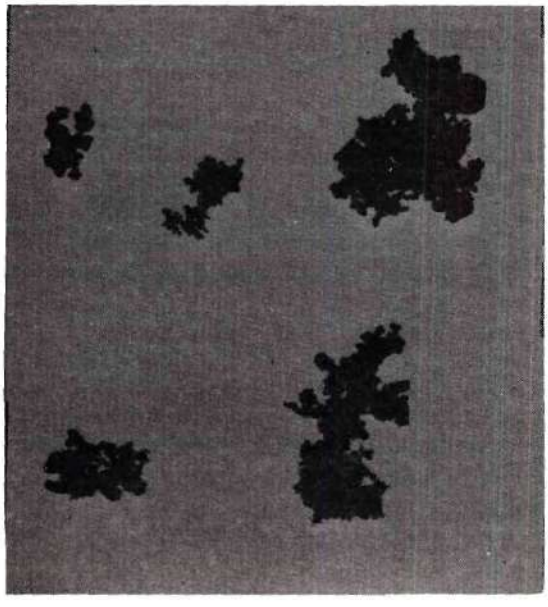

0.06 Micron.

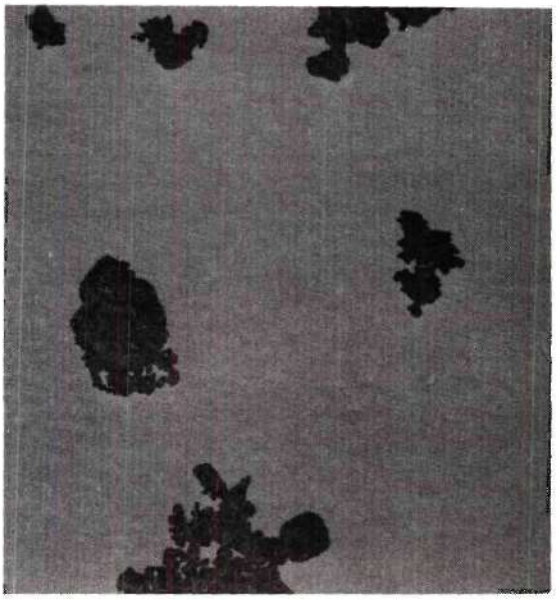

0.04 Micron.

1.0 Micron.

Figure 48. Electron Micrographs of Tungsten Particles of Different Average Sizes.

0.2 Micron.

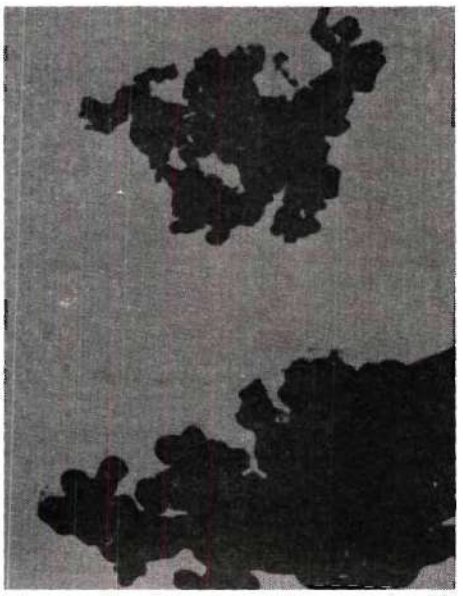

0.1 Micron.

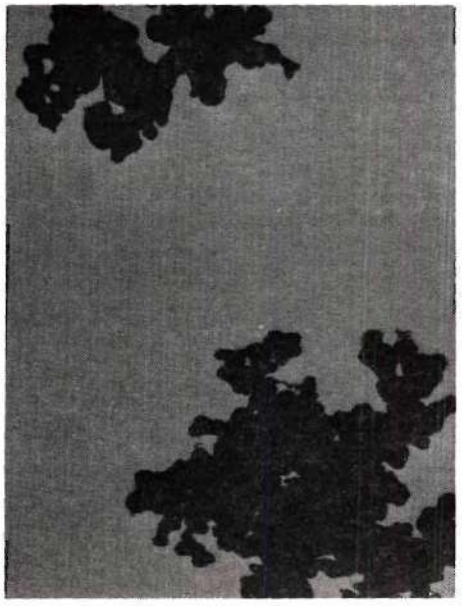

0.06 Micron.

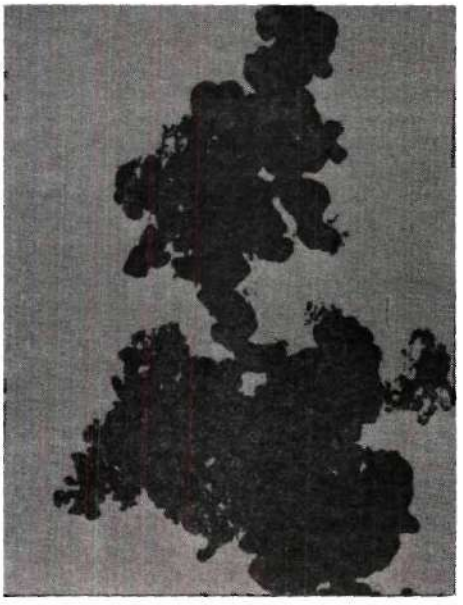

0.04 Micron.

0.1 Micron.

Figure 49. Electron Micrographs of Tungsten Particles of Different Average Sizes

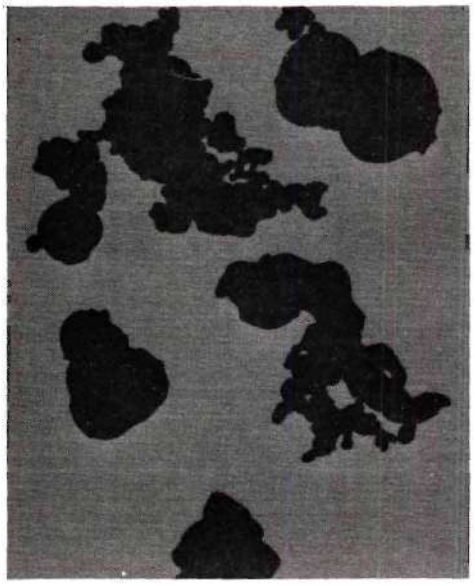

Tungsten

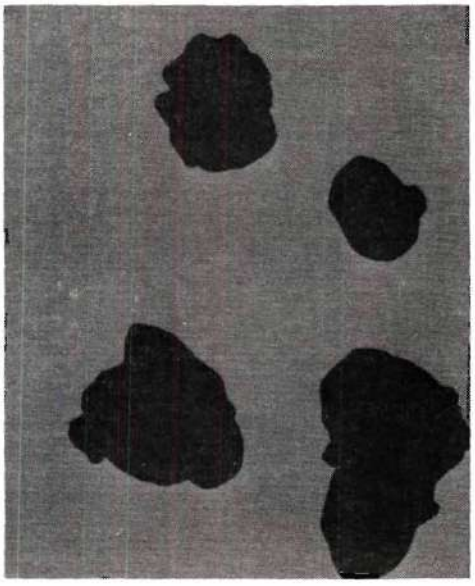

Tungsten Carbide

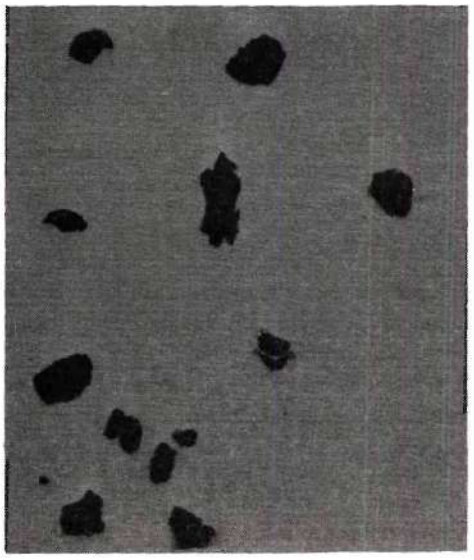

Silicon

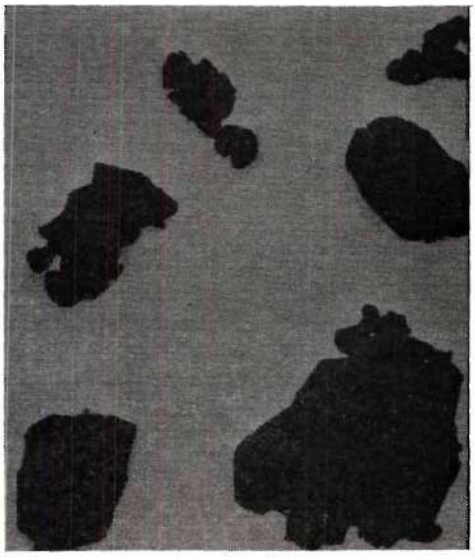

Silicon Carbide

1.0 Micron.

Figure 50. Electron Micrographs of Various Seed Material

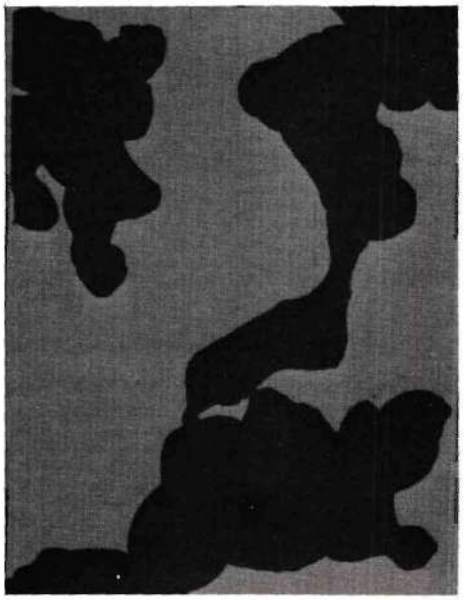

Tungsten

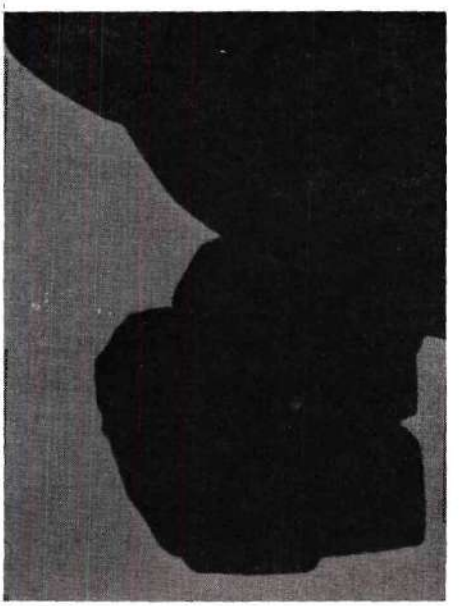

Tungsten Carbide

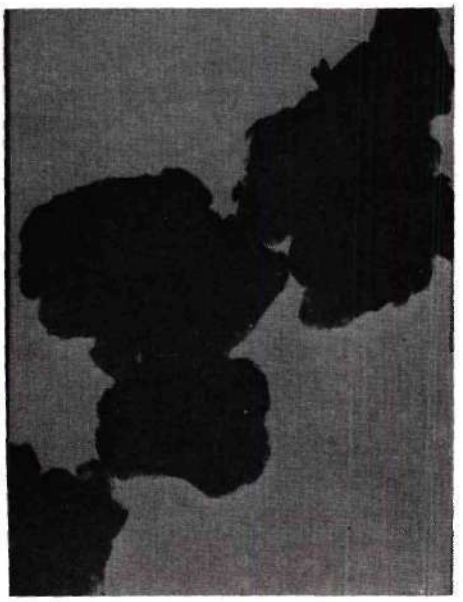

Silicon

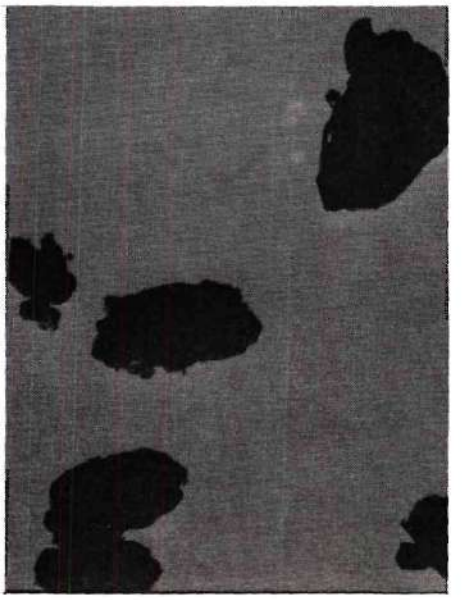

Silicon Carbide

0.1 Micron.

Figure 51. Electron Micrographs of Various Seed Material

of the same materials at a higher magnification. In the cases where the aerosol is deagglomerated by a nozzle, it is produced using the aerosol generator.

APPENDIX E

COMPUTED RESULTS

The data listed in Tables 2 through 17 are the mass attenuation coefficients of carbon, tungsten, and silicon of different sizes taken at various temperatures for radiation wavelengths from 1200 Å to 6000 Å. Each of the tables contains the results calculated using the computer program given in Appendix B. The results give, for each wavelength, the linear attenuation coefficient, the aerosol density, and the mass attenuation coefficient. The results also give the error associated with each of the mass attenuation coefficient values and give the percentage error.

Table 2. Attenuation Coefficient of Carbon at 80°F

SEED MATERIAL:CARBON SPHERON 6 PARTICLE SIZE:.025 MICRON .

TEMPERATURE = 80. F.

RESULTS

WAVELENGTH ANGSTROMS	K CM-1	RHO GMS/CC	K MASS CM2/GM	DEL K CM2/GM	PCT ERROR
1200	.5671	.0000101	55882.	6380.	11.42
1600	.4690	.0000101	46211.	5396.	11.68
2350	.4539	.0000067	67950.	8387.	12.34
2400	.3845	.0000065	59137.	7521.	12.72
2800	.5094	.0000080	63634.	7537.	11.84
3050	.6829	.0000097	70450.	7953.	11.29
3200	.5271	.0000090	58334.	6786.	11.63
3350	.4946	.0000093	53461.	6251.	11.69
3600	.5027	.0000093	54341.	6341.	11.67
3650	.4832	.0000088	54759.	6453.	11.78
3900	.3836	.0000069	55902.	7051.	12.61
4000	.4578	.0000074	61680.	7480.	12.13
4400	.4046	.0000080	50538.	6183.	12.23
4800	.4429	.0000097	45690.	5401.	11.82
5200	.3991	.0000070	56635.	7066.	12.48
5600	.4029	.0000080	50321.	6161.	12.24
6000	.5051	.0000101	49770.	5756.	11.56
6400	.4316	.0000088	48916.	5858.	11.97
6800	.2284	.0000058	39347.	5841.	14.85

Table 3. Attenuation Coefficient of Carbon at 1130°F

SEED MATERIAL:CARBON SPHERON 6 PARTICLE SIZE:.025 MICRON .

TEMPERATURE = 1130. F.

RESULTS

WAVELENGTH ANGSTROMS	K CM-1	RHO GMS/CC	K MASS CM2/GM	DEL K CM2/GM	PCT ERROR
1900	.1464	.0000036	40706.	14115.	34.68
2200	.1634	.0000036	45453.	15507.	34.12
2300	.1556	.0000043	36291.	11345.	31.26
3000	.1519	.0000033	46686.	17085.	36.60
3300	.1491	.0000036	41458.	14334.	34.58
3500	.1447	.0000036	40249.	13983.	34.74
4000	.1618	.0000036	44999.	15373.	34.16
4400	.1618	.0000036	44999.	15373.	34.16
4861	.1672	.0000043	39007.	12049.	30.89
5200	.1273	.0000043	29686.	9676.	32.59
5800	.2112	.0000050	42315.	11760.	27.79
6200	.1860	.0000057	32573.	8716.	26.76
6563	.1400	.0000057	24523.	6971.	28.43

Table 4. Attenuation Coefficient of Carbon at 1480°F

SEED MATERIAL:CARBON SPHERON 6 PARTICLE SIZE:.025 MICRON .

TEMPERATURE = 1480. F.

RESULTS

WAVELENGTH ANGSTROMS	K CM-1	RHO GMS/CC	K MASS CM2/GM	DEL K CM2/GM	PCT ERROR
1260	.1941	.0000073	26462.	4043.	15.28
1600	.2010	.0000076	26449.	3967.	15.00
1750	.2687	.0000079	34150.	4563.	13.36
2250	.3122	.0000076	41095.	5271.	12.83
2400	.3110	.0000076	40931.	5256.	12.84
2800	.3590	.0000079	45631.	5648.	12.38
3000	.3379	.0000079	42949.	5387.	12.54
3540	.3582	.0000076	47145.	5855.	12.42
3600	.3485	.0000079	44299.	5518.	12.46
4400	.3249	.0000066	49371.	7638.	15.47
4920	.2996	.0000066	45529.	7039.	15.46

Table 5. Attenuation Coefficient of Carbon at 1560°F

SEED MATERIAL:CARBON SPHERON 6 PARTICLE SIZE:.025 MICRON .

TEMPERATURE = 1560. F.

RESULTS

WAVELENGTH ANGSTROMS	K CM-1	RHO GMS/CC	K MASS CM2/GM	DEL K CM2/GM	PCT ERROR
1600	.0982	.0000031	31698.	12681.	40.01
2000	.1180	.0000031	38121.	14602.	38.30
2400	.1519	.0000028	54771.	21425.	39.12
2800	.1264	.0000028	45568.	18287.	40.13
2850	.1210	.0000031	39072.	14892.	38.11
3300	.1224	.0000025	49853.	21634.	43.39
3550	.1243	.0000025	50646.	21927.	43.29
4400	.1026	.0000025	41781.	18690.	44.73
4861	.1125	.0000025	45824.	20189.	44.06
5800	.1497	.0000025	60993.	28330.	46.45
6563	.1168	.0000025	47588.	20858.	43.83

Table 6. Attenuation Coefficient of Carbon at 2560°F

SEED MATERIAL:CARBON CARBOLAC 2 PARTICLE SIZE:.012 MICRON .

TEMPERATURE = 2560. F.

RESULTS

WAVELENGTH ANGSTROMS	K CM-1	RHO GMS/CC	K MASS CM2/GM	DEL K CM2/GM	PCT ERROR
1500	.8217	.0000130	63243.	7664.	12.12
1800	.3410	.0000067	51031.	7709.	15.11
2300	.2922	.0000075	38884.	5852.	15.05
2600	.3917	.0000067	58607.	8684.	14.82
3000	.4104	.0000071	57842.	8366.	14.46
3300	.2793	.0000051	54712.	9413.	17.20
3600	.2243	.0000059	38140.	6559.	17.20
4000	.3379	.0000055	61555.	9979.	16.21
4400	.2314	.0000067	34619.	5691.	16.44
4861	.2397	.0000040	60106.	11900.	19.80

Table 7. Attenuation Coefficient of Carbon at 2620°F

SEED MATERIAL:CARBON CARBOLAC 2 PARTICLE SIZE:.012 MICRON .

TEMPERATURE = 2620. F.

RESULTS

WAVELENGTH ANGSTROMS	K CM-1	RHO GMS/CC	K MASS CM2/GM	DEL K CM2/GM	PCT ERROR
1800	.6745	.0000113	59554.	6960.	11.69
3000	.6941	.0000092	75803.	9177.	12.11
3800	.7925	.0000125	63383.	7241.	11.42
4400	.2266	.0000030	76119.	16603.	21.81
4860	.5044	.0000087	57649.	7228.	12.54
6560	.0811	.0000022	36417.	12890.	35.39

Table 8. Attenuation Coefficient of Carbon at 3450°F

SEED MATERIAL:CARBON CARBOLAC 2 PARTICLE SIZE:.012 MICRON .

TEMPERATURE = 3450. F.

RESULTS

WAVELENGTH ANGSTROMS	K CM-1	RHO GMS/CC	K MASS CM2/GM	DEL K CM2/GM	PCT ERROR
1216	.0947	.0000011	85045.	34251.	40.27
1450	.0638	.0000009	69260.	35099.	50.68
1650	.0683	.0000010	67145.	31622.	47.10
2300	.0498	.0000011	44709.	23824.	53.29
2950	.0235	.0000005	43091.	45977.	106.70
4800	.0627	.0000009	68068.	34737.	51.03
5300	.0744	.0000011	66811.	30540.	45.71

Table 9. Attenuation Coefficient of 0.04 Micron Tungsten at 80°F

SEED MATERIAL:TUNGSTEN PARTICLE SIZE:.040 MICRON .

TEMPERATURE = 80. F.

RESULTS

WAVELENGTH ANGSTROMS	K CM-1	RHO GMS/CC	K MASS CM2/GM	DEL K CM2/GM	PCT ERROR
1216	.1336	.0000070	19147.	4324.	22.58
1350	.0886	.0000064	13837.	3982.	28.78
1600	.1390	.0000076	18375.	4008.	21.81
1750	.1519	.0000070	21772.	4654.	21.38
2000	.1176	.0000076	15537.	3682.	23.70
2300	.1707	.0000082	20896.	4128.	19.75
2800	.1761	.0000082	21560.	4211.	19.53
3000	.1322	.0000076	17467.	3901.	22.33
3350	.1860	.0000082	22768.	4366.	19.17
3550	.1536	.0000070	22008.	4685.	21.29
3600	.1510	.0000070	21644.	4638.	21.43
4000	.1011	.0000070	14492.	3790.	26.15
4400	.1519	.0000076	20079.	4215.	20.99
4861	.1730	.0000076	22867.	4570.	19.99
5200	.1008	.0000064	15745.	4187.	26.59
5600	.1165	.0000070	16690.	4032.	24.16
6000	.1096	.0000061	17925.	4591.	25.61
6400	.0982	.0000064	15333.	4141.	27.01

Table 10. Attenuation Coefficient of 0.04 Micron Tungsten at 700°F

SEED MATERIAL:TUNGSTEN PARTICLE SIZE:.040 MICRON .

TEMPERATURE = 700. F.

RESULTS

WAVELENGTH ANGSTROMS	K CM-1	RHO GMS/CC	K MASS CM2/GM	DEL K CM2/GM	PCT ERROR
1800	.0347	.0000025	13682.	16307.	119.19
3000	.0463	.0000025	18245.	20555.	112.66
3350	.0667	.0000025	26280.	28409.	108.10
3450	.0436	.0000043	10215.	9316.	91.20
4000	.0865	.0000025	34079.	36237.	106.33
4400	.0591	.0000025	23295.	25456.	109.28
4861	.1242	.0000043	29072.	23255.	79.99
5600	.0758	.0000043	17746.	14691.	82.79
6000	.1043	.0000043	24415.	19701.	80.69

Table 11. Attenuation Coefficient of 0.04 Micron Tungsten at 1220°F

SEED MATERIAL:TUNGSTEN PARTICLE SIZE:.040 MICRON .

TEMPERATURE = 1220. F.

RESULTS

WAVELENGTH ANGSTROMS	K CM-1	RHO GMS/CC	K MASS CM2/GM	DEL K CM2/GM	PCT ERROR
2300	.0836	.0000031	27271.	16071.	58.93
2900	.0982	.0000052	18875.	7941.	42.07
3100	.0933	.0000052	17936.	7645.	42.63
3300	.0982	.0000031	32010.	18414.	57.53
3600	.0487	.0000031	15897.	10817.	68.04
3700	.0740	.0000041	17944.	9120.	50.82
4000	.0738	.0000031	24066.	14524.	60.35
4400	.0641	.0000052	12333.	5980.	48.49
4861	.0944	.0000052	18162.	7717.	42.49
5600	.0646	.0000041	15673.	8322.	53.10
6200	.0613	.0000031	20005.	12627.	63.12

Table 12. Attenuation Coefficient of 0.04 Micron Tungsten at 1540°F

SEED MATERIAL:TUNGSTEN PARTICLE SIZE:.040 MICRON .

TEMPERATURE = 1540. F.

RESULTS

WAVELENGTH ANGSTROMS	K CM-1	RHO GMS/CC	K MASS CM2/GM	DEL K CM2/GM	PCT ERROR
1400	.0298	.0000018	16118.	15752.	97.73
1800	.0346	.0000018	18761.	17112.	91.21
2300	.0425	.0000012	34838.	34497.	99.02
3300	.0285	.0000012	23373.	26260.	112.35
3600	.0200	.0000012	16361.	21924.	134.00
3800	.0418	.0000012	34283.	34077.	99.40
4000	.0312	.0000012	25538.	27731.	108.59
4200	.0299	.0000012	24544.	27049.	110.21
4861	.0516	.0000012	42265.	40242.	95.21
5800	.0498	.0000018	26948.	21777.	80.81

Table 13. Attenuation Coefficient of 0.04 Micron Tungsten at 3000°F

SEED MATERIAL:TUNGSTEN PARTICLE SIZE:.040 MICRON .

TEMPERATURE = 3000. F.

RESULTS

WAVELENGTH ANGSTROMS	K CM-1	RHO GMS/CC	K MASS CM2/GM	DEL K CM2/GM	PCT ERROR
1800	.0693	.0000027	25542.	15906.	62.27
2000	.1222	.0000041	29582.	14196.	47.99
2300	.0541	.0000033	16525.	10306.	62.36
2800	.0944	.0000027	34827.	20535.	58.96
3000	.0863	.0000027	31819.	19009.	59.74
3200	.0753	.0000027	27776.	16995.	61.19
3400	.0451	.0000027	16615.	11821.	71.15
3600	.0568	.0000013	42548.	41919.	98.52
4000	.0636	.0000027	23467.	15546.	66.25

Table 14. Attenuation Coefficient of 0.2 Micron Tungsten at 80°F

SEED MATERIAL:TUNGSTEN PARTICLE SIZE:.200 MICRON .

TEMPERATURE = 80. F.

RESULTS

WAVELENGTH ANGSTROMS	K CM-1	RHO GMS/CC	K MASS CM2/GM	DEL K CM2/GM	PCT ERROR
1200	.5776	.0000440	13120.	1577.	12.02
1600	.6941	.0000440	15765.	1869.	11.86
2000	.4982	.0000440	11316.	1380.	12.20
2250	.5422	.0000440	12314.	1489.	12.09
2625	.5159	.0000440	11717.	1424.	12.15
3200	.4701	.0000440	10677.	1311.	12.28
3600	.5389	.0000417	12914.	1574.	12.19
4000	.4728	.0000440	10739.	1318.	12.27
4400	.5776	.0000440	13120.	1577.	12.02
4800	.5824	.0000417	13958.	1690.	12.11
5200	.5033	.0000395	12745.	1579.	12.39
5600	.4645	.0000406	11440.	1424.	12.45
6000	.4782	.0000417	11460.	1415.	12.35
6400	.5776	.0000417	13843.	1677.	12.12
6563	.4720	.0000417	11312.	1399.	12.37
6800	.5776	.0000440	13120.	1577.	12.02

Table 15. Attenuation Coefficient of 0.2 Micron Tungsten at 450°F

SEED MATERIAL:TUNGSTEN PARTICLE SIZE:.200 MICRON .

TEMPERATURE = 450. F.

RESULTS

WAVELENGTH ANGSTROMS	K CM-1	RHO GMS/CC	K MASS CM2/GM	DEL K CM2/GM	PCT ERROR
1200	.2397	.0000185	12924.	2283.	17.66
1600	.2972	.0000161	18430.	3273.	17.76
2000	.4257	.0000200	21239.	3357.	15.80
2400	.3144	.0000161	19495.	3435.	17.62
2625	.2585	.0000161	16026.	2914.	18.18
2800	.1432	.0000138	10388.	2357.	22.69
3200	.2186	.0000138	15860.	3167.	19.97
3600	.2247	.0000138	16301.	3236.	19.85
4000	.2247	.0000138	16301.	3236.	19.85
4800	.1285	.0000115	11153.	2808.	25.17
5200	.1618	.0000133	12141.	2666.	21.96
5600	.1860	.0000138	13489.	2804.	20.79
6000	.1193	.0000115	10353.	2688.	25.97
6563	.1631	.0000138	11832.	2560.	21.64

Table 16. Attenuation Coefficient of 0.2 Micron Tungsten at 1250°F

SEED MATERIAL:TUNGSTEN PARTICLE SIZE:.200 MICRON .

TEMPERATURE = 1250. F.

RESULTS

WAVELENGTH ANGSTROMS	K CM-1	RHO GMS/CC	K MASS CM2/GM	DEL K CM2/GM	PCT ERROR
1600	.0575	.0000083	6909.	3444.	49.85
2250	.0538	.0000059	9166.	5366.	58.54
2400	.1043	.0000083	12534.	5025.	40.09
2625	.0794	.0000083	9544.	4143.	43.41
2800	.0427	.0000083	5136.	3042.	59.22
3200	.0618	.0000083	7421.	3572.	48.13
3600	.0492	.0000071	6949.	3948.	56.82
4000	.1034	.0000071	14588.	6358.	43.58
4400	.1326	.0000071	18705.	7818.	41.80
5200	.0476	.0000071	6722.	3889.	57.86
5600	.0327	.0000053	6209.	4911.	79.09
6400	.1043	.0000083	12534.	5025.	40.09

Table 17. Attenuation Coefficient of Silicon at 80°F

SEED MATERIAL:SILICON PARTICLE SIZE:.200 MICRON .

TEMPERATURE = 80. F.

RESULTS

WAVELENGTH ANGSTROMS	K CM-1	RHO GMS/CC	K MASS CM2/GM	DEL K CM2/GM	PCT ERROR
1600	.2293	.0000037	62262.	9842.	15.81
1800	.2595	.0000041	63023.	9387.	14.90
2300	.2949	.0000047	62888.	8856.	14.08
2800	.3551	.0000053	67109.	8916.	13.29
3000	.3690	.0000055	66596.	8729.	13.11
3200	.3271	.0000054	60407.	8132.	13.46
3400	.3719	.0000053	70290.	9260.	13.17
3700	.3172	.0000048	65986.	9102.	13.79
3800	.3172	.0000048	65986.	9102.	13.79
4000	.3104	.0000043	71483.	10084.	14.11
4200	.3796	.0000048	78968.	10528.	13.33
4400	.3463	.0000046	75732.	10351.	13.67
4861	.2832	.0000043	65217.	9399.	14.41
5200	.2370	.0000043	54571.	8275.	15.16
5600	.3379	.0000048	70297.	9570.	13.61
5800	.4046	.0000050	80179.	10498.	13.09
6100	.3489	.0000048	72594.	9822.	13.53
6568	.3217	.0000048	66931.	9204.	13.75

APPENDIX F

DETECTION OF METHANE

In order to confirm that chemical reactions between carbon and hydrogen have taken place in the carbon-hydrogen aerosol heated in the furnace, an effort was made to detect methane in the effluent. A sample of hydrogen heated with carbon was collected in a sampling tube as shown in Figure 52. A mixture of carbon and hydrogen was heated to about 2500°F and drawn through the sampling port. After the mixture was cooled, the carbon particles were separated both by an electrostatic precipitator and a fiber glass filter before the hydrogen was collected in the sampling tube. The sampling system was evacuated initially to remove traces of water and other gases.

The collected sample was analyzed with a mass spectrograph. Peaks were observed at various atomic numbers for the constituents present in the sample. In this particular experiment, a distinct peak was noted for methane CH_4.

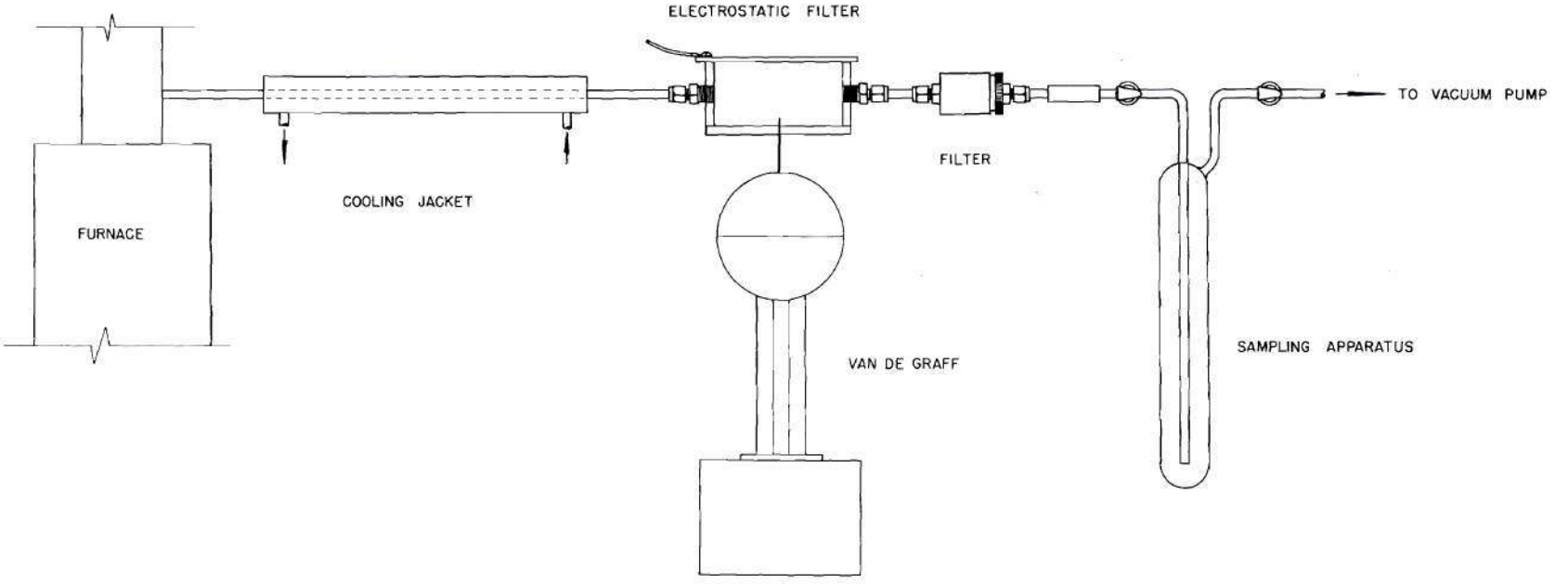

Figure 52. Furnace Exhaust Sampling Setup

APPENDIX G

EQUIPMENT PHOTOGRAPHS

Figure 53. Spectrometer Assembly - Furnace End

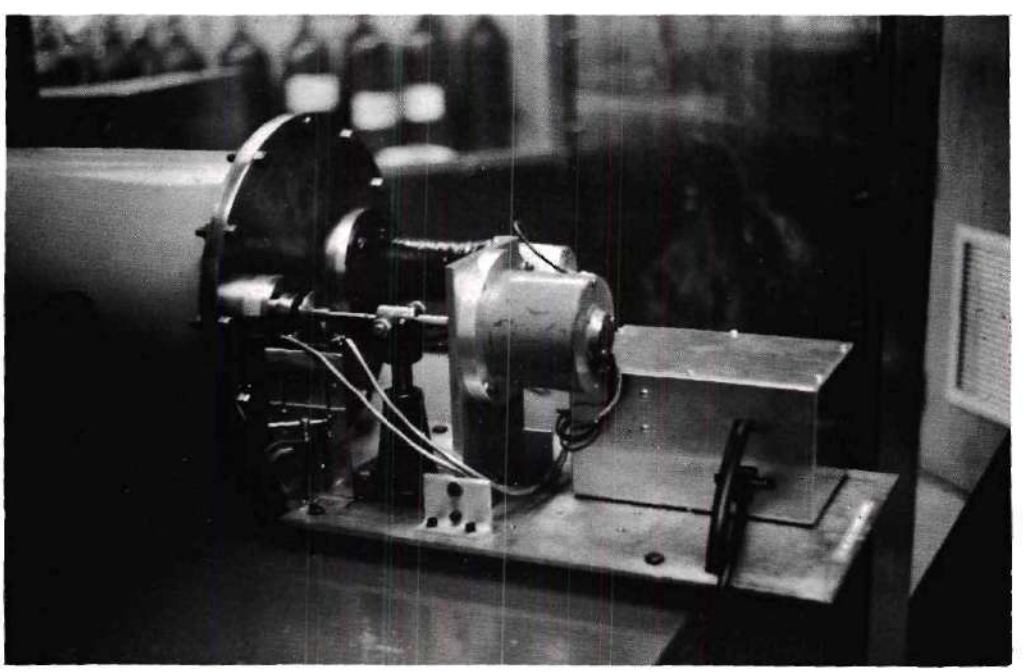

Figure 54. Spectrometer Assembly - Grating End

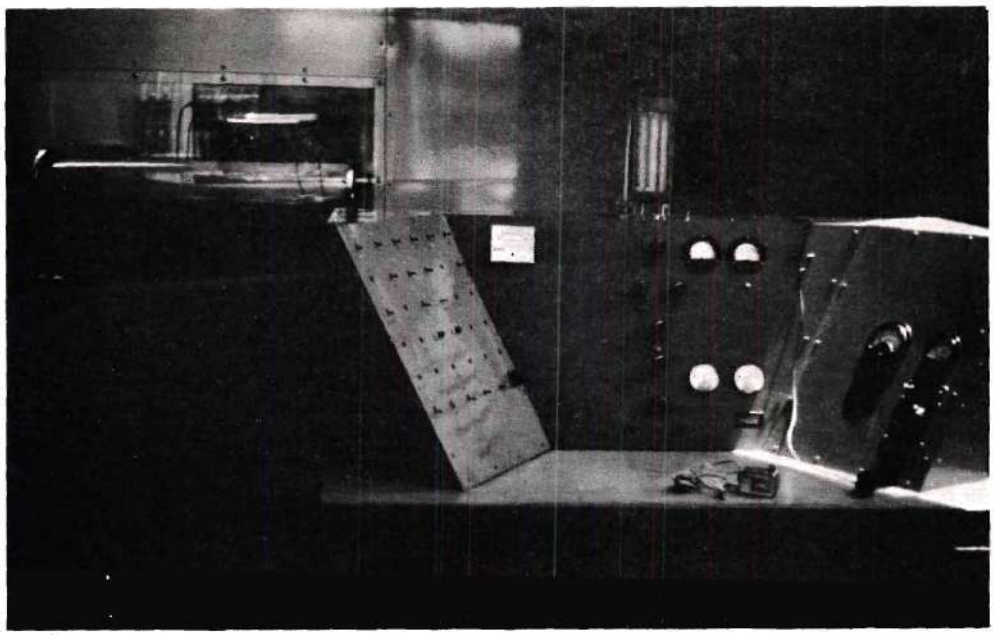

Figure 55. Control Console

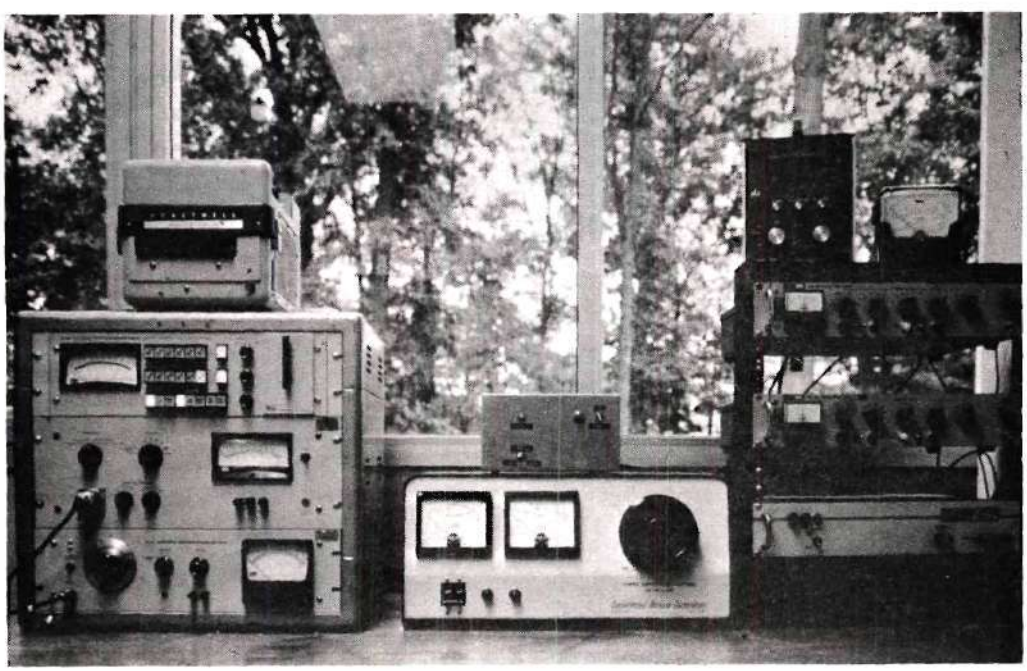

Figure 56. Instrumentation

BIBLIOGRAPHY

1. R. W. Bussard and R. D. DeLauer, Fundamentals of Nuclear Flight, McGraw-Hill Book Company, Inc., New York, 1965.

2. M. W. Hunter, Jr., "Single Stage Spaceships Should Be Our Goal," Nucleonics Handbook of Nuclear Research and Technology, McGraw-Hill Book Company, Inc., New York, 1966.

3. H. B. Finger, "The Case for Nuclear Energy," Nucleonics 19, No. 4, 64 (1961).

4. R. V. Meghreblian, "Gaseous Fission Reactors for Booster Propulsion," American Rocket Society Journal 32, 13 (1962).

5. R. V. Meghreblian, "Gaseous Fission Reactors for Spacecraft Propulsion," Jet Propulsion Laboratory, Technical Report, July 1960, pp. 32-42.

6. L. P. Hatch, W. H. Regan, and J. R. Powell, "Fluidized Solids as a Nuclear Fuel for Rocket Propulsion," American Rocket Society Journal 31, 547 (1961).

7. R. G. Ragsdale, A. F. Kascak, and L. F. Donovon, "Performance Potential of a Radiant Heat Transfer Liquid-Core Nuclear Rocket Engine," NASA TN-D 4127 (1967).

8. E. E. Duke and W. J. Houghton, "Gas-Core Nuclear Rocket Engine," Journal of Spacecraft 4, No. 12 (December, 1967).

9. F. E. Rom, "Coaxial Flow Gaseous Nuclear Reactor Concept," Proceedings of an Advanced Nuclear Propulsion Symposium, Los Alamos Scientific Laboratory Report, LA-3229, January, 1965, pp. 177-179.

10. G. H. McLafferty, "Work on the Nuclear Light Bulb at UAC Research Laboratories," Proceedings of an Advanced Nuclear Propulsion Symposium, Los Alamos Scientific Laboratory Report, LA-3229, January, 1965, pp. 137-147.

11. H. J. Stumpf, "Gas Core Reactors," Proceedings of an Advanced Nuclear Propulsion Symposium, Los Alamos Scientific Laboratory Report, LA-3229, January, 1965, pp. 293-339.

12. R. G. Ragsdale, "Coaxial Flow Research Studies," Proc. Adv. Nucl. Propulsion Symp., Los Alamos Scientific Laboratory Report, LA-3229, January, 1965, pp. 180-207.

BIBLIOGRAPHY (Continued)

13. R. G. Ragsdale and F. E. Rom, "Gas-Core Reactor Work at NASA/Lewis," AIAA 3rd Propulsion Joint Specialist Conference, Washington, D. C., Paper No. 67-499.

14. G. H. McLafferty and H. E. Bauer, "Studies of Specific Nuclear Light Bulb and Vortex-Stabilized Gaseous Nuclear Rocket Engines," United Aircraft Corporation Research Laboratories Report No. F-910093-37 (September 1967).

15. G. H. McLafferty and G. F. Hausmann, "Investigations of a Unique Gaseous-Core Nuclear Rocket Concept," United Aircraft Corporation Research Laboratories Report No. R-2494-4 (November 1961).

16. N. L. Krascell, "Tables of the Composition, Opacity and Thermodynamic Properties of Hydrogen at High Temperatures," United Aircraft Corporation Research Laboratories Report No. B-910168-1 (September 1963).

17. E. G. Schneider, Physical Review 49, 341 (1936).

18. Peter Debye, Annalen der Physik 30, 57 (1909).

19. G. Mie, Ann. d. Physik 25, 377 (1908).

20. N. L. Krascella, "Theoretical Investigation of the Absorption and Scattering Characteristics of Small Particles," UAC Research Laboratories Report C-910092-1 (September 1964).

21. J. Svatos, "Light Scattering by Flattened Ellipsoids," Astronomical Institute of Czechoslavakia Bulletin 18, No. 2, 114-119 (1967).

22. C. D. Lanzo and R. G. Ragsdale, NASA TND-1405 (September 1962).

23. C. D. Lanzo and R. G. Ragsdale, Proceedings of the 1964 Heat Transfer and Fluid Mechanics Institute, Standard University Press (1964).

24. J. A. McAlister, David Kocsis, and Clyde Orr, Jr., Heat Transfer to a Gas Containing a Cloud of Particles, Semi-annual Status Report No. 8, Project A-635-002, Georgia Institute of Technology, Engineering Experiment Station, Atlanta, Georgia, June, 1966.

25. Edward Keng and Clyde Orr, Jr., "Investigation of Radiant Heat Transfer to Particle-seeded Gases for Application to Nuclear Rocket Engine Design," NASA CR-953 (November 1967).

26. P. J. Marteney, "Experimental Investigation of the Opacity of Small Particles," UAC Research Laboratories Report C-910092-2 (September 1964).

BIBLIOGRAPHY (Concluded)

27. Valerie C. Burkig, "Theoretical Absorption in Seeded Gases," Douglas Report DAC-59985, Nasw-1310 (January, 1967).

28. J. A. Jenkins and H. E. White, Fundamentals of Optics, McGraw-Hill Book Company, Inc., New York, 1957, p. 424.

29. J. R. Williams, "Radiative Heat Transfer in the Gaseous Core Nuclear Rocket," Ph.D. Dissertation, Georgia Institute of Technology, Atlanta, Georgia, May, 1967.

30. T. J. Love and J. F. Beattie, "Experimental Determination of Thermal Radiation Scattering by Small Particles," Aerospace Research Laboratories Report ARL 65-110 (June 1965).

31. C. C. Masser, "Radiant Heating of a Seeded Gas in a Coaxial-Flow Gaseous Reactor," NASA TN-D-3197 (January 1966).

32. C. A. Fritsch, R. J. Grosh, and M. W. Wildin, "Radiative Heat Transfer Through an Absorbing Boundary Layer," Journal of Heat Transfer (ASME) 88, 296-304 (August 1966).

33. J. R. Howell and H. E. Renkel, "Analysis of the Effects of a Seeded Propellant Layer on Thermal Radiation in the Nozzle of a Gaseous Core Nuclear Propulsion System," NASA TN-D-3119 (1962).

34. Y. Tanaka, R. E. Huffman, and J. C. Larrabee, "Recent Improvements in Rare Gas Continua in the Vacuum Ultraviolet Region," Journal of Quantum Spectrosc Radiant Transfer 2, 451-464 (1963).

35. J. A. Stratton, Electromagnetic Theory, McGraw-Hill Book Company, Inc., New York, 1941.

36. H. C. Van de Hulst, Light Scattering by Small Particles, John Wiley and Sons, New York, 1957.

37. Max Born and Emil Wolf, Principles of Optics, 2nd Edition, Macmillan Company, New York, 1964.

38. A. L. Aden, "Electromagnetic Scattering from Spheres with Sizes Comparable to the Wavelength," Journal of Applied Physics 22, No. 5, 601-605 (1951).

39. S. Roberts, "Optical Properties of Nickel and Tungsten and Their Interpretation According to Drudis Formula," Phys. Rev. 114, No. 1 104-115 (1959).

40. V. R. Stull and G. N. Plass, "Emissivity of Dispersed Carbon Particles," Journal of Optical Society of America 50, No. 2 (1960).

VITA

Arkal Subraya Shenoy was born in Mangalore, Mysore State, India, on November 12, 1941. He lived with his uncle, Mr. M. Gopal Bhat, in Mangalore and attended St. Aloysius' College High School from which he was graduated in 1958. He attended the College of Engineering, Davangere, Mysore State and received the degree of Bachelor of Mechanical Engineering "With University Rank" in January 1964. He entered the Indian Institute of Science in August, 1964 and obtained the degree of Master of Engineering in Heat Power Engineering "With Distinction" in June, 1966.

In September 1966, Mr. Shenoy came to the United States to continue his education in nuclear engineering. He completed requirements for a Master of Science in Nuclear Engineering in 1967, at which time he began work toward the Doctor of Philosophy in the School of Nuclear Engineering.

Mr. Shenoy is a member of the American Nuclear Society, American Society of Mechanical Engineers, American Institute of Aeronautics and Astronautics, and the honor Society of Sigma Xi. He is co-author of several papers, including "Radiant Propellant Heating in the Gaseous Core Nuclear Rocket" and "Measurement of Heat Transfer Parameters for the Gaseous Core Nuclear Rocket."

Mr. Shenoy has been active in a number of campus organizations and is an Executive Committee member of the International Student Organization of Georgia Tech. He is a member of the India Association of Atlanta and the Indo-American Cultural Society, both social organizations.